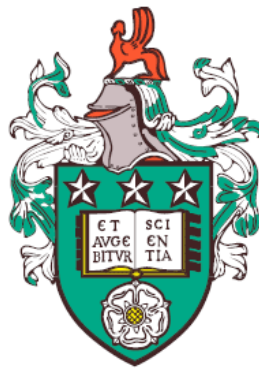


---

# Computer simulations of dynamics, structure and rheology of packed soft colloids



Tom Ridley

Faculty of Engineering and Physical Sciences

University of Leeds

Submitted in accordance with the requirements for the degree of

*Doctor of Philosophy*

October 12, 2020

---

## Statement of authorship

I, Tom Ridley confirm that the work submitted is my own and that appropriate credit has been given where reference has been made to the work of others.

Leeds, October 12, 2020

.....

This copy has been supplied on the understanding that it is copyright material and that no quotation from the thesis may be published without proper acknowledgement.

The right of Tom Ridley to be identified as Author of this work has been asserted by Tom Ridley in accordance with the Copyright, Designs and Patents Act 1988.

## Acknowledgements

I'd like to start by thanking my friends. Trying to complete a thesis in the middle of a global pandemic is an absurd, impossible task, and without their support, this would never have been submitted. I thank especially James Edward George Dickinson, Caseley, Ruthy, Sandy, Timms, Payling, Rashmi, Orla, Ben, Matt and Ethan. I also really appreciate the support from my siblings, Ben and Emma.

I also definitely need to thank Robert Welch, Ben Hanson and Albert Solernou for the bulk of the work on FFEA during my PhD, that I've modified to do my own dark tasks. Standing on the shoulders of giants, and all that.

I also thank my supervisory team, Oliver Harlen, Daniel Read, and Johan Mattsson, as well as Sarah Harris, for sharing their knowledge and enthusiasm for soft matter and FFEA with me. Additionally I would like to thank Michel Cloitre and ESPCI Paris for hosting me and allowing me, a theoretician and simulator, to get my grubby mitts dirty doing some experimental rheology on an unusual and tricky system, and being patient with my cluelessness. Thanks also to Mike Evans who, after a discussion at my transfer viva, turned round and gave me a random sphere placement code that was exactly what we needed.

Finally I'd like to thank SOFI CDT for the training and support for this PhD and EPSRC for funding this research. The simulations included in this work were undertaken on ARC3 and ARC4, part of the High Performance Computing facilities at the University of Leeds, UK.

## Abstract

‘Soft’ colloids are typically micron or sub-micron scale structured objects such as polymer microgels, which consist of chemically cross-linked polymer networks that are compressible and deformable. Experiments suggest that at packing ratios where the structural dynamics of hard colloids are arrested, a soft colloid system may still be able to flow as a consequence of cage-breaking due to particle deformation. However, the link between the detailed elastic properties of soft colloids and the resulting dynamics are presently not well understood. Soft packed colloids show rich and complex rheological and flow behaviour and it is important to derive the links between the single particle elastic properties and the resulting suspension’s behaviour.

The simulations described in this thesis utilise a recently developed computational algorithm, Fluctuating Finite Element Analysis, for simulating viscoelastic objects undergoing thermal excitation. This approach captures the detailed shape deformations of the colloidal particles allowing the structure of the objects as well as the effect of anisotropic deformation to be considered.

I apply Fluctuating Finite Element Analysis to soft colloidal systems, investigating the effects of varying effective volume fraction and material parameters on the dynamics, structure and rheology of both

thermally diffusing and linearly sheared soft colloidal systems. Additionally, I present results of an experimental rheology investigation of ultrasoft polymer microgels, and compare to sheared simulation results.

I find evidence of a diffusive regime between cages in all quiescent simulations, and frustration of long range ordering. I find the structural modulus of systems depends on the volume fraction, while mean squared displacement does not. Applying shear, I find a relationship between the diffusion timescale of the system and the timescale at which the system yields and layers. I find that shear response is similar to less expensive simulation techniques, and does not reproduce ultrasoft behaviour.

## Abbreviations

FFEA	Fluctuating Finite Element Analysis
PBC	Periodic Boundary Condition
LEBC	Lees-Edwards Boundary Condition
VdW	Van Der Waals
CoM	Centre of Mass
HPC	High Performance Computing
MPI	Message Passing Interface
LHS	Left Hand Side
RHS	Right Hand Side
MD	Molecular Dynamics
pNIPAM	Poly(N-isopropylacrylamide)
ESPCI Paris	École supérieure de physique et de chimie industrielles de la Ville de Paris
MMC	(Soft Matter and Chemistry) Matière Molle et Chimie
EA	Ethyl-Acrylate
MAA	Methacrylic Acid
TMPTA	Trimethylpropane Triacrylate
RPM	Revolutions Per Minute
CR	Count Rate
SAOS	Small Amplitude Oscillatory Shear
LAOS	Large Amplitude Oscillatory Shear
MSD	Mean-Square Displacement
RMSD	Root Mean-Square Displacement
PDF	Probability Distribution Function

# Contents

<b>1</b>	<b>Introduction</b>	<b>1</b>
1.1	What is a colloid? . . . . .	1
1.2	Diffusion . . . . .	2
1.3	Hard and soft colloids . . . . .	5
1.3.1	Polymer microgels . . . . .	8
1.4	Experimental characterisation . . . . .	9
1.5	Simulation techniques for colloidal systems . . . . .	16
1.6	Key research questions . . . . .	23
1.7	Thesis outline . . . . .	24
<b>2</b>	<b>Fluctuating Finite Element Analysis (FFEA)</b>	<b>27</b>
2.1	Mathematical model of FFEA . . . . .	29
2.2	Colloid interactions . . . . .	36
2.3	Summary . . . . .	38
<b>3</b>	<b>Simulations of Soft Colloids using FFEA</b>	<b>41</b>
3.1	Building a soft colloidal simulation . . . . .	43
3.1.1	Construction of a single colloidal particle . . . . .	43

## CONTENTS

---

3.1.2	Periodic Boundary Conditions . . . . .	46
3.1.3	Lees-Edwards Boundary Conditions and external forcing due to shear . . . . .	50
3.2	Initialisation of a simulation . . . . .	53
3.3	Stress calculation . . . . .	55
3.4	Multi- $\tau$ correlator . . . . .	56
3.4.1	General background . . . . .	56
3.4.2	Theory and implementation . . . . .	57
3.4.3	Stress autocorrelation . . . . .	62
3.4.4	Mean-Square Displacement . . . . .	62
3.5	Practical considerations . . . . .	65
3.5.1	Parallelisation . . . . .	65
3.5.2	Bottlenecks . . . . .	68
3.5.3	General limitations and further work . . . . .	68
3.6	Summary . . . . .	71
<b>4</b>	<b>Quiescent Simulations</b>	<b>73</b>
4.1	Parameter space . . . . .	75
4.2	Repeated simulations and consistency . . . . .	76
4.2.1	Overlapping simulations . . . . .	77
4.2.2	Finite size effects and Convergence . . . . .	78
4.3	Observed volume fraction . . . . .	82
4.4	Structure . . . . .	84
4.5	Mean-Squared Displacement . . . . .	91
4.5.1	Expected behaviour . . . . .	91

4.5.2	Results and discussion . . . . .	92
4.6	Visualisation of trajectories of colloids . . . . .	99
4.7	Peak in non-Gaussian behaviour . . . . .	104
4.8	Correlation between particle deformation and motion . . . . .	111
4.9	Stress correlator . . . . .	114
4.10	Conclusion . . . . .	124
<b>5</b>	<b>Experimental Rheology</b>	<b>127</b>
5.1	Microgels . . . . .	131
5.1.1	Material . . . . .	131
5.1.2	Sample preparation . . . . .	133
5.2	Free chains . . . . .	134
5.2.1	Sample preparation . . . . .	134
5.2.2	Static Light Scattering . . . . .	135
5.2.3	Thermogravimetry . . . . .	136
5.2.4	Centrifugation . . . . .	136
5.3	Rheological experiments . . . . .	137
5.3.1	Experimental setup . . . . .	137
5.3.2	Steady shear . . . . .	139
5.3.3	Oscillatory rheology . . . . .	140
5.4	Results and discussion . . . . .	142
5.4.1	Batches . . . . .	142
5.4.2	Aging and history dependence . . . . .	149
5.4.3	Master flowcurve . . . . .	152
5.5	Conclusion . . . . .	157

## CONTENTS

---

<b>6 Sheared Simulation Results</b>	<b>159</b>
6.1 Shear . . . . .	160
6.2 Parameter space and number of simulations . . . . .	161
6.3 Results . . . . .	162
6.3.1 Observed volume fraction . . . . .	162
6.3.2 Mean-Squared Displacement . . . . .	164
6.4 Flowcurve . . . . .	168
6.4.1 Normal stress differences . . . . .	171
6.4.2 Scattering . . . . .	173
6.5 Comparison to experiments and other simulation techniques . . . . .	178
6.6 Conclusion . . . . .	180
<b>7 Conclusion</b>	<b>183</b>
7.1 Progress overview . . . . .	183
7.2 Future applications and development . . . . .	185
<b>References</b>	<b>203</b>

# List of Figures

1.1	Schematic representation of cage-breaking or rearrangement through collective motion of hard particles. Note that the cage must break entirely and particles experience significant change in their centroid position. . . . .	3
1.2	Schematic representation of cage-breaking or rearrangement through collective motion of soft particles. Note that few of the caging particles experience significant change in their centroid positions. . .	4
1.3	Phase diagram of monodisperse hard spheres as a function of volume fraction $\phi$ . Equilibrium states are indicated by solid arrows while dashed arrows are non-equilibrium states. Glassy states require at least 8% polydispersity. Image reproduced from <a href="#">Hunter &amp; Weeks (2012)</a> . . . . .	6
1.4	Schematic of simple rotational rheometer with cone-plate geometry viewed from the side, describing the edge of the plate, with idealised solid-like behaviour on the left and idealised liquid like behaviour on the right. . . . .	14

## LIST OF FIGURES

---

2.1	2D illustration of FFEA steric repulsion with 3D tetrahedra reduced to triangles $a$ and $b$ . $V$ is the volume overlap and $F_{ba}$ is the force applied on tetrahedron $a$ by the overlap with tetrahedron $b$ . $F_{ab} = -F_{ba}$ is the Force applied to tetrahedron $b$ . This force is linearly interpolated over all nodes of the tetrahedron(Solernou <i>et al.</i> , 2018). . . . .	37
3.1	(a) 2-dimensional cartoon of PBCs. Straight dotted lines denote voxels while straight solid lines denote simulation box boundaries. Solid particle lines denote position of particle in simulation. Dotted particle lines indicate projected image of particle through PBCs. The particle filled in solid black considers interactions with particles in surrounding voxels, finding particles to consider interactions in all voxels from the opposite edge. All projected images of particles from these voxels are checked for collision, and only the gray, hatched particle is found to overlap. The black particle and the hatched grey particle experience a corrective steric force due to this overlap. (b) Illustrative visualisation of identical collisions simulated in FFEA using corrected PBCs in the centre of the simulation box and at the edge. . . . .	49

## LIST OF FIGURES

---

3.2	Cartoon of LEBCs. Thick lines denote the boundary of the simulation box and thin lines denote the edge of voxels. The solid black particle on the edge of the box in the $x$ -direction interacts with the grey hatched particle as it would in standard PBCs. The black particle on the edge of the box in the $y$ -direction interacts with the image of the white hatched particle, with the image offset by $O_{box}$ in the $x$ -direction due to the implementation of LEBCs. . . . .	52
3.3	Identical collisions between two colloids in a shear gradient in the (a) middle and (b) edge of the simulation box, illustrating the offset due to LEBCs. . . . .	53
3.4	Schematic view of the data structure implemented in the multi- $\tau$ correlator. We represent each level of storage, with the arrow representing the averaging and transferring between different levels of the correlator. Schematic used from <a href="#">Ramírez <i>et al.</i> (2010)</a> . . . . .	59
3.5	Verification of the correlator for a particle diffusing in a potential well. Correlator output matches $e^{-t}$ until its value is low enough that noise begins to cause deviation from the analytic result. . . . .	61
3.6	(a)Speedup of simulation relative to single core performance of both ARC3 and ARC4. (b) Relative efficiency of each core compared to single core performance. . . . .	66
4.1	Space explored with quiescent simulations. . . . .	76
4.2	Quantitative difference between simulation instances with larger surface interaction cutoff (upper curves) and original interaction cutoff (lower curves) for 12kPa simulations with $\zeta_e = 0.6$ . . . . .	78

## LIST OF FIGURES

---

- 4.3 (a) Plot of MSD of 10 instances of 100-colloid systems at  $\zeta_e = 0.8$ , and a single instance of an 1000-colloid system at the same  $\zeta_e$ . The 100 colloid systems have significant variance in behaviour, and diverge significantly from the 1000-colloid results due to finite size effects. (b) Consistency in MSD of ten 1000 colloid simulations at  $\zeta_e = 0.8$ . . . . . 81
- 4.4 (a) Observed real volume fraction  $\phi$  versus  $\zeta_e$  for 12kPa and 2kPa series, dashed line indicates  $\phi = \zeta_e$ . (b)  $\phi$  versus bulk modulus  $K$ . 83
- 4.5 Representative sample of scattering amplitude averaged over  $x - y, y - z, x - z$  planes for all simulations and every 10<sup>th</sup> simulation checkpoint output at given parameter values. The solid line in radial profiles represent spherical average of the corresponding data, while the square markers represent Percus-Yevick behaviour (Percus & Yevick, 1958) for  $\phi = 0.55$  with an effective radius of the particles is 500nm, scaled to have a coincident first peak, y-intercept and high  $|q|$  value, as a representative example of amorphous hard-sphere behaviour. Results shown for (a)  $\zeta_e = 0.6, K = 2\text{kPa}, \phi = 0.525$ , (b) Radial profile of **a**, (c)  $\zeta_e = 0.8, K = 2\text{kPa}, \phi = 0.642$ , (d) Radial profile of **c**. . . . . 85

4.6 Representative sample of scattering amplitude averaged over  $x - y, y - z, x - z$  planes for all simulations and every 10<sup>th</sup> simulation checkpoint output at given parameter values. The solid line in radial profiles represent spherical average of the corresponding data, while the square markers represent Percus-Yevick behaviour (Percus & Yeivick, 1958) for  $\phi = 0.55$  with an effective radius of the particles is 500nm, scaled to have a coincident first peak, y-intercept and high  $|q|$  value, as a representative example of amorphous hard-sphere behaviour. Results shown for (a) $\zeta_e = 1.0, K = 2\text{kPa}, \phi = 0.720$ , (b) Radial profile of **a**. . . . . 86

4.7 Representative sample of scattering amplitude averaged over  $x - y, y - z, x - z$  planes for all simulations and every 10<sup>th</sup> simulation checkpoint output at given parameter values. The solid line in radial profiles represent spherical average of the corresponding data, while the square markers represent Percus-Yevick behaviour (Percus & Yeivick, 1958) for  $\phi = 0.55$  with an effective radius of the particles is 500nm, scaled to have a coincident first peak, y-intercept and high  $|q|$  value, as a representative example of amorphous hard-sphere behaviour. Results shown for (a) $\zeta_e = 0.6, K = 12\text{kPa}, \phi = 0.586$ , (b) Radial profile of **a**, (c) $\zeta_e = 0.8, K = 12\text{kPa}, \phi = 0.748$ , (d) Radial profile of **c**. . . . . 87

4.8 MSD of [2kPa varied  $\zeta_e$ ]: (a)Simple MSD, (b) MSD divided by  $\tau$ . 92

4.9 MSD of [ $\zeta_e = 0.7$ , Varied  $K$ ]: (a)Simple MSD, (b) MSD divided by  $\tau$ . . . . . 94

4.10 MSD of [12kPa varied  $\zeta_e$ ]: (a)Simple MSD, (b) MSD divided by  $\tau$ . 95

## LIST OF FIGURES

---

4.11	Comparisons of MSD for systems with similar $\phi$ : (a)Systems with $\phi \simeq 0.59$ , (b)Systems with $\phi \simeq 0.68$ , (c)Systems with $\phi \simeq 0.64$ . . .	96
4.12	Approximate diffusivities against $\phi$ for all simulations. . . . .	97
4.13	Representative sample of particle trajectories for 50 particles with highest displacement over course of simulation. Particle begins at yellow and transitions to red, with each section of the trajectory representing displacement over $10^{-4}$ s. Results shown for systems where $K = 2\text{kPa}$ : (a) $\zeta_e = 0.6$ , $\phi = 0.525$ , (b) $\zeta_e = 0.8$ , $\phi = 0.642$ , (c) $\zeta_e = 1.0$ , $\phi = 0.720$ . . . . .	100
4.14	Representative sample of particle trajectories for 50 particles with highest displacement over course of simulation. Particle begins at yellow and transitions to red, with each section of the trajectory representing displacement over $10^{-4}$ s. Results shown for systems where $K = 12\text{kPa}$ : (a) $\zeta_e = 0.6$ , $\phi = 0.586$ , (b) $\zeta_e = 0.8$ , $\phi = 0.748$ . . . . .	101
4.15	Single particle trajectories of particle with highest displacement over course of simulation. Particle begins at yellow and transitions to red, with each section of the trajectory representing displacement over $10^{-4}$ s. Results shown for softest, least packed system and most packed hard system: (a) $\zeta_e = 0.6$ , $K = 2\text{kPa}$ , $\phi = 0.525$ . (b) 50th highest displacement particle in simulation a, showing more intermittent cage breaking. (c) $\zeta_e = 0.8$ , $K = 12\text{kPa}$ , $\phi = 0.748$ . (d) 50th highest-displacement particle in simulation c, showing a greater degree of caging. . . . .	102
4.16	Non-gaussian parameter $\alpha_2(\tau)$ for each set of parameters for (a)2kPa varied $\zeta_e$ , (b)Varied moduli, $\zeta_e = 0.7$ . (c)12kPa varied $\zeta_e$ . . . . .	105

## LIST OF FIGURES

---

4.17 Comparisons of non-Gaussian parameter $\alpha_2$ for systems with similar $\phi$ : (a)Systems with $\phi \simeq 0.59$ , (b)Systems with $\phi \simeq 0.68$ , (c)Systems with $\phi \simeq 0.64$ . . . . .	108
4.18 Histogram of displacements in units of RMSD for $\zeta_e = 0.7, K = 4\text{kPa}$ simulations for various timelags as denoted in the plots. Red line represents the PDF for a gaussian system with the MSD of this system. . . . .	109
4.19 MSD divided by $\tau$ and $\alpha_2$ for $\zeta_e = 0.7, K = 4\text{kPa}$ simulations with timescales used for displacement histograms marked. . . . .	110
4.20 (a)Covariance of instantaneous velocity with ratio $\frac{\lambda_{max}}{\lambda_{min}}$ of the shape tensor of the particle for a representative sample of simulations. (b)Measure of correlation of eigenvector corresponding to $\lambda_{max}$ and instantaneous velocity. . . . .	111
4.21 Stress correlation function against time lag $\tau$ and i-Rheo (Tassieri <i>et al.</i> , 2018) converter embedded in RepTate (Boudara <i>et al.</i> , 2020) deconvolution of of $G', G''$ for (a)2kPa varied $\zeta_e$ , (b) $G', G''$ generated using data from <b>a</b> , (c)Varied moduli, $\zeta_e = 0.7$ , (d) $G', G''$ generated using data from <b>c</b> . . . . .	115
4.22 Stress correlation function against time lag $\tau$ and i-Rheo (Tassieri <i>et al.</i> , 2018) converter embedded in RepTate (Boudara <i>et al.</i> , 2020) deconvolution of of $G', G''$ for (a)12kPa varied $\zeta_e$ , (b) $G', G''$ generated using data from <b>a</b> . . . . .	116
4.23 Output of stress correlation function against time lag $\tau$ for all instances of simulation at $\zeta_e = 0.8, K = 12\text{kPa}$ . . . . .	118

## LIST OF FIGURES

---

4.24	Comparisons of deviatoric stress correlation functions for systems with similar $\phi$ . . . . .	119
4.25	Comparisons of deviatoric stress correlation functions at intermediate value of $10^{-4}$ s versus (a) volume fraction $\phi$ , linear scaled, (b) $\phi$ , log scaled in $G_{Elastic}$ , (c) effective volume fraction $\zeta_e$ , (d) $\zeta_e$ , with $G_{Elastic}$ scaled by $\frac{1}{G_{Particle}}$ , log scaled in $\frac{G_{Elastic}}{G_{Particle}}$ . . . . .	120
4.26	Comparisons of deviatoric stress correlation functions at short timescale of $10^{-7}$ s normalised by $\frac{1}{G_{Particle}}$ versus (a) volume fraction $\phi$ , (b) effective volume fraction $\zeta_e$ . . . . .	122
5.1	Variation of elastic modulus $G_0$ with concentration for lin-lin plots of (a) Standard soft colloid, (b) Ultrasoft colloid and the same data on log-lin plots for (c) and (d). Plots and data from <a href="#">Mattiello (2018)</a> . . . . .	129
5.2	Constituent monomers of the microgel polymer network. Above, the two monomers EA and MAA, and below the crosslinker TMPTA. Figure from <a href="#">Mattiello (2018)</a> . . . . .	132
5.3	Schematic of plate and cell geometries used for rheological measurements. . . . .	138
5.4	Log-log Flowcurves showing difference between previous measurements of Batch 1 by <a href="#">Mattiello (2018)</a> , new measurements of Batch 1 and measurements of Batch 2 at various wt% of microgel: (a)1.5wt%, (b) 2.5wt%, (c) 3wt%, (d) 4wt%, . . . . .	143
5.4	(e)5wt%. . . . .	144

5.5 Log-log Frequency sweeps showing difference between previous measurements of Batch 1 by [Mattiello \(2018\)](#), new measurements of Batch 1 and measurements of Batch 2 at various wt% of microgel: (a)1.5wt%, (b) 3wt%, (c) 5wt%. . . . . 146

5.6 Log-log amplitude Sweeps showing difference between measurements of Batch 1 and measurements of Batch 2 at 1.5 wt% of microgel at  $\omega =$  for (a)1  $\text{rads}^{-1}$ , (b) 10  $\text{rads}^{-1}$ . . . . . 147

5.7 Log-log Flowcurves showing difference between measurements fresh (1 day after sample preparation) and aged (1-2 weeks after sample preparation) for (a) 3wt%, Batch 1, (b) 3wt%, Batch 2, (c) 5wt% Batch 1, (d) 5wt% Batch 2. . . . . 150

5.8 Log-log frequency sweeps showing difference between measurements fresh (1 day after sample preparation) and aged (1-2 weeks after sample preparation) for (a) 3wt%, Batch 1, (b) 3wt%, Batch 2, (c) 5wt% Batch 1. . . . . 151

5.9 Log-log amplitude sweeps showing difference between measurements for 2.5wt% Batch 2 for (a)0.1 $\text{rads}^{-1}$ , (b)1 $\text{rads}^{-1}$ (c)10 $\text{rads}^{-1}$ . 153

5.10 Representative stress-strain plot from which we extract  $\sigma_y$ , as an alternate presentation of values from amplitude sweep experiments shown elsewhere in the chapter. Value extracted marked on plot by cross. . . . . 154

5.11 Log-log steady-state shear Flowcurves with Couette cell measurements for a range of Batch 2 measurements presented (a)unscaled, (b)scaled as indicated in [Table 5.1](#). . . . . 155

## LIST OF FIGURES

---

6.1	Observed Volume Fractions of Sheared simulations. . . . .	163
6.2	MSD of systems with $\zeta_e = 1.0$ and varied $\dot{\gamma}$ : (a)Simple MSD, (b) MSD divided by $\tau$ . . . . .	166
6.3	MSD of systems with $\zeta_e = 0.7$ and varied $\dot{\gamma}$ : (a)Simple MSD, (b) MSD divided by $\tau$ . . . . .	167
6.4	MSD of systems with $\zeta_e = 0.7, 1.0$ and varied $\dot{\gamma}$ for comparison: (a)Simple MSD, (b) MSD divided by $\tau$ . . . . .	168
6.5	Flowcurve of systems with $\zeta_e = 1.0$ and varied $\dot{\gamma}$ . . . . .	169
6.6	Magnitude of normal stress differences for all sheared simulations. If not visible, error bars smaller than markers. (a) $N_1$ for $\zeta_e = 0.7$ , (b) $N_1$ for $\zeta_e = 1.0$ , (c) $N_2$ for $\zeta_e = 0.7$ , (d) $N_2$ for $\zeta_e = 1.0$ . . . . .	172
6.7	Averaged scattering amplitude for the $x - y$ planes for all sim- ulations at given parameter values. Results shown for $\zeta_e = 0.7$ , $K = 2\text{kPa}$ at various shear rates: (a) $10^2\text{s}^{-1}$ , (b) $10^3\text{s}^{-1}$ , (c) $10^4\text{s}^{-1}$ , (d) $10^5\text{s}^{-1}$ . . . . .	174
6.8	Averaged scattering amplitude for the $x-y$ planes for all simulations at given parameter values. Results shown for $\zeta_e = 1.0$ , $K = 2\text{kPa}$ at various shear rates: (a) $10^2\text{s}^{-1}$ , (b) $10^3\text{s}^{-1}$ , (c) $10^4\text{s}^{-1}$ , (d) $10^5\text{s}^{-1}$ . . .	175
6.9	$z-y$ plane for simulations at $10^5\text{s}^{-1}$ and at given parameter values. We vary $\zeta_e$ : (a) $\zeta_e = 0.7$ , (b) $\zeta_e = 1.0$ . . . . .	177

# Chapter 1

## Introduction

### 1.1 What is a colloid?

The simplest definition of a colloidal mixture is a phase suspended in another phase, where a discrete unit of the suspended phase typically has a size between 1nm and  $1\mu\text{m}$ . We primarily discuss colloidal suspensions, discrete particles suspended in a liquid, and use the term colloid to refer to these particles. These occur in many places in every day life - in products, and biology - blood, toothpaste and ink to drug delivery, oil recovery and photonics. They are also often used in research laboratories as models for phases of matter, as large scale analogies to both atomic and molecular crystals and glasses. This size range means that quantum effects do not need to be considered, outside of their role in chemical or charge interactions. Their size range also means they are typically thermally active and undergo Brownian motion.

Colloids are often described as ‘hard’ or ‘soft’. Soft colloids are capable of deformation and/or compression, while hard colloids are assumed to be incom-

## 1. INTRODUCTION

---

compressible and have a fixed shape. Additionally, colloids may be characterised by long range interactions which typically have a repulsive and/or attractive component. In hard sphere colloids, short time motion is diffusive rather than ballistic. Hydrodynamics can couple particle motion in complex ways (Di Cola *et al.*, 2009). Colloids are usually spherically symmetric, and when practically created almost always slightly polydisperse (have a distribution of sizes).

### 1.2 Diffusion

A key concept to introduce is diffusion, or more precisely ‘self diffusion’, which acts to set the rate of dynamics in colloids. Let  $\underline{x}(t)$  be the position of a colloid at time  $t$  in a quiescent fluid. Although there is no large scale motion, individual colloids will be subject to random, uncorrelated collisions with solvent molecules, causing a displacement  $\Delta\underline{r} = \underline{x}(t+\tau) - \underline{x}(t)$  after a time lag  $\tau$ . The average particle displacement  $\langle \Delta\underline{r} \rangle$  is zero. However, the mean square displacement (MSD):

$$\langle \Delta r^2 \rangle = \langle (\underline{x}(t+\tau) - \underline{x}(t)) \cdot (\underline{x}(t+\tau) - \underline{x}(t)) \rangle \quad (1.1)$$

where  $\langle \rangle$  indicates an average over all particles and all initial times  $t$  for a time lag  $\tau$ . For an isolated spherical particle of radius  $R$  in a solvent of viscosity  $\eta$ , the MSD is:

$$\langle \Delta r^2 \rangle = 6D\tau \quad (1.2)$$

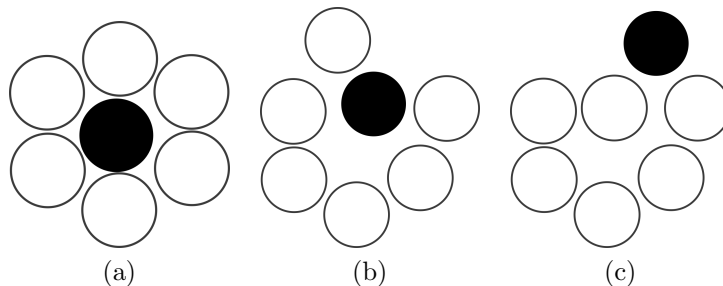


Figure 1.1: Schematic representation of cage-breaking or rearrangement through collective motion of hard particles. Note that the cage must break entirely and particles experience significant change in their centroid position.

For free diffusion, with no other colloids or hindrances in the suspension, MSD grows linearly with  $\tau$ . Here  $D$  is given by

$$D = \frac{k_B T}{6\pi\eta R}, \quad (1.3)$$

the Stokes-Einstein-Sutherland equation, where  $k_B$  is Boltzmann's constant and  $T$  is the system temperature (Einstein, 1905). This sets the diffusive timescale  $\tau_D = \frac{R^2}{6D}$ , or the average time needed for a particle to diffuse its own radius. As the concentration of colloids increases they begin to sterically confine each other.

A colloidal glass occurs when the proportion of the continuous medium is reduced such that relative motion of the colloids is strongly hindered by inter-particle interactions. In a concentrated hard-sphere colloid, movement of the colloids past each other requires a rearrangement of the nearest neighbours of the colloid, referred to as "cage-breaking", which in turn requires those neighbours to break their cages, shown schematically in Figure 1.1. Cage breaking therefore requires collective movement of multiple particles, which under thermal fluctuations may be unlikely or even virtually impossible. However, if the parti-

## 1. INTRODUCTION

---

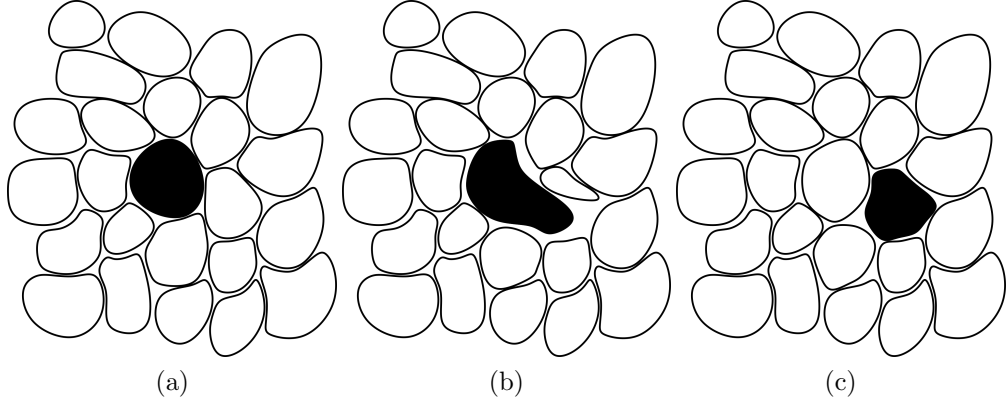


Figure 1.2: Schematic representation of cage-breaking or rearrangement through collective motion of soft particles. Note that few of the caging particles experience significant change in their centroid positions.

cles are soft, rearrangement may require much less displacement of neighbouring particles as each particle can elastically deform (Mattsson *et al.*, 2009; Rahmani *et al.*, 2012). Colloids are structured objects and can be deformable, which may facilitate cage-breaking through deformation allowing lower required movement per colloid (shown schematically in Fig. 1.2) and altering properties in shear flow (Rahmani *et al.*, 2012).

The effects of steric hindrance can be observed in the MSD. At short times the MSD grows linearly, but as the colloids feel a caging effect their MSD will begin to plateau, as they are prevented from moving beyond their local cage. If they are entirely trapped, this plateau will continue indefinitely, but if they are able to rearrange, a second diffusive regime will occur at longer timescales after the plateau, as the colloids enter a diffusive regime between cages. For hard colloids, these cages will become kinetically arrested at high enough volume fraction, but as soft colloids can compress and deform, they may continue to rearrange even

at very high volume fractions. This is a key question we wish to study - to what extent does the ability of our colloids to compress and deform allow rearrangement at high volume fraction and how does this affect dynamics and structure?

### 1.3 Hard and soft colloids

Hard sphere colloids are defined as having an excluded-volume interaction potential:

$$U(r) = \begin{cases} \infty, & \text{if } r \leq 2R \\ 0, & \text{if } r > 2R \end{cases} \quad (1.4)$$

where  $R$  is the sphere radius and  $r$  is the distance between their centres. When practically implemented for simulations or modelling this is usually softened slightly, with a slight ramp up to allow for numerical stability (Hirschfelder, 1939).

If no other interactions are present in the system, the only variable that can affect the dynamics is the volume fraction  $\phi$  (Hoover & Ree, 1967):

$$\phi = \frac{V_0}{V_{System}} \quad (1.5)$$

where  $V_0$  is the volume of the colloids and  $V_{System}$  is the volume of the system. For a monodisperse system, where all colloids are the same size,  $V_0 = nV_{Colloid}$  where  $n$  is the number of colloids and  $V_{Colloid}$  is the volume of each colloid. The phase diagram for hard spheres is shown in Figure 1.3. The particle size may affect the rate of system evolution due to diffusion, but does not affect the phase diagram. At volume fractions  $\phi$  below 0.494, the suspension is a liquid. Above this we may have supercooled or glassy states, which involves increasing

## 1. INTRODUCTION

---

$\phi$  fast enough to prevent crystallisation. Between  $\phi = 0.494$  and  $0.58$ , we have a super cooled state, and between  $0.58$  and the limit of random close packing,  $0.64$ , a glassy state is possible (Hunter & Weeks, 2012). To achieve a glassy state requires somewhat polydisperse colloids (with a distribution of sizes) to frustrate crystallisation (Pusey *et al.*, 2009). Glasses can be characterised as solids that lack long range order. While crystals have a Bragg diffraction signal, glasses do not. Short range order may be present but bulk crystallisation is frustrated. From  $0.64$  to  $0.74$ , samples must be partially crystallised. Volume fractions above  $0.74$  must again have some amount of polydispersity, as  $0.74$  is the limit of monodisperse close packing in the form of hexagonal close packing.

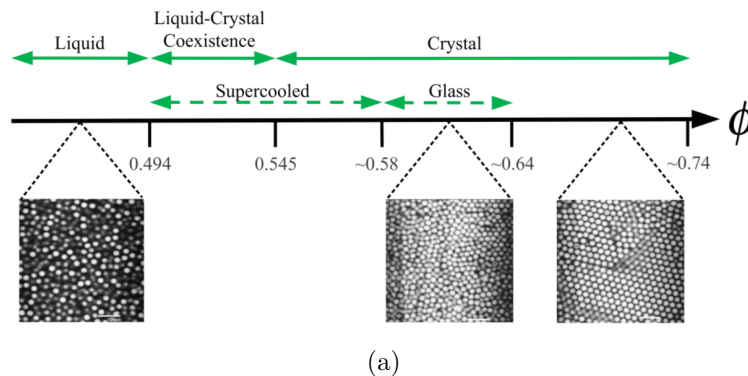


Figure 1.3: Phase diagram of monodisperse hard spheres as a function of volume fraction  $\phi$ . Equilibrium states are indicated by solid arrows while dashed arrows are non-equilibrium states. Glassy states require at least 8% polydispersity. Image reproduced from Hunter & Weeks (2012).

In soft colloids it is possible to exceed this random packing threshold due to the deformability and compressibility of the particles. For this reason it is useful to define a modified volume fraction for compressible objects (Mattsson *et al.*,

2009):

$$\zeta_e = \frac{nV_0}{V_{Tot}}, \quad (1.6)$$

where  $n$  is number of particles and  $V_0$  is the uncompressed, undeformed volume of each colloid, assuming they are monodisperse. This volume fraction may exceed unity. [Mattsson \*et al.\* \(2009\)](#) find that varying this at a steady temperature affects the fragility of the system in a manner similar to varying temperature in a molecular glass (where a lower temperature would lead to an increase in viscosity), and therefore the study of these systems may provide greater insight into glass formation in general. Fragility of the glass refers to its sensitivity to a change in temperature or particle concentration at the glass transition, and the disruption or rearrangement due to changes to the local environment.

Real examples of colloids are unlikely to have a true spherical form that fully excludes volume at all radii ([Royall \*et al.\*, 2013](#)). This is often dealt with by defining an effective radius, such as the radius of gyration, or an effective interparticle potential, that is softer than for hard colloids, which we will discuss later. When used as practical model systems, these are often treated in ways that sterically stabilise them, or the solvent is chosen to minimise the effects of gravity, which can be relevant.

Both hard and soft colloids can interact through steric, attractive and repulsive interactions, and these can be localised to specific sites on the colloid. Attractive interactions include Van der Waals or osmotic interactions. Repulsive interactions include steric interactions, charge, osmotic interactions, or magnetism.

Caging behaviour can actually be stronger for a highly packed soft system than

## 1. INTRODUCTION

---

in a hard particle system (Romeo *et al.*, 2012). Average particle displacement may be lower as each particle can deform to move a smaller distance out of the way, but a result of this is that movement can be coordinated in collective strings of highly displaced fast particles. In general soft glassy systems exhibit coordinated motion with significantly longer lengthscales, spanning the whole system, whilst having much shorter relaxation timescales (Rahmani *et al.*, 2012). This suggests soft colloidal glasses are dynamically distinct from hard colloids.

When discussing interactions of soft colloids, an additional complication is present in that the word soft can have multiple meanings. Simulations of soft colloids often use spherically symmetric potentials, running from simple  $\frac{1}{r^n}$  potentials where smaller values of  $n$  correspond to softer colloids, to Hertzian-derived potentials that take faceting into account and that are modified to consider electrohydrodynamics. However, softness in experimental colloids may be more complex, with multiple meanings of softness (De Michele *et al.*, 2011; Mattsson *et al.*, 2009) and with the difficulty of arriving at a simple measure for deformation due to multiple contacts (Höhler & Weaire, 2019). For some systems softness can be defined from experimental elastic moduli measured for spherical colloidal particles, but is more complex for other structures such as star polymers, that do not map easily onto traditional spherical models, especially when undergoing forcing.

### 1.3.1 Polymer microgels

Polymer microgels are a common form for both hard and soft colloids. Their internal structure arises from five inter-molecular forces (Sierra-Martin *et al.*, 2011); Van der Waals, hydrophobic interactions, hydrogen bonding, electrostatic inter-

## 1.4 Experimental characterisation

---

actions, and osmotic pressure due to the presence of ions/counter ions introduced during creation of the polymer. These interactions can be altered and therefore swelling can be controlled by the choice of solvent (Perry, 1987). Hydrogen bonds break at higher temperatures, causing deswelling which can be discontinuous (Shenoy *et al.*, 1999). Hydrophobic interactions increase in strength with temperature, but actually drive deswelling themselves, as the polymer seeks to minimise exposed surface area. However, this is a weak interaction. Electrostatic groups may interact with each other, but the primary source of swelling due to the presence of electrostatic regions is osmotic pressure. As these all depend on distance between each polymer strand, the structure of each microgel may affect the elastic response. For example, Stieger *et al.* (2004) find a flat density profile in a dense core that then decays gradually to the outer limit of the particle, though they can be made more homogeneously crosslinked (Witte *et al.*, 2019). Simulating these microgels as continuum objects may require these discontinuities and density profiles to be taken into account. These interactions are common amongst a wide variety of colloids.

It is also possible to use a broad variety of experimental techniques to study these systems, as the time and length scales can be experimentally accessible - a particle with  $\mu\text{m}$  diameter can diffuse its own diameter in approximately a second, which makes observation tractable for optical microscopy and light scattering.

## 1.4 Experimental characterisation

Common experimental techniques used to explore the dynamics and structure of soft colloidal systems are: optical microscopy, including video microscopy,

## 1. INTRODUCTION

---

confocal microscopy and particle tracking; static and dynamic light scattering; and rheology.

In video microscopy, a camera is attached to a microscope and used to capture images, which are then stored for later analysis. Common forms of microscopy include brightfield and fluorescence microscopy. Brightfield microscopy functions through scattering or absorption of light by the the sample for image contrast. As this depends on the optical properties of the sample, dyes or related techniques that aim to improve contrast may need to be used. As a traditional microscope illuminates the entire sample and therefore has difficulty resolving three dimensional motion, this technique is easiest to implement in the study of two-dimensional samples.

Fluorescence microscopy is is similar, but the sample is tagged with a fluorescent dye, and high energy light is used to illuminate the sample, which excites the dye and emits light at a lower wavelength. An advantage of this is that specific objects can be tagged, such as the colloids in a suspension, or a particular kind of colloid, if the suspension is a mixture. However the introduction of this sort of dye can have issues. As the dye is expected to interact with some part of the system, it naturally can influence interactions, such as introducing a slight charge. Additionally, the dye is eventually degraded through contact with light and oxygen, known as photobleaching.

To effectively use optical microscopy in three dimensions, confocal microscopy is often used. This technique still uses fluorescence, but avoids issues with dense systems where objects outside the focal plane are fluorescing, producing bright objects against a bright background. This is achieved through illumination of a small sample volume, and rejection of out of focus light ([Prasad \*et al.\*, 2007](#)).

## 1.4 Experimental characterisation

---

Laser light is emitted and passes through a dichroic mirror, and onto rotating mirrors that scan light in horizontal planes. This light enters the microscope optics and excites the sample. The light then follows the reverse path, again passing through the dichroic mirror, which reflects it onto a screen with a pinhole before collection by a detector. This acts to reject light not in focus and limits depth of field (Habdas & Weeks, 2002). This technique allows two and three dimensional observations to be taken.

Particle tracking is the computational analysis of the collected visual data to identify centroids of particles in images and track them between images (Crocker & Grier, 1996; Habdas & Weeks, 2002). This allows access to both structural and dynamical information, although difficulty can be encountered when attempting to identify a particular particle across multiple frames, essential for the retrieval of dynamical data. Challenges may include small sizes of particles, poor contrast, sedimentation, and highly crowded samples. Using video microscopy, one may recover behaviour of individual particles or the behaviour of a population of up to several thousand.

Light scattering can also be used to probe average structure and dynamics of a system. A laser is shone through a sample, and a detector is placed at a given angle to detect scattered light. The scattered light interferes with itself, and the details of this interference at different angles allow reconstruction of information about structure of the sample. Of common interest is the static structure factor  $S(k)$ , which provides information about the spatial correlation between objects in the medium, reflecting interactions between scattering elements or concentration

## 1. INTRODUCTION

---

fluctuations. Here  $k$  is the wave vector of the scattered light, given by

$$k = \frac{4\pi n}{\lambda} \sin\left(\frac{\theta}{2}\right), \quad (1.7)$$

where  $n$  is the refractive index of the sample medium,  $\lambda$  is the the laser wavelength and  $\theta$  the angle between the incident and detected light (Jones & Pusey, 1991).

When performing investigations using dynamic light scattering, fluctuations in light intensity  $I(t)$  are analysed as functions of time. The fluctuations in time arise from motions of the particles within the sample volume. This measure fluctuates with rearrangements in the sample, affecting the interference pattern of the scattered light. Of specific interest is the autocorrelation function of intensity,

$$g_2(\tau) = \frac{\langle I(t + \tau)I(t) \rangle_t}{\langle I(t) \rangle^2} \quad (1.8)$$

and fluctuations with time lag  $\tau$ . This decays with increasing  $\tau$  from a maximum value at  $\tau = 0$ . Measuring the rate of decay gives information about particle movement, including data related to the diffusion coefficient. If the particles move on the order of the length-scale probed (inversely related to the  $k$ -vector chosen), the two intensities in Equation 1.8 are uncorrelated, so the correlation will decay to zero. By determining the relevant time scale for this decay for a diffusive system, the diffusion coefficient will be given by the square of the length scale over the time scale. Altering  $k$  will allow probing of local or collective particle dynamics. The autocorrelation function may be calculated from very short timescales ( $10^{-6}$ s) to days or weeks. Accurate MSD measurements for an entire system are relatively easy to recover, but local dynamics are much more

## 1.4 Experimental characterisation

---

difficult to measure due to ensemble-averaging (Jones & Pusey, 1991).

An advantage of recovering this information through light scattering is it allows for smaller colloids to be used. Additionally, colloidal suspensions near a glass transition become difficult to treat, as they do not rearrange enough to have confidence in the time-average from the sample, though there are workarounds. Another issue is that light is often scattered multiple times in a dense suspension, which can be mitigated by techniques such as Diffusive Wave spectroscopy, particularly useful in multiply scattering systems with small motions such as dense colloidal systems (Pine, D.J. *et al.*, 1990).

Finally, rheology is the study of material flow and deformation. In most situations, common fluids will exhibit a Newtonian response, i.e. one where the stress  $\sigma$  is related to the viscosity  $\eta$  of a fluid by:

$$\sigma = \eta \dot{\gamma} \tag{1.9}$$

where  $\dot{\gamma}$  is the the shear rate.

Where the material is viscoelastic, and has a mixed solid and liquid like response depending on the applied shear rate, one would apply a varying strain of the form

$$\gamma = \gamma_0 \sin(\omega t) \tag{1.10}$$

where  $t$  is time,  $\omega$  is the frequency of oscillatory stress and  $\gamma_0$  is the maximum amplitude of the oscillating strain. In the linear regime, the measured stress is:

$$\sigma(t) = \gamma_0 (G'(\omega) \sin(\omega t) + G''(\omega) \cos(\omega t)) \tag{1.11}$$

## 1. INTRODUCTION

---

Here  $G'(t)$  and  $G''(t)$  are the conservative, elastic contribution to the shear modulus, and the viscous dissipative contribution to the shear modulus, respectively. These are often referred to as ‘solid-like’ and ‘liquid-like’ behaviours. Rheometers either create a constant or oscillatory stress and study the deformation response, or measure the stress required to deform a material at a constant rate of strain.

A key difference in Newtonian and non-Newtonian fluids is that Newtonian fluids have only a single, scalar viscosity, whereas viscoelastic materials have a viscosity tensor which can be different for each direction and involve interactions between directions.

The conceptually simplest version of a rheometer and geometry would be a cone shaped plate above a circular plate, where the bottom is fixed and the top can be rotated in a well controlled manner. Shear is then applied to this by rotating the top plate. The cone shaped geometry of the upper plate means shear is consistent through the radius of the plate. Examples of this for an idealised solid-like and liquid-like situation can be seen in [Figure 1.4](#). An idealised solid is displaced by the movement of the top plate perfectly, while the idealised liquid depends on the current rate of applied shear. As above, shearing can be

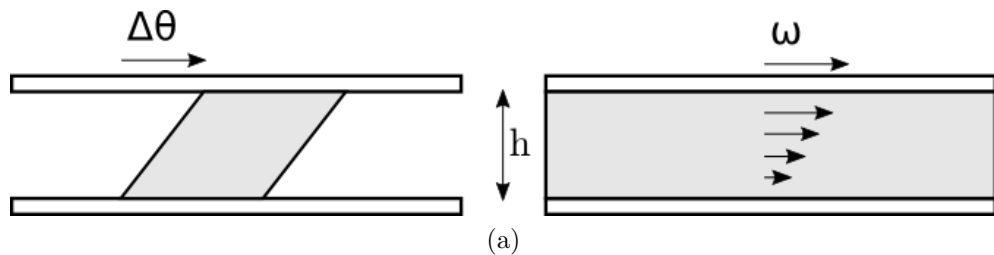


Figure 1.4: Schematic of simple rotational rheometer with cone-plate geometry viewed from the side, describing the edge of the plate, with idealised solid-like behaviour on the left and idealised liquid like behaviour on the right.

sinusoidal and oscillatory, probing structure and morphology of a material with

## 1.4 Experimental characterisation

---

small oscillations. By increasing the the amplitude of the oscillations, the internal mechanisms of stress relaxation may be probed. The structure of the system is disrupted by these large amplitude oscillations, and by varying their timescale the relaxation timescale can be investigated.

Another class of common shearing investigations is rotational steady shear, where the sample is simply sheared in one angular direction at a consistent shear rate, investigating the bulk response to simple linear shear. A complication of these sort of steady state shear measurements is that it can take some time to reach a steady state - strain may eventually destroy the structure of the sample, and a steady state will not be reached until the structure is destroyed and is flowing freely. In this case, there will be a transient stress that is higher, as stress builds, relaxes, and then reaches a steady state.

Additionally, many materials or suspensions may not flow until a minimum amount of force is exceeded, known as the yield stress. In dense colloidal suspensions, this is often the forcing required to break the cages of the suspended particles, often adapting a flow induced arrangement typically including layering. Under this yield stress, the sample acts like a solid, with  $G'$  greater than  $G''$ . Above, it begins to flow, and  $G''$  is the greater (Pham *et al.*, 2006).

Dense colloidal suspensions, both hard and soft, are likely to be viscoelastic (Mason & Weitz, 1995), as the response of the system in general will often depend on the dynamics and structure of the suspended particles in a complex way, for example forming chains of particles, depletion through force increasing friction, or shear thinning due to forming attractive clumps.

Macrorheology, or the response of a material bulk is mainly studied through the use of a rheometer between various measuring geometries designed to measure

## 1. INTRODUCTION

---

different systems, but video microscopy, particle tracking and light scattering can also be used for microrheology alongside this. Microrheology is concerned with local, microscopic properties, and these microscopic dynamics and structure can relate to the macrorheology of the system.

In general, the motion of a bulk material may not be homogenous, especially under forcing. Different regimes of a system may relax differently, stress may be trapped in certain areas of systems, or there may be sub populations of particles with differing dynamics (Ediger, 2000; Richert, 2002; Sillescu, 1999). Often, in very densely packed suspensions, cooperation is necessary for stress relaxation (Adam & Gibbs, 1965). As mentioned previously, for hard spheres this often involves significant displacements of the centroids around a particle to allow it to break its cage, but for soft spheres this can be compressions or deformations, allowing rearrangement with much smaller centroid displacement, and this can happen in system-spanning strings. This necessitates an understanding of the microrheology to effectively design for the macroscopic results desired.

### 1.5 Simulation techniques for colloidal systems

To date, simulations of colloidal particles have mainly been carried out using hard sphere or radially-symmetric soft sphere potentials (Hunter & Weeks, 2012). Hard sphere potentials are usually considered as infinite if particles are overlapping. For the simplest case in Equation 1.4, the potential is zero if particles do not overlap, but friction or longer range forces such as electrostatics can also be considered. For soft colloids Equation 1.4 can be replaced by a softer repulsive potential. Such radially symmetric soft sphere potentials consider only the core-

## 1.5 Simulation techniques for colloidal systems

---

to-core distance between particles. This ignores effects that arise where soft spheres become anisotropically deformed (Höhler & Weaire, 2019).

Winkler *et al.* (2014) comment on several theoretical approaches employed in recent years. They conclude that systems of soft colloidal particles exhibit several generic behaviours, such as "tank-treading" (where the particles deform continuously so that the axis of deformation is fixed in space and thus appear similar to tank treads while rotating), as well as tumbling motions. These behaviours are found in different soft matter systems, including star polymers, vesicles, soft capsules, red blood cells, and linear polymers. However, they comment that while similar phenomena may be present, the quantitative or qualitative properties differ greatly; a polymeric system does not necessarily have an internal viscosity, whereas an encapsulation might, and therefore care should be taken when generalising findings across systems.

De Michele *et al.* (2011) conducted simulations with radially symmetric 'softer' repulsive potentials, with more rapidly decaying inverse power laws that weakly exclude volume. They did not find the dependence of fragility on particle softness that Mattsson *et al.* (2009) observe. However, Mattsson *et al.* (2009) use softness to refer to the elastic moduli of the particles, as well as their charged nature giving an additional contribution of softness, rather than the strength of an excluding potential. While these are linked, it is not clear they are interchangeable.

A number of approaches to colloidal simulation use Hertzian potentials (Berthier *et al.*, 2010; Seth *et al.*, 2011), obtained from the analytic solution of the compression of an elastic particle due to a faceting contact. Seth *et al.* (2011) propose a micromechanical three-dimensional model that predicts nonlinear rheology of soft glasses. This potential is based on the overlap of the particles and is effectively

## 1. INTRODUCTION

---

radially-symmetric, and approximates an elastic contact force, which cannot account for multiple contact deformation of a continuous object. Additionally, it uses an elastohydrodynamic drag force parallel to the implicit facet, arising due to the existence of thin films of solvent between these facets during shear deformation. This was successfully validated with model systems in shear situations, using a Hertzian potential at low shear modified at high shear to model elastic interactions between particles. They find that the elastic contact forces dominate the dynamics compared to the thermal energy, and find general behaviour of the soft glasses arises from a combination of both the elasticity of the particles particles and their structural rearrangements. This collaboration between research groups also found in [Liu \*et al.\* \(2018\)](#) that results are not highly sensitive to the exact form of the elastic overlap interaction potential. This investigation modified the Hertzian potential to more appropriately deal with larger overlaps, attempting to elucidate the minimal interparticle interactions necessary for soft particle glasses. By using this simulation technique and forcing motion of select particles through a frozen colloidal glass, [Mohan \*et al.\* \(2014\)](#) find some agreement between the microrheology they observe and macrorheology. An advantage of this model is the inclusion of the elastohydrodynamic interactions which may be important to "lubricating" cage-breaking and rearrangement.

[Berthier \*et al.\* \(2010\)](#), using Hertzian potentials, find a reentrant behaviour - increasing density results in fluid-glass-fluid transitions, due to particle softness. This is also seen in the more computationally complex simulations of [Gnan & Zaccarelli \(2019\)](#); [Lo Verso \*et al.\* \(2016\)](#), though this results from particle deformation leading to accumulation of internal stresses, unlike Hertzian systems, where this results from significant overlap.

## 1.5 Simulation techniques for colloidal systems

---

The relaxation of stress after shear is relevant to the phenomenon of glass ‘aging’, which is the process of a glass relaxing due to thermal motion or otherwise as time passes, towards a true equilibrium state if one exists. Even though glasses may be stable over extremely long timescales, their disordered nature can mean they are not at a global free energy minimum. They find that relaxation occurs quite differently when shear is switched off in a plastic-flow regime to an elastic regime, with the former being much more rapid, and that these can be distinguished by observing the local stress. [Zausch & Horbach \(2009\)](#) performed simulations of soft spheres to probe relaxation of stress after shear. They implement a Yukawa potential, which is also radially-symmetric but acts at longer ranges than the nominal particle radius.

[Das \*et al.\* \(2020\)](#) use a simple harmonic potential of a binary mixture of athermal soft spheres, using cyclic shearing to construct a phase diagram including isolating phase space for reversible and irreversible transitions. They also observe jamming and yielding transitions, all in a frictionless system. The amorphous solids yield at a well defined strain, and they investigate contact number as it relates to shear stress - if this is below 6, shear stress discontinuously goes to zero. They find a jamming regime at  $\phi = 0.648$ , which then unjams at  $\phi = 0.661$ . Below this, there are 2 varieties of reversible phase present - one that is point reversible, where particles self organise back into a similar layout to their starting, and one that is loop reversible, where original particle positions can be recovered as the shear cycles. Above this regime, it behaves as an elastic amorphous solid. This shows the rich behaviour of even simple colloid models.

Another class of approaches to colloidal simulations is Multi-Particle Collision Dynamics (MPCD). This is a particle based simulation technique, including ther-

## 1. INTRODUCTION

---

mal fluctuations and hydrodynamic correlations, whilst being capable of coupled with MD for the microgels. In this approach, the solvent is modelled explicitly, by coarse-grained particle dynamic approximations. This method and DPD methods are effectively similar particle based approaches that consider Fluid Dynamics, but make different approximations and use different models to do so. For example, [Malevanets & Kapral \(1999\)](#) use this approach coupled with coarse-grained linear polymers with tetra-functionally crosslinked monomers to directly investigate internal polymer dynamics in responsive microgels, observing conformational changes due to external stimuli. [Tran \*et al.\* \(2018\)](#) implement MPCD efficiently on Graphics Processing Unit (GPU) hardware. An advantage of MPCD approaches is the detailed representation of hydrodynamic and friction ([Theers \*et al.\*, 2016](#)), although they tend to be focussed on relatively dilute regimes.

A further class of approaches to colloidal simulations are Lattice-Boltzmann methods. Lattice Boltzmann approaches fluid simulation through a kinetic model of fluid particle velocity distributions confined to a lattice. The advantages of this approach are its ability to parallelise easily and to treat complex boundaries. [Rivas \*et al.\* \(2018\)](#) use this approach with submerged spherical particles, which when projected onto the LBM lattice introduce structure to the particles, with solid fraction and ion concentration in the solvent varying within the particle - this treats particles in a somewhat structured way, while simple enough to allow direct simulation of colloid coated droplets and their breakup, particles at fluid interface and electrophoresis.

Another example of LBM simulation for soft flowing systems is the work of [Fei \*et al.\* \(2018\)](#). This treats the suspension as a binary mixture, and allows significant distortion, but in this case is limited to two-dimensions and small numbers of

## 1.5 Simulation techniques for colloidal systems

---

particles. Despite that, it reaches relatively high volume fractions. This method appears more suitable for approaching flow undergoing forcing, rather than quiescent systems.

Depletion effects can be important to colloidal systems, as the work by [Stopper \*et al.\* \(2016\)](#) simulates. This approach uses the Asakura-Oosawa model for depletion effects, which is again spherically symmetric. Mixtures of polymers and colloids are simulated, and dynamical density functional theory is used to construct the van Hove distribution function for a dilute system.

[Fedosov \*et al.\* \(2012\)](#) compare both Dissipative Particle Dynamics (DPD) and MPCD approaches in simulations of star polymers which offer a similar paradigmatic model as microgels for soft colloids, but their approach uses multiple single branch chains emanating from a core representing a quite different particle than a crosslinked system such as microgels. Their DPD approach uses radially symmetric potentials between monomers, with a general ball and spring model between bonded monomers in the same colloid. These demonstrate marked dependence on arm length and arm number, transitioning from soft-sphere to hard-sphere. This allows consideration of the variance in structure in microgels, as these can be cross-linked to a greater or lesser extent, or may be grown around a hard core. They also exhibit lengthening under shear, an example of tank-treading, but as the arms are not linked they may be more susceptible. They find that there is small difference in absolute value found for key outputs, such as characteristic arm relaxation time, but that these hydrodynamic approaches largely agree.

[Locatelli \*et al.\* \(2016\)](#) use a multi-scale approach for star polymers as soft spherical potentials in a mixture with coarse-grained linear polymers, coarse-graining where they expect a departure from simple soft sphere behaviour, al-

## 1. INTRODUCTION

---

though this publication represents a validation of the method against more detailed approaches rather than presenting new results.

Another approach to soft colloidal simulation is that of [Gnan & Zaccarelli \(2019\)](#). While these simulations are two-dimensional, they utilise a very different approach to most others reviewed. Here, each colloid is simulated as a ring of circular particles, with a Weeks-Chandler-Andersen (WCA) and Finitely Extensible Nonlinear Elastic (FENE) potential between neighbouring members of the ring, and a Hertzian potential from each particle to the edge of the ring. This allows for more complex deformation, and to go to a high effective packing fraction. The most relevant observation is that of a second diffusive regime between cages in all cases. These simulations can also measure and report on deformation and its correlation with movement, and observe strings of correlated super-diffusive movement. They observe a variation with softness of the relaxation time dependence on packing fraction, which provides an effective dynamic fragility parameter.

Another technique that treats soft colloids as structured materials, in this case in three dimensions, is that of [Lo Verso \*et al.\* \(2016\)](#). They use a Langevin dynamics monomer-resolved bead-spring model, validated against MPCD, to simulate globular single-chain nanoparticles, which consist of a linear polymer with side chains, such that volume of the polymer appears globular. Increasing the concentration shows reentrant behaviour in structure and dynamics, a soft caging regime and weak dynamic heterogeneity. They find that the Stokes-Einstein-Sutherland relation persists above overlap density, and reach effective volume fractions of 2.7. They investigate the shape and find a tendency to be prolate, due to the backbone of the particle. They also find no crystallisation, and that the system is

always fluid.

## 1.6 Key research questions

We can see from the previous section a number of approaches to simulations of colloids. Simulations with simple radially symmetric potentials allow a large number of particles to be simulated, but these are largely athermal - they do not allow spontaneous rearrangements past contact packing fraction through thermal motion. The existence of ultrasoft colloids suggests that there are situations where thermal motion remains important even when the system is not being forced. Many simulations that represent colloids with more complex, deformable structures consider very dilute regimes, or small numbers of colloids due to the computational expense. Simulations that represent colloids as being structured and deformable suggest that soft colloids retain the ability to rearrange even at very high volume fractions. However, simulations of these types of system with reasonable numbers of colloids use simplistic bead-spring models for the colloidal particles, which will become less accurate as the coarse-graining increases.

There is therefore a need for an approach capable of considering the volumetric compression and deformation of thermally fluctuating material as a continuum. Additionally, as the colloids are further coarse-grained, continuum methods will become more accurate rather than less. For this reason, we choose the method Fluctuating Finite Element Analysis, as detailed in [Chapter 2](#).

Our key research questions involve the structure and dynamics of soft colloidal suspensions.

- Is the ability to describe these deformations due to thermal motion enough

## 1. INTRODUCTION

---

to alter the dynamics in highly packed systems?

- How does varying the volume fraction or material parameters of the particles affect rearrangement?
- How does this correspond to experimental examples of ultrasoft colloids?
- What effect does shear have on the structure and dynamics of these soft colloidal simulations?
- Can we construct bulk rheology from microscopic simulations?

### 1.7 Thesis outline

In this thesis, we present the further development and usage of Fluctuating Finite Element Analysis (FFEA), a simulation technique that began development in [Oliver \*et al.\* \(2013\)](#). This technique was initially implemented to model the dynamics of globular biomolecules, but is also a suitable technique to provide novel insight into the dynamics, structure and rheology of soft colloids. [Chapter 2](#) discusses FFEA, including the underlying mathematical model and the particular aspects that make it suitable for simulating soft colloidal systems. [Chapter 3](#) describes the development of FFEA required to simulate soft colloidal systems. In [Chapter 4](#) we then discuss the results of simulations of quiescent (i.e. unforced) packed soft colloidal systems, and present analysis of dynamics and structure. We vary material parameters and degree of packing, and investigate effective and observed volume fractions, diffusive behaviour, rheological measures, asphericity and light scattering. [Chapter 5](#) discusses experimental rheology conducted on ultrasoft microgels. This includes both steady state and oscillatory rheology.

Finally, in [Chapter 6](#) we simulate systems undergoing linear shear and discuss the results and analysis obtained. We vary degree of packing and shear rate, and discuss effective and observed volume fractions, diffusive behaviour, rheological measurements and light scattering.

## 1. INTRODUCTION

---

## Chapter 2

# Fluctuating Finite Element Analysis (FFEA)

In [Chapter 1](#), we discussed that most simulations of soft colloidal systems are based on spherically symmetric potentials, i.e. potentials which depend only on the distance between particles. These methods of simulation may miss effects arising from anisotropic deformation of the colloidal particles; one would expect the interparticle potential to depend upon the current particle shape. Likewise, systems based on isotropic potentials do not account for variations in interaction energy due to multi-particle contacts, and therefore are most accurate for considering particles that deform only slightly, or facet at contact but do not experience significant deformation such as the objects in the simulations of [Khabaz \*et al.\* \(2017, 2018\)](#).

We must therefore use a model that is able to capture the three-dimensional deformability of soft colloids, and specifically microgels with their three-dimensional structure. Soft colloids are objects which can change their shape and volume,

## 2. FLUCTUATING FINITE ELEMENT ANALYSIS (FFEA)

---

swelling with solvent and deswelling with its absence, as well as interacting with neighbouring particles. To reflect these attributes, we chose a simulation technique called Fluctuating Finite Element analysis (FFEA). This was developed as a method for simulating the dynamics of biomolecules by modelling them as viscoelastic solids, developed originally by [Oliver \*et al.\* \(2013\)](#) and further refined into a C++ implementation by [Richardson \(2014\)](#).

In FFEA, each biomolecule is envisaged as a deformable object. The objects can change shape, with an internal stress arising from internal elasticity (parametrised by moduli) and internal viscosity, and a stochastic thermal stress from Brownian motion. This thermal stress gives rise to fluctuations in the shape of the object. Interactions between objects can be introduced as a steric force preventing overlap, and also specific surface-surface interactions such as Lennard-Jones interactions. The technique aimed to cover larger timescales (up to  $1\mu s$ ) and length (in the range of  $5nm$  to  $1\mu m$ ) scales of biomolecular simulation that full atomistic simulations cannot currently reach with available computational resources, allowing more complete exploration of their conformational space.

Although FFEA was developed for biomolecules, it has all the ingredients we require for simulation of soft colloids: internal elasticity of objects, viscous dissipation, thermal fluctuations, and interaction between objects. These ingredients address the deformability, steric interaction and the thermal dependence of the dynamics of soft colloids such as microgels. Additionally, soft colloids are small enough that thermal motion remains important, and large enough for a continuum approximation to be appropriate, rather than an atomistic or coarse-grained molecular dynamics approach.

## 2.1 Mathematical model of FFEA

In FFEA, the material viscoelasticity is modelled using the Kelvin-Voigt constitutive model where viscous and elastic stresses act in parallel. This is chosen to provide a simple non-linear model for a viscoelastic solid.

The equation of motion, Cauchy's momentum equation, is

$$\rho \frac{D\underline{u}}{Dt} = \nabla \cdot (\underline{\underline{\sigma}}^e + \underline{\underline{\sigma}}^v + \underline{\underline{\pi}}) + \underline{f}, \quad (2.1)$$

where  $\rho$  is the density and

$$\frac{D\underline{u}}{Dt} = \frac{\partial \underline{u}}{\partial t} + \underline{u} \cdot \nabla \underline{u}, \quad (2.2)$$

is the material derivative of the velocity with respect to time.

Here, the total stress,  $\underline{\underline{\sigma}}$ , is the sum of three separate stresses:  $\underline{\underline{\sigma}}^e$ , the elastic stress,  $\underline{\underline{\sigma}}^v$ , the viscous stress, and  $\underline{\underline{\pi}}$ , the stochastic thermal stress. The vector  $\underline{f}$  is the external force density which includes all other interactions with the system, including steric interactions with other bodies, and a drag against the surrounding fluid.

The elastic stress  $\underline{\underline{\sigma}}^e$  is assumed to be hyperelastic meaning that the stress-strain response is non-linear with respect to deformation, allowing us to address more significant compression and deformation of our particles as well as considering the internal elastic shear stress in each element. A relatively simple choice of this stress-strain relationship is (Hanson, 2018):

$$\underline{\underline{\sigma}}^e = G \det(\underline{\underline{F}}) (\underline{\underline{F}}^T \underline{\underline{F}} - \underline{\underline{I}}) + \frac{1}{2} \left( K - \frac{2G}{3} \right) \left( \det(\underline{\underline{F}}) - \frac{1}{\det(\underline{\underline{F}})} \right) \underline{\underline{I}} \quad (2.3)$$

## 2. FLUCTUATING FINITE ELEMENT ANALYSIS (FFEA)

---

where  $G$  and  $K$  are the shear and bulk moduli respectively, and  $\underline{\underline{F}}$  is the deformation gradient tensor, defined as

$$\underline{\underline{F}} = \frac{\partial \underline{x}}{\partial \underline{X}}, \quad (2.4)$$

where  $\underline{x} = \underline{x}(\underline{X}, t)$  is the current position of the material initially located at  $\underline{X}$ .

The internal viscous stress is assumed to be isotropic and linear so that it takes the form:

$$\underline{\underline{\sigma}}^v = \mu (\nabla \underline{u} + \nabla \underline{u}^T) + \lambda \nabla \cdot \underline{u} \underline{I}, \quad (2.5)$$

where  $\mu$  is shear viscosity, and  $\lambda$  is the second coefficient of viscosity, related to compressibility.

The statistics of the thermal stress  $\underline{\underline{\pi}}$  must satisfy the fluctuation-dissipation theorem and so depend on the form of  $\underline{\underline{\sigma}}^v$ . As shown by [Oliver \*et al.\* \(2013\)](#), [Equation 2.1](#) can be discretised using the finite element method in a way that enables the thermal stress to be calculated locally. In the finite element method we replace [Equation 2.1](#) with a weak formulation ([Reddy, 2006](#)), which relaxes the requirement for the equation to hold absolutely, and instead only requires solutions to satisfy a set of weighted integrals.

The weak form of [Equation 2.1](#) is obtained by integrating over the volume of the object,  $\Omega$ , with a weight function  $w$ ,

$$\int_{\Omega} w \left( \rho \frac{Du_i}{Dt} - \frac{\partial \sigma_{ij}}{\partial x_j} - f_i \right) dV = 0. \quad (2.6)$$

Here  $\sigma_{ij}$  is the total stress tensor  $\sigma_{ij} = \sigma_{ij}^v + \sigma_{ij}^e + \pi_{ij}$ , and  $i, j$  are indices referring to orthogonal spatial directions. The summation convention is applied. Integrating

the stress term by parts gives:

$$\int w \frac{\partial \sigma_{ij}}{\partial x_j} = \int_{\Gamma} w F_i dA - \int_{\Omega} \sigma_{ij} \frac{\partial w}{\partial x_j} dV \quad (2.7)$$

where  $\Gamma$  is the surface of the object and  $F_i = \sigma_{ij} n_j$  is the surface force density.

The completed weak form of [Equation 2.1](#) is therefore:

$$\int_{\Omega} w \rho \frac{Du_i}{Dt} + \int_{\Omega} \sigma_{ij} \frac{\partial w}{\partial x_j} dV = \int_{\Omega} w f_i dV + \int_{\Gamma} w F_i dA. \quad (2.8)$$

With the derivative on  $w$ , the stress does not need to be differentiable.

In the finite element formulation, velocity at any point in the simulation domain is set by shape functions,  $\psi_{\alpha}(\underline{x})$ :

$$u_i(x) = \sum_{\alpha} v_{i\alpha} \psi_{\alpha}(\underline{x}), \quad (2.9)$$

where  $v_{i\alpha}$  is the value of the  $i$ th component of velocity at node  $\alpha$ . The nodes are fixed to the material frame of the object. In the Galerkin formulation ([Reddy, 2006](#)), the weight functions,  $w$ , are chosen to be equal to the shape functions,  $\psi_{\alpha}$ . [Oliver et al. \(2013\)](#) sought an approximate solution to [Equation 2.1](#) using tetrahedral elements, where  $\psi_{\alpha}$  are chosen to be linear interpolation functions over the element. It then follows that:

$$\frac{Du}{Dt} = \sum_{\alpha} \frac{dv_{\alpha}}{dt} \psi_{\alpha}(\underline{x}). \quad (2.10)$$

[Equation 2.8](#) can then be computed by summing the contributions from each

## 2. FLUCTUATING FINITE ELEMENT ANALYSIS (FFEA)

---

element to give a matrix equation of the form:

$$M_{pq} \frac{dv_q}{dt} = -\Lambda_{pq} v_q + E_p + N_p + O_p, \quad (2.11)$$

where indices  $p = i, \alpha$  and  $q = j, \beta$  run over both nodes,  $\alpha, \beta$  and Cartesian directions  $i, j$ .  $M_{pq}$  is the mass matrix which distributes the density contained within an element to its associated nodes,  $v_q$  is a component of velocity at a node, and  $\Lambda_{pq}$  is the viscosity matrix which is the sum of internal contribution,  $\Lambda_{pq}^{Int}$  and an external component,  $\Lambda_{pq}^{Ext}$ .  $E_p$  is the elastic force vector (a non-linear function of node position),  $N_p$  is the stochastic noise force vector, and  $O_p$  represents all additional conservative external forces. In our case,  $O_p$  contains the steric interaction between elements, which will be discussed in [section 2.2](#).

As in Brownian dynamics, we assume that the system is overdamped, so that the time scale on which the mass affects the dynamics is small compared to the timescale of interest. This assumption is discussed in [Chapter 3. Hanson \(2018\)](#) therefore sought the solution of [Equation 2.11](#) where the mass matrix is zero:

$$\Lambda_{pq} v_q = E_p + N_p + O_p. \quad (2.12)$$

The elastic force vector  $\underline{E}$  can be calculated from an the elastic stress  $\underline{\underline{\sigma}}^e$ :

$$E_{p(i,\beta)} = - \int_{\Omega} \frac{\partial \psi_{\beta}}{\partial x_j} \sigma_{ij}^e dV, \quad (2.13)$$

integrated over the volume of the tetrahedral element.

## 2.1 Mathematical model of FFEA

---

The internal contribution to the viscosity matrix is given by

$$\Lambda_{p(i,\beta)q(j,\alpha)}^{Int} = \int_{\Omega} \mu \frac{\partial \psi_{\beta}}{\partial x_c} \frac{\partial \psi_{\alpha}}{\partial x_c} \delta_{ij} + \mu \frac{\partial \psi_{\beta}}{\partial x_j} \frac{\partial \psi_{\alpha}}{\partial x_i} + \lambda \frac{\partial \psi_{\beta}}{\partial x_i} \frac{\partial \psi_{\alpha}}{\partial x_j} dV. \quad (2.14)$$

Since  $\underline{\nabla}\psi$  is piecewise constant over elements, this is a straightforward sum over elements allowing internal stochastic noise to be calculated locally on each element.

External viscosity from the solvent is applied via a Stokes drag on each node, contributing

$$\Lambda_{pq}^{Ext} v_q = \int_{\Omega} f_i \psi_{\beta} dV \quad (2.15)$$

to the viscosity matrix. For the purposes of this calculation, the drag at each node is modelled by the Stokes drag of a sphere located at that node with an effective radius scaled to the volume of the object to give the correct drag to a coarse-grained sphere, recovering Stokes drag on the scale of the whole object. This is scaled by a variable referred to as  $d_S$ .

The internal viscosity in microgel colloidal systems arises from the solvent moving within and being expelled from or entering the swollen microgel, although the solvent is not modelled explicitly. Additionally, [Equation 2.14](#) shows the internal stresses are decoupled from the solvent drag terms and therefore there is no global viscous coupling, meaning internal and external contributions to  $\underline{N}$  can be considered separately.

As the solvent is not explicitly modelled, there is currently no hydrodynamic coupling between colloids. As we choose systems with effective volume fraction  $\zeta_e$  of 0.6 and above with monodisperse particles, we assume that physical interactions between the particles dominate over hydrodynamic interactions at such

## 2. FLUCTUATING FINITE ELEMENT ANALYSIS (FFEA)

---

high volume fractions.

The thermal noise,  $N_p$ , is chosen such that [Equation 2.12](#) satisfies the fluctuation-dissipation theorem: viscous dissipation must be associated with a stochastic thermal noise as they arise from the same processes. This requires that the statistics of  $\underline{N}^{int}$  from internal deformation be related to the form of  $\underline{\Lambda}$ .

With time step,  $\Delta t$ , components of  $\underline{N}$  therefore have the form:

$$\langle N_i^{int} N_j^{int} \rangle = \frac{k_B T}{\Delta t} (\Lambda_{ij} + \Lambda_{ji}), \quad (2.16)$$

This requires forming the square-root of the viscosity matrix ([Öttinger, 1996](#)), which is normally computationally expensive to calculate. However in the FFEA formulation the viscous stress is constant over each element, and contributions come only from the elements of which the specific node is a part. This gives us delta-correlation of internal thermal noise in both time and space, and allows us to assemble  $N$  on an element-by-element basis.

As the velocity gradient is constant within each element, [Oliver \*et al.\* \(2013\)](#) showed that thermal stress in an element of volume  $V$  for simulation timestep  $\Delta t$  is given by

$$\underline{\pi} = \sqrt{\frac{2k_B T}{V \Delta t}} (\underline{X} \sqrt{\underline{\mu}} + X_0 \sqrt{\lambda \underline{I}}) \quad (2.17)$$

where  $X_0$  is an independent stochastic variable and  $\underline{X}$  a symmetric stochastic

## 2.1 Mathematical model of FFEA

---

tensor, satisfying

$$\langle X_{ij} \rangle = \langle X_0 \rangle = 0, \quad (2.18)$$

$$\langle X_0 X_0 \rangle = 1, \quad (2.19)$$

$$\langle X_0 X_{ij} \rangle = 0, \quad (2.20)$$

$$\langle X_{ij} X_{kl} \rangle = \delta_{ik} \delta_{jl} + \delta_{il} \delta_{jk}, \quad (2.21)$$

leading to the internal viscosity contribution to N

$$N_{p(i,\beta)}^{Int} = - \int_{\Omega} \frac{\delta \psi_{\beta}}{\partial x_j} \pi_{ij} dV. \quad (2.22)$$

The dissipation due to the drag against the implicit solvent is given by:

$$N_p^{Ext} = \left( \frac{12k_B T \pi R_{\text{eff}} \mu^s}{\Delta t} \right)^{\frac{1}{2}} X_p^{Ext}, \quad (2.23)$$

where  $\underline{X}^{Ext}$  is an independent stochastic vector with the properties

$$\langle X_p^{Ext} \rangle = 0, \quad (2.24)$$

$$\langle X_p^{Ext} X_p^{Ext} \rangle = \delta_{pq}. \quad (2.25)$$

Having defined the constituent terms, we finally solve [Equation 2.12](#) for  $\underline{v}$  using a preconditioned conjugate gradient technique. We then use  $\underline{v}$  to perform a single forward Euler integration, chosen for simplicity and computational speed, calculating the new positions of each node after timestep  $\Delta t$  as

$$\underline{x}(t + \Delta t) = \underline{x} + \underline{v} \Delta t. \quad (2.26)$$

## 2. FLUCTUATING FINITE ELEMENT ANALYSIS (FFEA)

---

Mechanical accuracy is acceptable, as covered by [Solernou \*et al.\* \(2018\)](#).

### 2.2 Colloid interactions

We utilise an overlap potential energy term to represent steric repulsion between different objects. Overlapping elements gain an unfavourable positive energy proportional to their intersecting volume, giving rise to a conservative force.

The repulsive force between two surface elements is calculated as

$$\underline{F}_{steric} = -\underline{\nabla}kV, \quad (2.27)$$

where  $V$  is the overlapping volume of the tetrahedra, and  $k$  is a prefactor that governs the strength of the response to overlap. This has units of modulus, but does not represent a modulus of the physical system simulated, but rather a resistance to overlap. This modulus should be chosen to be larger than that of the bulk modulus of the particle to prevent overlap.

When two elements overlap, the repulsive force is applied in equal and opposite directions to each of the two elements. The point of application of the force is chosen to be the centre of mass of the overlap volume. This force is then transferred to the element nodes by linear interpolation. Choosing the point of action of the steric force in this way also avoids introducing an unphysical torque into the collision.

If all external surfaces in a simulation were tested for interactions with all other faces, computational expense would scale as the square of the number of faces. To reduce this computational expense, we split the computational volume into cubic

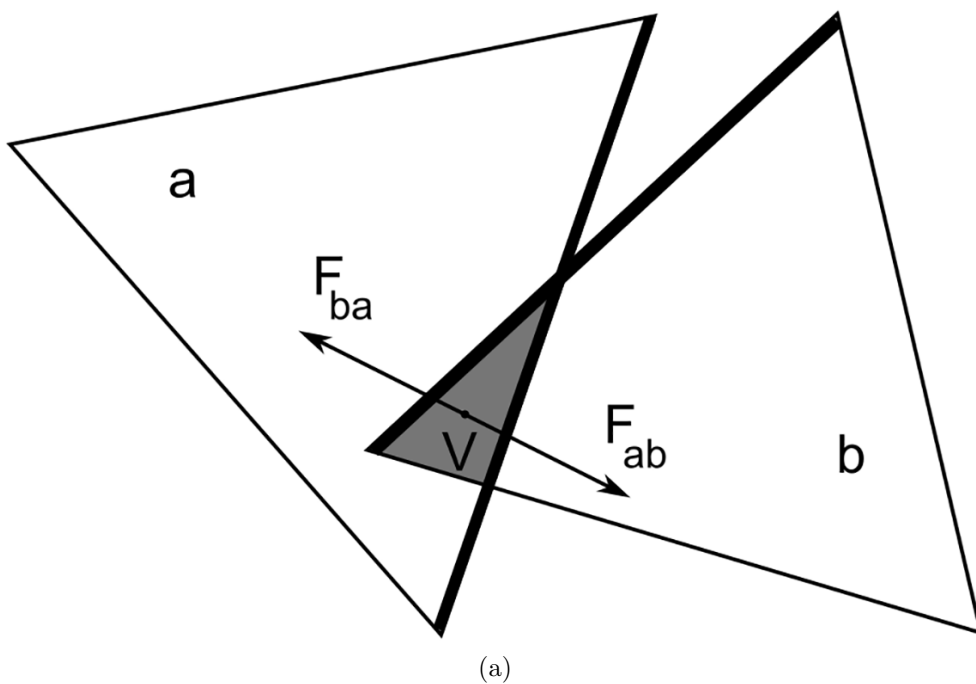


Figure 2.1: 2D illustration of FFEA steric repulsion with 3D tetrahedra reduced to triangles  $a$  and  $b$ .  $V$  is the volume overlap and  $F_{ba}$  is the force applied on tetrahedron  $a$  by the overlap with tetrahedron  $b$ .  $F_{ab} = -F_{ba}$  is the Force applied to tetrahedron  $b$ . This force is linearly interpolated over all nodes of the tetrahedron (Solernou *et al.*, 2018).

## 2. FLUCTUATING FINITE ELEMENT ANALYSIS (FFEA)

---

cells, or voxels. The external surfaces are then assigned to a voxel based on the position of their centre of mass within the grid. Interactions are only considered between surfaces in the same voxel or the 26 surrounding voxels. The lengths of these cubic voxels are chosen based on the dimension of the particles considered. The length is required to be longer than the longest edge of an element in these particles, so an element will consider all other elements it could possibly interact with.

Finally, external surfaces only interact if the dot product of their normals is zero or negative, i.e. if they are facing each other, both as a rapid numerical check to avoid unnecessary calculations, and also to avoid transmitting interactions inside the object's interior.

FFEA is also capable of including longer range interactions such as Lennard-Jones, but these were not utilised for our systems due to computational cost: the longer range the force, the more interactions have to be considered, and considering interactions already makes up 85-90% of compute time for our systems.

### 2.3 Summary

In this chapter, we have discussed the underlying mathematical model of FFEA. We have also introduced the treatment of colloids and microgels as continuum soft objects with a viscoelastic response to deformation, due both to thermal-induced deformation and to deformation due to interaction. We have introduced the surface interactions included in our simulations.

With the trajectories of each node, we have the volumetric deformation of each element. This is the key difference between this approach and the majority

of other approaches for simulating packed colloidal systems: while most others use radially symmetric potentials, we can capture reactions to compression and to anisotropic deformation with our continuum approach. While the elastic stress acts to return the object to its equilibrium configuration, the thermal stress acts to continuously deform it. This interplay allows cooperative deformations to result in rearrangement, as will be seen in [Chapter 4](#). The elastic response corresponds to both the osmotic pressure due to swelling and deswelling, as well as the elasticity of the polymer network itself.

FFEA also includes standard mechanical validation that can be run upon compilation of the software. The most relevant of these verify that the steric forces in this chapter are effective in preventing overlap of simulated bodies, and additionally verify that the simulation produces the expected result for a freely diffusing coarse-grained sphere.

However, as this software was designed for simulation of biological macromolecules, a number of modifications were required to render it suitable for simulating a bulk of soft colloids and recover rheological properties. These modifications, and the basics of constructing a soft colloidal simulation in FFEA, are discussed in the following chapter.

## **2. FLUCTUATING FINITE ELEMENT ANALYSIS (FFEA)**

# Chapter 3

## Simulations of Soft Colloids using FFEA

In this chapter we describe the method used to simulate the dynamics of an ensemble of soft colloids. The experimental system that initially inspired our simulations is soft-colloidal microgels. These are typically comprised of small particles (100-1000 nm) made from cross-linked polymer chains. These particles are highly compressible and deformable as they are swollen by solvent, salt, surfactant or a combination thereof. The solvent mixture inhabits the voids between polymer strands, and this can be expelled and reabsorbed to swell and deswell the microgel. This will result in both elastic responses to compression and deformation due to the polymer structure and interactions, but also an internal viscosity from the relative movement of the solvent through the polymer network. Because of this structure and size (sub-micron to micron) they can therefore be compressed and deformed significantly under typical force of order nanoNewtons per particle. Our choice of system is guided by the size range of real microgels and ensuring

### 3. SIMULATIONS OF SOFT COLLOIDS USING FFEA

---

efficiency of computation with regard to timestep length. Moreover, these systems are sufficiently small and flexible that thermal noise plays a significant role in their dynamics.

We wish to study the dynamics of rearrangement of soft colloidal particles where rearrangements of the equivalent hard spheres would be impossible. We also wish to study rheology: the response of such systems to flow. Rearrangement and rheology are both influenced by system structure: studying them requires simulating systems with sufficiently large population that the structure and dynamics are not strongly affected by the system size.

In the following sections we detail the modifications required and implemented to adapt the FFEA code for simulating a collection of soft colloidal particles. We also discuss the assumptions and approximations that define our parameter space. We consider how we define and generate a single particle in isolation. We then discuss requirements for a simulation of a finite number of particles to be representative of bulk material, including modification and use of Periodic Boundary Conditions (PBCs) for a quiescent bulk material and the addition of Lees-Edwards Boundary Conditions (LEBCs) for sheared bulk material. We explain the method of generation of initial configurations for the simulations. We discuss the requirement for and implementation of an efficient multi- $\tau$  correlator to extract statistical measures of particle diffusion and stress. To conclude, we discuss practical considerations of using FFEA to simulate these systems. This includes a discussion of simulation performance, including parallelisation, performance bottlenecks, and finally limitations of this simulation approach.

### 3.1 Building a soft colloidal simulation

To simulate systems from which we can extract rearrangement dynamics and rheological information, we must attempt to approximate a macroscopic bulk material using a finite simulation with a limited number of particles. We first define a simulation box as a box with side lengths  $L_x$ ,  $L_y$ ,  $L_z$ , within which  $N$  colloidal particles, with properties discussed in [subsection 3.1.1](#), will be placed.

To best approximate a quiescent bulk material through simulation, we must introduce Periodic Boundary conditions (PBCs) on all three axes, where the simulation box interacts with periodically repeated images of itself. To approximate a sheared bulk material, we must also introduce Lees-Edwards Boundary conditions (LEBCs), where the periodic images in the gradient direction are offset in the flow direction.

#### 3.1.1 Construction of a single colloidal particle

To begin, we must define our computational representation of a soft colloid. We do this by first defining a tetrahedral finite element mesh by coarse graining a sphere. Representation of approximately spherical particles with a tetrahedral finite element mesh is a compromise between accurately representing a sphere using more elements, and the computational efficiency of using fewer elements. Additionally, thermal fluctuations of small elements can cause significant element distortion and therefore computational instability, requiring shorter timesteps to keep stable. However, there are also issues with using too coarse a representation. Icosahedral meshes were trialled, but these were deemed too simplistic, as their regularity and ability to tessellate could bias results. Faceting can be important

### 3. SIMULATIONS OF SOFT COLLOIDS USING FFEA

---

for packed soft systems, and the more simplistic mesh one uses, the more inherent faceting that is introduced to the colloids due to the lower number of tetrahedra they contain.

The mesh for our particle was generated using the software package Netgen (Schöberl, 1997), using the ‘Very Coarse’ setting from a sphere. All simulated colloids are identical, being initialised with the same input files. All the results in this thesis were generated using particles composed of a mesh of 44 tetrahedral elements with a single internal node that all elements share.

The particles have an equilibrium diameter of approximately  $10^{-7}\text{m}$ , with an actual volume of  $4.07 \times 10^{-22}\text{m}^3$  after coarse-graining. All simulations presented use monodisperse particles. This size is relatively small for a microgel but within a realistic range. We limit the size to remain in a regime where thermal fluctuations might be most relevant. Bulk moduli are varied between 2-12kPa, held at a constant Poisson ratio of 0.33 as measured by Voudouris *et al.* (2013) at 302.15K for pNIPAM microgels. This corresponds to a range of 0.6-3.7kPa for shear moduli. These moduli were chosen to be within a reasonable range for Poly(N-isopropylacrylamide) (pNIPAM) microgels, as measured by Aufderhorst-Roberts *et al.* (2018), from a range of 3-50kPa. Our simulational range was chosen to allow for a longer timestep, as the higher the modulus, the less stable the simulation will be. Water viscosities for the simulated colloids were sourced from the work of Holmes *et al.* (2011); a shear viscosity of  $8.8 \times 10^{-4}\text{Pa}\cdot\text{s}$  and a bulk viscosity of  $2.47 \times 10^{-3}\text{Pa}\cdot\text{s}$ , and the Stokes viscosity for the implicit background solvent was set to  $1.00 \times 10^{-3}\text{Pa}\cdot\text{s}$ .

#### Damping

As discussed in [Chapter 2](#), we expect that this system is overdamped and that we can use the version of the FFEA solver that takes advantage of this fact. In this subsection, we verify that these approximations are appropriate for the parameter space we explore. As shown by [Hanson \(2018\)](#), we can check this by evaluating the ratio  $\frac{\tau_m}{\tau_K}$ , where  $\tau_m$  and  $\tau_K$  are the time constants associated with the inertial and elastic relaxation respectively. If we assume a homogeneous object, we can approximate  $\tau_M$  as

$$\tau_M \sim \frac{\rho}{\mu}, \quad (3.1)$$

and  $\tau_K$  as

$$\tau_K \sim \frac{\mu}{K}. \quad (3.2)$$

Here  $\rho$ ,  $\mu$  and  $K$  are the density, viscosity and bulk modulus of the object, respectively. The system is overdamped if  $4\frac{\tau_M}{\tau_K} < 1$ , so the inertial relaxation time is faster than the viscoelastic relaxation, meaning that the inertial forces decay quickly and the longer time motion is a balance of viscous and elastic forces.

[Hanson \(2018\)](#) further shows that for a globular or spherical body,

$$4\frac{\tau_M}{\tau_K} \approx \frac{16}{9} \frac{\rho K}{\mu^2} \quad (3.3)$$

and for the range of values outlined above, this evaluates to:

$$8.89 \times 10^{-5} \leq 4\frac{\tau_M}{\tau_K} \leq 5.33 \times 10^{-4} \quad (3.4)$$

### 3. SIMULATIONS OF SOFT COLLOIDS USING FFEA

---

and we therefore remain comfortably in the overdamped regime for all discussed simulations.

#### Deformability of colloids

It is worth also quickly calculating a measure that would indicate how likely our colloids are to deform under thermal motion, to check whether we are in a regime where the unique capabilities of FFEA would be relevant. To do this we calculate an approximate strain  $\gamma$ :

$$\gamma = \sqrt{\frac{k_B T}{G_P V_P}}, \quad (3.5)$$

where  $G_P$  is the shear modulus of the particle and  $V_P$  is the volume per particle.

This gives strains between

$$0.04 \leq \gamma \leq 0.13. \quad (3.6)$$

Meaning that quite substantial shape changes are possible with only thermal motion.

#### 3.1.2 Periodic Boundary Conditions

Implementation of periodic boundaries required two separate modifications to the FFEA code: particles must be returned appropriately to the simulation box when they exit, and we must include the periodic interactions of colloids across the box boundaries.

We first consider returning particles to the simulation box. This requires any colloid whose centre of mass exits the simulation boundaries to be moved by the box length,  $L_{Dim}$ , in the appropriate dimension to return it to the opposite side of the simulation box.

### 3.1 Building a soft colloidal simulation

---

Second, we must account for interactions across a box boundary where the centre of mass of a particle remains inside the simulation box, but part of the colloid protrudes outside of the simulation box. To deal with this consistently, we must consider interactions between the colloids across the simulation box boundaries in each dimension. As discussed in [Chapter 2](#), the simulation box is decomposed into cubic voxels. The simulation box decomposition then creates a list of elements whose centre of mass is in each voxel. The list considers interactions of external surfaces of a colloid in a voxel with the 26 surrounding voxels, accounting for a box boundary by adding or subtracting the total number of voxels in that dimension,  $N_{Dim}$ , as appropriate. Elements in this list are then checked for overlap, with each possible collision being considered once. A visual reference for this implementation can be found in [Figure 3.1](#)

To check for collisions between pairs of colloidal particles, an array of 'corrections' to the centre of mass displacement for all colloid pairs is constructed such that they can be projected appropriately, using the following equation in each dimension:

$$C_x = L_x \left\lfloor \frac{x_\beta - x_\alpha + \frac{L_x}{2}}{L_x} \right\rfloor \quad (3.7)$$

where  $x_\alpha$  and  $x_\beta$  are the centre of mass  $x$ -coordinates of the two colloids,  $C_x$  is the stored correction between a pair of colloids  $\alpha$  and  $\beta$  for the  $x$ -direction, and  $L_x$  is the box length in the  $x$ -direction. In the above equation, the bracket notation  $\lfloor \rfloor$  denotes the greatest integer less than the enclosed quantity. Calculation of corrections for  $y$ - and  $z$ -directions proceeds similarly.

Any distance between colloids greater than half a box length apart in any dimension will then result in a correction such that the projected position will

### 3. SIMULATIONS OF SOFT COLLOIDS USING FFEA

---

always be within  $\frac{L_{Dim}}{2}$  in that dimension, thus finding the closest projected image to be used for calculation of interaction forces. This correction is calculated once per frame for all particle pairs.

This PBC implementation was tested and found to be functioning correctly by verifying identical incidence of surface contact and energy of overlap for equivalent simulations between pairs of colloids across the simulation box boundaries.

This is illustrated in [Figure 3.1](#) in which a collision between two particles at the centre of a box, or an identical collision across the periodic boundary, gives the same results.

### 3.1 Building a soft colloidal simulation

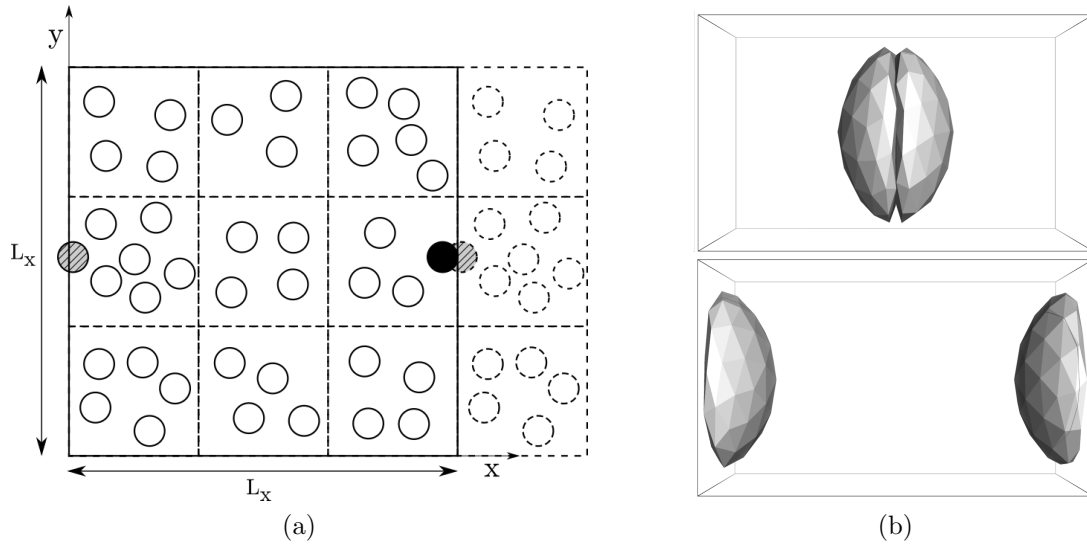


Figure 3.1: (a) 2-dimensional cartoon of PBCs. Straight dotted lines denote voxels while straight solid lines denote simulation box boundaries. Solid particle lines denote position of particle in simulation. Dotted particle lines indicate projected image of particle through PBCs. The particle filled in solid black considers interactions with particles in surrounding voxels, finding particles to consider interactions in all voxels from the opposite edge. All projected images of particles from these voxels are checked for collision, and only the gray, hatched particle is found to overlap. The black particle and the hatched grey particle experience a corrective steric force due to this overlap. (b) Illustrative visualisation of identical collisions simulated in FFEA using corrected PBCs in the centre of the simulation box and at the edge.

### 3. SIMULATIONS OF SOFT COLLOIDS USING FFEA

---

#### 3.1.3 Lees-Edwards Boundary Conditions and external forcing due to shear

To simulate bulk conditions in shear flow, we use Lees-Edwards Boundary Conditions (LEBCs). These modify PBCs by having the projected images of the system in the gradient direction move in the flow direction relative to the simulation box. In all sheared systems we have simulated, the gradient is in the  $y$ -direction, flow is in the  $x$  direction and vorticity in the  $z$ .

For the projected image in the positive  $y$ -direction, the offset distance  $O_{box}$  in the  $x$  direction is

$$O_{box} = \gamma L_y - n L_y \quad (3.8)$$

where  $n \in \mathbb{Z}$  such that  $0 < O_{box} < L_y$ . This is to ensure that an image adequately close to the simulation box is always selected.  $\gamma$  is calculated as

$$\gamma = \dot{\gamma} t \quad (3.9)$$

and strain rate  $\dot{\gamma}$  is supplied as a constant scalar. The image in the negative  $y$ -direction is offset by  $-O_{box}$ .

If a colloid's centre of mass exits the simulation box in the  $y$ - direction, it is moved back into the simulation box in the  $y$ -direction by  $L_y$ , and its  $x$ -coordinate offset by  $O_{box}$ , to account for the relative motion of the projected image.

The voxels considered for interactions must also be altered to account for this offset. This correction is calculated as

$$O_{cell} = \left\lfloor \frac{O_{box}}{r_c} + \frac{1}{2} \right\rfloor \quad (3.10)$$

### 3.1 Building a soft colloidal simulation

---

where  $r_c$  is the length of each side of a voxel.  $O_{cell}$  is an integer that adjusts which voxels are considered for collision, shifting to voxels corresponding to  $O_{box}$  in the  $x$ -direction. The  $\frac{1}{2}$  ensures that particles whose centre of mass is near the edge of a voxel are consistently dealt with and are mapped to an appropriate voxel for comparison with the surrounding voxels.

LEBCs also require a slightly modified set of calculations for the corrections to interactions across the box boundary. For the  $y$  and  $z$  directions, these remain the same as in [subsection 3.1.2](#), but for the  $x$ -direction the shortest particle separation becomes

$$C_x = L_x \left[ \frac{x_\beta - x_\alpha + \frac{L_x}{2} - O_{box} \frac{C_y}{L_y}}{L_x} \right] + \frac{O_{box} C_y}{L_y}. \quad (3.11)$$

This is similar to the correction discussed in [Equation 3.7](#), with additional corrections of  $\frac{O_{box} C_y}{L_x}$ , to account for the relative  $x$ -displacement of images in the  $y$ -direction. A visualisation of LEBCs can be seen in [Figure 3.2](#).

In addition to the modification of boundary conditions, the drag force on the colloids is also modified to account for the implied background shear flow of solvent. This gives an additional force on each node of

$$F_x = \dot{\gamma} L_y d_S \left( \frac{y_{node}}{L_y} - \frac{1}{2} \right), \quad (3.12)$$

where  $F_x$  is the  $x$ -component of the drag force,  $y_{node}$  is the  $y$  position of the node, and  $d_S$  is the Stokes drag scaling on the node. This gives zero force on the central plane of the box, and a linear velocity gradient in the  $y$ -direction.

This implementation of LEBC and velocity gradient in the background solvent was tested and found to be functioning correctly by verifying identical incidence of surface contact and energy of overlap for equivalent simulations in both the

### 3. SIMULATIONS OF SOFT COLLOIDS USING FFEA

---

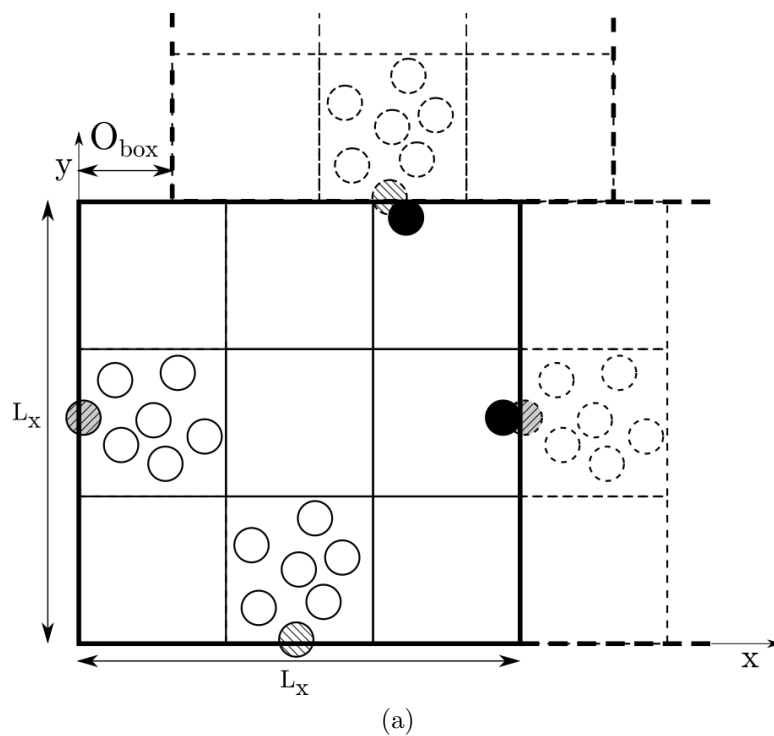


Figure 3.2: Cartoon of LEBCs. Thick lines denote the boundary of the simulation box and thin lines denote the edge of voxels. The solid black particle on the edge of the box in the  $x$ -direction interacts with the grey hatched particle as it would in standard PBCs. The black particle on the edge of the box in the  $y$ -direction interacts with the image of the white hatched particle, with the image offset by  $O_{box}$  in the  $x$ -direction due to the implementation of LEBCs.

## 3.2 Initialisation of a simulation

---

centre of the box and edges in the  $y$  direction. This is visualised in [Figure 3.3](#).

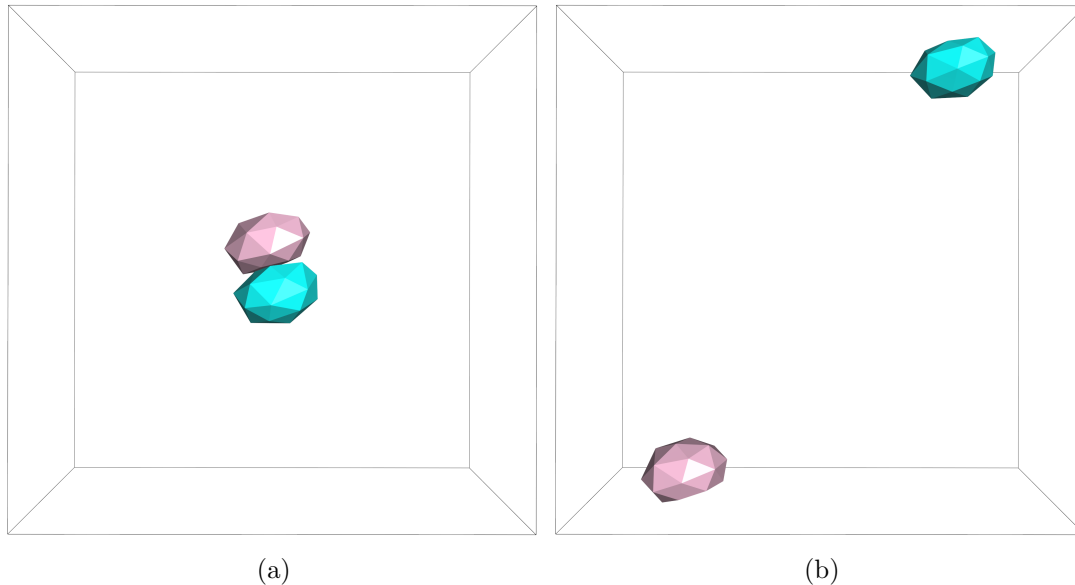


Figure 3.3: Identical collisions between two colloids in a shear gradient in the (a) middle and (b) edge of the simulation box, illustrating the offset due to LEBCs.

## 3.2 Initialisation of a simulation

Having defined the simulation box and the relevant boundary conditions for simulating a bulk material, we now describe the initialisation of our system. This includes three major considerations - the compressed state of our system, placement of the particles, and an initialisation step of the simulation to allow the system to relax approximately to equilibrium.

Firstly, we need to equilibrate our systems in a compressed state. We considered two possible approaches for this - one where the system starts in an uncompressed state, and the simulation box volume is slowly reduced until the particles

### 3. SIMULATIONS OF SOFT COLLOIDS USING FFEA

---

are in contact, and a second where the particles themselves begin in a compressed state and are allowed to expand into contact. The latter scheme was used, as it was the easiest to implement, and the schemes are otherwise equivalent.

Our initialisation strategy is aimed at achieving as random a distribution of particles as possible. To this end, initial placement of particles is decided through the use of code generously shared by Dr. Mike Evans, which generates a random placement of hard spheres at 50% volume fraction. The algorithm proceeds by starting with randomly placed particles of small radius and then progressively increases particle radius until the target volume fraction is met. During this process particles are moved via random Monte-Carlo moves subject to a hard core potential (preventing overlap) plus a weaker interparticle potential to minimise move rejection. Once this algorithm has generated an acceptable distribution, it saves the coordinates to a file. A python script then takes these coordinates and creates an FFEA input file with each particle compressed to the size of the hard sphere and placed with its centroid at each of the coordinates. Once particles are placed in this manner, FFEA is run in an initialisation step so that particles decompress and come into contact with each other.

Inter-particle forces are calculated using the steric interaction detailed in [section 2.2](#), with steric factors generally varied proportionally to  $K$ , and additionally varied to ensure simulation stability. These values are detailed in [Table 4.1](#). Simulations output the full trajectory every 10000 frames (or  $10^{-5}$ s). We assume we require significantly longer than the time for a free particle to diffuse its own diameter (approximately  $10^{-4}$ s, given the above parameterisation) to see cage-breaking events occur.

Timestep for all simulations was chosen as  $10^{-9}$ s and systems are run for

$9.5 \times 10^6$  steps or  $9.5 \times 10^{-3}$ s. This timestep was stable for the colloids with highest modulus, and is kept constant as time constraints made it infeasible to analyse the stable timestep for each softness of particle.

Once the particles are placed, FFEA is run so that the particles decompress and come into contact with each other. The initialisation step is run for  $5 \times 10^5$  steps, equivalent to  $5 \times 10^{-4}$ s. Tests indicate  $2 \times 10^5$  steps, or  $2 \times 10^{-4}$ s are the longest needed for decompression of free particles with the range of moduli we simulate, so we leave enough time for decompression and some initial relaxation.

### 3.3 Stress calculation

To calculate macrorheological properties, we must calculate both the average values of viscous and elastic stresses. These stresses are derived from [Equation 2.3](#) for the elastic stress and from [Equation 2.5](#) for the viscous stress.

Whilst simulating the system dynamics, we construct [Equation 2.3](#) in the course of the internal elastic stress calculation within each element, and so we can simply sum the contribution from all elements of all objects in the simulation, and then normalise by the volume of the simulation box to retrieve the elastic stress for the bulk material.

By contrast, [Equation 2.5](#) is not calculated directly as part of the simulation, so we add an explicit calculation, and store a normalised version as with the elastic stress.

For quiescent simulations, we use these quantities to calculate a stress auto-correlation function, which is discussed in [section 3.4](#). For sheared simulations, we extract the mean of  $\sigma_{xy}^e$  to construct a flowcurve.

## 3.4 Multi- $\tau$ correlator

### 3.4.1 General background

Consider a dynamically stochastic system in which some function of the system state  $f(t)$  fluctuates around some equilibrium mean value  $\langle f \rangle$ . Instantaneous fluctuations away from the mean are expected to relax back towards the mean on sufficiently long timescales, to be replaced by new fluctuations. One can recover dynamical effects such as the average time for a fluctuation to decay by considering the autocorrelation of the instantaneous value of  $\Delta f(t) = f(t) - \langle f \rangle$  at different times:  $\langle \Delta f(t) \Delta f(0) \rangle$ , where  $\langle \rangle$  represents a time average over all possible origins of the time axis, or an ensemble average over many equilibrium realisations of the same system. If the system is ergodic, these two averages are equivalent. We also assume the form of system dynamics to be time invariant. This allows us to consider any single trajectory as multiple trajectories of a shorter length, which we may use to improve our statistical error for shorter correlation times.

Such time autocorrelation functions can be used to reveal relaxation properties of systems. We use them to determine the the Mean-Square Displacement (MSD) of particles to deduce the statistics of particle motion including the occurrence and timescales of caging effects and cage-breaking, and the deviatoric stress autocorrelation function, allowing us to deduce the timescales of stress relaxation in quiescent systems. This latter function will also aid in ascertaining whether quiescent systems have entirely relaxed to their equilibrium state. Stress autocorrelation and MSD behave slightly differently, and so will need to be discussed separately. The deviatoric stress relaxes to a fixed equilibrium value, in this case

zero, and so calculating the correlation function for this quantity is easier and is discussed in [subsection 3.4.2](#). For quantities such as the MSD of the system, which is an increasing function of time, we must introduce a correction to the correlation function discussed in [subsection 3.4.4](#).

Methods of calculating a time autocorrelation function can often consume significant computational and memory resources, especially in simulations such as ours, which span 7 decades in time between an individual timestep and the total time of the simulation. To overcome this we have implemented a memory and computationally efficient correlator, that was proposed by [Ramírez \*et al.\* \(2010\)](#). This algorithm uses hierarchical averaging in time to obtain correlation at different timescales in a way that is computationally and memory efficient. It is based on a well known multiple- $\tau$  correlator method used in dynamic light scattering experiments ([Magatti & Ferri, 2001](#); [Schtzel \*et al.\*, 1988](#)). Information is added to correlators every 100 timesteps (or  $10^{-7}$ s, for our choice of timestep), to avoid undue computational cost from calculating values to be fed to the correlator.

#### 3.4.2 Theory and implementation

The time autocorrelation of a dynamical function  $f(t)$  obtained from a simulation may be expressed as

$$F(\tau) = \frac{1}{T - \tau} \int_0^{T-\tau} f(t + \tau)f(t)dt, \quad (3.13)$$

### 3. SIMULATIONS OF SOFT COLLOIDS USING FFEA

---

where  $T$  is the duration of the simulation trajectory, and  $\tau$  the lag time. Where a simulation has  $N - 1$  discrete steps of length  $\Delta t$ , this is approximated as:

$$F_j = \frac{1}{N-j} \sum_{i=0}^{N-j-1} f_i f_{i+j}, \quad (3.14)$$

where  $F_j \equiv F(j\Delta t)$  and  $f_i \equiv f(i\Delta t)$ .

For large systems, with a large number of timesteps, evaluating Equation 3.14 can require processing a huge amount of data. Following Ramírez *et al.* (2010), we consider averaging the function  $f$  over  $k$  neighbouring points,

$$\bar{f}_{i,k} = \frac{1}{k} \sum_{j=0}^{k-1} f_{i+j}, \quad (3.15)$$

and define a correlator of these averages as

$$\bar{F}_{j,k} = \frac{1}{N-j-k+1} \sum_{i=0}^{N-j-k} \bar{f}_{i,k} \bar{f}_{i+j,k} \quad (3.16)$$

$$= \frac{1}{k^2(N-j-k+1)} \sum_{i=0}^{N-j-k} \sum_{q=0}^{k-1} \sum_{s=0}^{k-1} f_{i+q} f_{i+j+s}. \quad (3.17)$$

In the limit where  $N \gg j$ , small differences in the upper limits can be neglected and we obtain

$$\bar{F}_{j,k} \approx \frac{1}{k^2} \sum_{q=0}^{k-1} \sum_{s=0}^{k-1} F_{j+s-q} \quad (3.18)$$

$$= \frac{1}{k^2} \sum_{q=-k+1}^{k-1} (k - |q|) F_{j+q}, \quad (3.19)$$

which is equivalent to applying a triangular smoothing to the correlation function.

Such smoothing is likely to be acceptable for  $j \gg k$ .

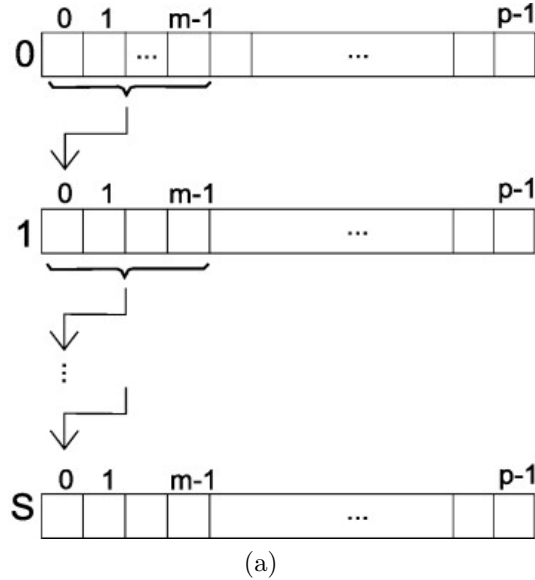


Figure 3.4: Schematic view of the data structure implemented in the multi- $\tau$  correlator. We represent each level of storage, with the arrow representing the averaging and transferring between different levels of the correlator. Schematic used from [Ramírez \*et al.\* \(2010\)](#).

In practice, the pre-averaging and storage of the values the correlation function will be calculated with is implemented through a layered data structure, shown schematically in [Figure 3.4](#), which introduces greater levels of smoothing as the correlation time increases, i.e.  $k$  increases as  $j$  increases. New values of the function  $f$  are introduced at the zeroth layer and short time correlations are calculated within this layer, without any averaging. As values are introduced to this layer older values are pushed along the zeroth layer, while also being placed into a buffer of a user-defined size  $m$ . When  $m$  values are stored in the buffer, these are averaged and this single averaged value is pushed to the layer below, i.e. the first layer. Therefore,  $k = m^n$  where  $n$  is the number of the layer, as we

### 3. SIMULATIONS OF SOFT COLLOIDS USING FFEA

---

have multiple resolutions of data, and the layers average more and more points as  $n$  grows. As these new, average values are added to layer 1, time correlations of these average values are calculated within that layer. This process of storing  $m$  values in a buffer, averaging them, and then sending the averaged value to the next layer proceeds in a hierarchical manner: so, averaged values from layer 1 are sent to layer 2, and so on. Time autocorrelation functions of the averaged values are calculated within each layer. Any given layer stores only the  $\frac{p}{2}$  most recent values added to it, other than the zeroth layer which stores  $p$  values. Entries are discarded at the end of the level as new entries are recorded. This information will already be part of the layer below. The values of  $p$  and  $m$  are chosen to be 16 and 2, respectively, which correspond to the default values suggested by [Ramírez \*et al.\* \(2010\)](#). A large value of  $p$  compared to  $m$  will reduce error. Increasing  $p$  will increase the amount of data stored at any given resolution, which will improve accuracy at that resolution, but will also increase memory requirements and the number of operations to add to and evaluate the correlator.

The correlators used for the deviatoric stress calculation were tested using a simple 1-dimensional simulation of a particle diffusing in a potential well, with a Langevin equation of

$$\frac{dx}{dt} = -\frac{k}{\zeta}x + \frac{f}{\zeta}. \quad (3.20)$$

Here,  $x$  is position,  $t$  is time,  $k$  is the strength of the potential,  $\zeta$  is the frictional drag, and  $f$  is the noise term.  $F(t)$  obeys statistics  $\langle f(t)f(t') \rangle = 2k_B T \zeta \delta(t - t')$ . These dynamics discretise to:

$$\Delta x = -\frac{k}{\zeta}x\Delta t + \frac{f}{\zeta}\Delta t \quad (3.21)$$

where  $f$  is evaluated at each time from

$$f_i = \sqrt{\frac{24\zeta k_B T}{\Delta t}} r_i \quad (3.22)$$

where  $r_i$  is a random number from a uniform distribution over -0.5 to 0.5. In units where  $k, \zeta, k_B T$  are all equal to 1, the autocorrelation is expected to be  $\langle x(s)x(s+t) \rangle = e^{-t}$ . We simulate this with timestep  $\Delta t = 0.005$  over  $10^9$  steps.

Figure 3.5 shows that the computed autocorrelation is as expected.

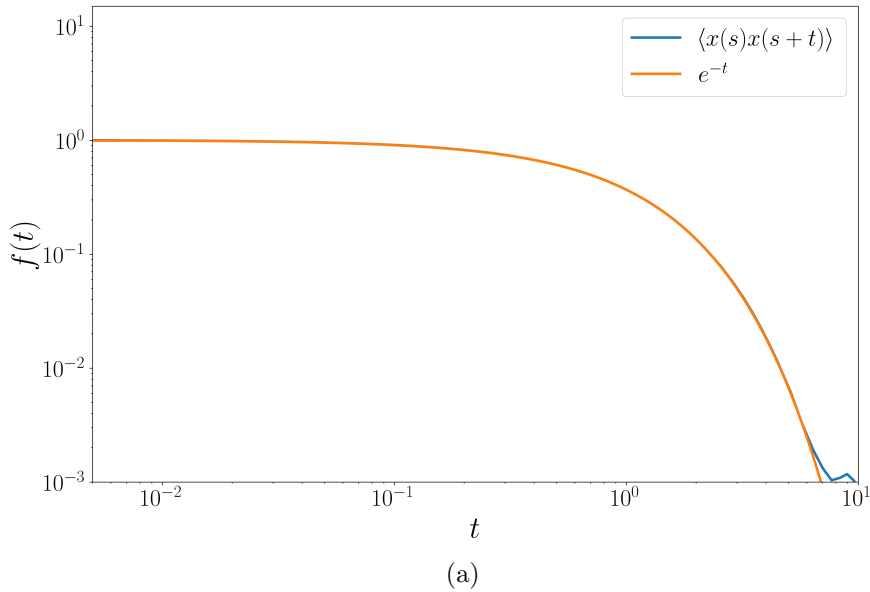


Figure 3.5: Verification of the correlator for a particle diffusing in a potential well. Correlator output matches  $e^{-t}$  until its value is low enough that noise begins to cause deviation from the analytic result.

### 3. SIMULATIONS OF SOFT COLLOIDS USING FFEA

---

#### 3.4.3 Stress autocorrelation

The correlation function for stress fluctuations in a finite system is related to the dynamic shear modulus  $G(t)$  via the fluctuation-dissipation theorem. For our soft colloidal system stress relaxation will involve a convolution of both the timescale for relaxation of each individual colloid, and also a timescale for relaxation of the entire suspension. Although  $G(t)$  can be obtained from individual stress components, the statistical sampling error can be reduced by averaging over correlation functions for different components of the deviatoric stress, as in [Ramírez \*et al.\* \(2010\)](#):

$$G(t) = \frac{V}{5k_B T} [\langle \sigma_{xy}(t)\sigma_{xy}(0) \rangle + \langle \sigma_{yz}(t)\sigma_{yz}(0) \rangle + \langle \sigma_{zx}(t)\sigma_{zx}(0) \rangle] \\ + \frac{V}{30k_B T} [\langle N_{xy}(t)N_{xy}(0) \rangle + \langle N_{yz}(t)N_{yz}(0) \rangle + \langle N_{xz}(t)N_{xz}(0) \rangle]. \quad (3.23)$$

Here  $\sigma_{\alpha\beta}$  denotes a component of the stress tensor for the system,  $V$  is volume and  $T$  is temperature, and  $N_{\alpha\beta} = \sigma_{\alpha\alpha} - \sigma_{\beta\beta}$  are the normal stress differences. This measure includes all stresses that act to change the shape of the particles, but not the isotropic stress (pressure) that produces changes in volume. The stress of the implicit background solvent is not included in this calculation.

#### 3.4.4 Mean-Square Displacement

For a quantity such as MSD, whose expectation value grows monotonically with time, we must use a modified approach to autocorrelation functions, again as proposed by [Ramírez \*et al.\* \(2010\)](#). For a particle with position  $r(t)$ , average

MSD may be calculated as:

$$g_j = \frac{1}{N-j} \sum_{i=1}^{N-j-1} \langle (r_{i+j} - r_i)^2 \rangle. \quad (3.24)$$

where  $N$  is the number of steps in the simulation,  $j$  is the time lag  $\tau$  in steps of  $\Delta t$ ,  $i$  the initial step being considered and  $r_q$  the position at timestep  $q$ . We may define the time-averaged position of the particle:

$$\bar{r}_{i,k} = \frac{1}{k} \sum_{j=0}^{k-1} r_{i+j}. \quad (3.25)$$

The mean square displacement of the time average is:

$$\bar{g}_{j,k} = \frac{1}{N-j-k+1} \sum_{i=0}^{N-j-k} (\bar{r}_{i+j,k} - \bar{r}_{i,k})^2 \quad (3.26)$$

$$= \frac{1}{k^2(N-j-k+1)} \sum_{p=0}^{k-1} \sum_{q=0}^{k-1} \sum_{i=0}^{N-j-k} (r_{i+j+p} - r_{i+p}) \times (r_{i+j+p} - r_{i+q}), \quad (3.27)$$

In the limit of  $N \gg j$  this can be shown (Ramírez *et al.*, 2010) to give

$$\bar{g}_{j,k} \approx \frac{1}{k^2} \sum_{p=-k+1}^{k-1} (k - |p|) g_{j+p} - \frac{1}{k^2} \sum_{p=-k+1}^{k-1} (k - |p|) g_p. \quad (3.28)$$

The first sum is of the same form as Equation 3.19. The second sum is an additional required correction that depends on the MSD at smaller timescales, arising because MSD is expected to grow continuously in free diffusion.

To calculate the particle position to supply to the MSD correlator, we must make a few corrections to account for periodic boundary conditions. In the case of quiescent systems, to find the ‘true’ position of the particle relative to its starting

### 3. SIMULATIONS OF SOFT COLLOIDS USING FFEA

---

position, we count the number of times a particle crosses each box boundary. Thus the ‘true’ position in the  $x$ -direction is

$$x = x_{sim} + p_x L_x \quad (3.29)$$

where  $x_{sim}$  is the position within the simulation box,  $L_x$  is the length of the simulation box in the  $x$ -direction and  $p_x$  is the integer number of box lengths to correct by -  $p_x$  is increased by 1 each time a particle exits in the positive  $x$ -direction and decreased by 1 if it exits in the negative  $x$ -direction. The  $y$ - and  $z$ -directions proceed similarly.

We are interested in motion of individual particles relative to the reference frame of the material. Due to finite simulation size, the material bulk itself diffuses, so we must correct for the diffusion of the system as a whole. To do this, we calculate the average of [Equation 3.29](#), and subtract this average from each individual particle displacement to obtain the relative motion of the particles to the centre of mass.

For sheared systems, we are still interested in the MSD of individual particles, to assess whether they leave their cage. We make a first order attempt to remove the effects of Taylor dispersion ([Taylor, 1954](#)), by removing advective transport of the particles by the mean shear flow, so as to isolate diffusion due to cage-breaking. This will allow us to more closely observe the effect on cage-breaking due to shear. In this case, for each colloid we store a variable  $X(t)$  which increments by  $\Delta x(t)$  during one timestep, such that:

$$\Delta X(t) = \frac{\Delta t}{N} \sum_{\alpha} \left( \Delta x_{\alpha} - \dot{\gamma} L_y \left( \frac{y_{\alpha}}{L_y} - \frac{1}{2} \right) \right), \quad (3.30)$$

where the  $\alpha$  is the node in the colloid,  $\Delta x_\alpha$  is the motion of each node in the  $x$ -direction during the timestep,  $N$  is the number of nodes in the colloid,  $y_\alpha$  is the  $y$ -position of the node in the simulation box, and  $\dot{\gamma}$  is strain rate. The second term on the right subtracts the flow advection.

The MSD correlator was tested with both long runs with single particles diffusing and over the average of multiple shorter runs, and was tested by verifying agreement with the expected result for free diffusion:  $\langle r^2 \rangle \propto \tau$ .

## 3.5 Practical considerations

Having set up how we build the idealised system, we now discuss the practical issues of running these simulations, including performance and limitations of the implementation.

### 3.5.1 Parallelisation

To run at the maximum system size possible and to reach the longest timescales, we must investigate the way to achieve best parallel performance for FFEA. FFEA uses shared memory parallelisation with OpenMP, so is currently capable of running in parallel on a single node (i.e. a set of processors sharing the same memory), but not across multiple nodes. By default, the FFEA code compiles two binary executables with different parallelisation strategies. One parallelises by sharing the task of solving the dynamics of each simulation object (colloid) amongst the specified number of threads in the environment it is run, i.e each colloids is split across multiple processors. This approach is suited for small numbers of large, complex meshes. This parallelisation scheme, even if used with

### 3. SIMULATIONS OF SOFT COLLOIDS USING FFEA

---

more fine-grained spherical meshes, peaks in performance on a single processor with multiple cores. On a workstation or HPC node with 2 or more processors, thread count and affinity should be localised to a single processor. This scheme is not well suited to our simulations, because our colloid meshes are simple and do not benefit from being split.

The second parallelisation strategy solves the dynamics for the entirety of any given colloid on a single thread, but distributes the colloids across the specified number of threads in the environment it is run. We select this parallelisation scheme for all simulations presented in our main results, since each colloid is made up of a small number of elements, and we wish to run with large numbers of colloids. This parallelisation scheme also scales well over multiple processors in a node, as we will discuss next.

#### Scaling performance

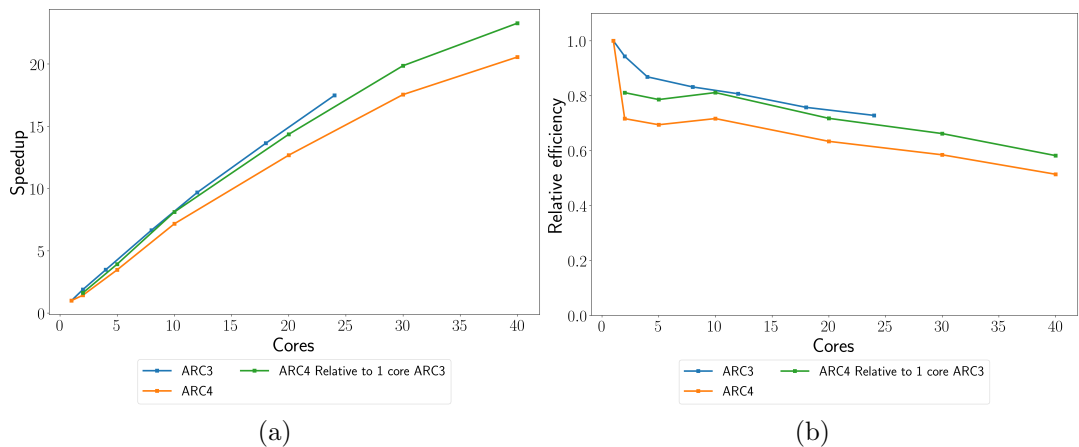


Figure 3.6: (a) Speedup of simulation relative to single core performance of both ARC3 and ARC4. (b) Relative efficiency of each core compared to single core performance.

### 3.5 Practical considerations

---

Simulations included in the main results were performed on the HPC resources at University of Leeds, ARC3 and ARC4, using the standard nodes. Each node on ARC3 contains 2 Broadwell E5-2650v4 processors containing 12 cores, whereas each node on ARC4 has 2 Intel Xeon Gold 6138 processors containing 20 cores. The computational cost per timestep within the multi-colloid parallelisation scheme ideally scales in number of operations somewhere between  $n \log(n)$  and  $n^2$ , due to the voxel decomposition, where  $n$  is number of particles.

To test the efficiency of parallelisation 10,000 steps with the same initial configuration were simulated on ARC3 on 1, 2, 4, 8, 12, 18, and 24 cores and on ARC4 on 1, 2, 5, 10, 20, 30, and 40 cores. The configuration was selected from the last point of a simulation with an effective volume fraction of 0.8 to ensure significant contact and a highly equilibrated system. The simulation is not identical for each trial run, as a different thermal noise was used. However, the computation for a step is quite similar across different configurations of systems with the same input parameters.

As can be seen in [Figure 3.6](#), scaling performance is good, with speedup increasing as more cores are added and relative efficiency per core - defined here as  $\frac{\text{Speedup}}{\text{No. of Cores}}$  - decreasing only moderately. These results clearly demonstrate that it is worthwhile to increase core count. Speedup and relative efficiency are also plotted for ARC4 relative to a single core of ARC3, as ARC4 has a significantly higher single core clock speed(3.7 GHz) than its multi-core clock speed (2.0GHz). We only discuss strong scaling performance here, i.e. scaling for fixed system size with increasing number of processors, as finite size effects dictate a minimum population on the order of 1000 objects regardless.

A trial was also run on ARC3's Xeon Phi Knight's Landing equipped nodes.

### 3. SIMULATIONS OF SOFT COLLOIDS USING FFEA

---

These are x86 manycore processors that share similarities with GPU architecture but still retain x86 compatibility. Unfortunately, this yielded similar performance to the standard compute nodes; it is likely that significant refactoring of the FFEA code would be required to achieve significant performance gains on this architecture. For the purposes of packed colloidal systems such as the ones in this paper, it is likely that implementation of MPI for multi-colloid simulations would yield better results for the effort involved.

#### 3.5.2 Bottlenecks

The performance of FFEA was profiled with allinea, a debugging and performance mapping tool for HPCs, and found that for the systems discussed in this thesis, 85-90% of compute time is spent calculating whether an overlap of elements has occurred, and therefore whether steric forces need to be applied to these elements to push them apart. This is the key bottleneck for these populations of systems in FFEA.

#### 3.5.3 General limitations and further work

While FFEA offers a novel method to approach the simulation of soft colloids, the complexity of the approach does introduce some limitations which we will discuss here.

##### **Finite element approach**

Due to the requirement for computational efficiency, the mesh we use is relatively simplistic, and therefore cannot reflect the denser core and less dense

periphery that is common to the precipitation polymerisation method used to make many common microgels. However, there are methods to make more homogeneously cross-linked polymer microgels, such as those used to make the microgels discussed in [Chapter 5](#). If the code could be further parallelised, simulating meshes of greater internal complexity is a possible future direction for research to proceed. We could also introduce longer range interaction potentials between faces. This would be especially interesting with patchy colloids, where only certain areas of the colloid are attractive.

For systems of different moduli, timestep is limited by the particles with the largest moduli, as the numerics of these particles would require shorter timesteps for stability. The most sensible route, which we again did not have time to implement, would be to explore mixtures of soft and rigid particles. These would not be deformable at all, and therefore do not change the required timestep as there is no oscillation to keep numerically stable. However, modification of the code would be required to implement these rigid particles and allow them to move.

#### **Boundary conditions**

Although we consider only small, spherical colloids in this work, for PBCs care must be taken with definition of box size relative to colloid size and shape. If a colloid is larger than  $\frac{L_{Dim}}{2}$ , or is unusually shaped and therefore has areas significantly distant from its centre of mass relative to box size, the projected image for surface-surface interactions may not be properly located for calculation of all interactions.

For LEBCs, extra care should be taken that the acceptable accuracy of numer-

### 3. SIMULATIONS OF SOFT COLLOIDS USING FFEA

---

ical solutions and the maximum number of solver iterations are set appropriately. Using the default parameters for FFEA, at high strain rates, inaccuracies can be introduced that cause a mismatch of the edge and centre collision cases. If the acceptable accuracy is set too loosely, the high strain rate can introduce differences in force and displacement at the edges of the simulation box. If we then decrease the bounds of acceptable accuracy to counteract this, it may be necessary to increase the number of iterations of the solver that are allowed to reach this higher accuracy. These are slight, but should be validated before use.

#### **Voxel decomposition**

In the simulations detailed in this thesis, voxel lengths vary because a rare issue was found in some simulations, with FFEA failing to apply the correct steric repulsive force to simulated colloids. In such cases, some colloids would entirely and permanently overlap. These simulations were rejected and no data from them is included in this thesis, as they represent an effective removal of a particle from a densely packed simulation.

This can be rectified by increasing the voxel length, but as the the length of each simulation box side results from a multiplication of the number of cells in each direction with the voxel length, these must be varied together to reach the desired volume and therefore the desired  $\zeta_e$ . Increasing the cutoff length comes at a cost to performance, so voxel lengths should take as small a value as possible in balance against this. Appropriate voxel lengths should be calculated by the length of the longest edge in a single element.

### 3.6 Summary

In this chapter, we have discussed how we build a soft colloidal simulations in FFEA. We have described some of the features that have been added to the code, including boundary conditions and the implementation of a runtime multi- $\tau$  correlator. We have discussed how we initialise our systems and the bounds of our parameter space. Finally, we have discussed limitations and important considerations for use of FFEA for soft colloidal simulations. In the next chapter, we will use this knowledge to perform quiescent soft colloidal simulations, and discuss the results.

### **3. SIMULATIONS OF SOFT COLLOIDS USING FFEA**

---

# Chapter 4

## Quiescent Simulations

Having detailed the simulation software and the modifications required for simulation of soft colloidal systems, we now move to analyse and discuss the simulations we have performed. A list of the parameters varied in these simulations can be found in [Table 4.1](#), and the exploration of phase space is illustrated in [Figure 4.1](#). The main aim is to investigate the effects of: particle packing fraction; viscoelastic material parameters; and the ability of particles within the simulations to deform on dynamical observables such as: thermal motion of colloids; particle-particle and structural arrangement; detailed behaviour during cage breaking; structural relaxation; flow. We choose these parameters to vary as in packed monodisperse hard-sphere systems particle packing fraction is the main control parameter ([Hoover & Ree, 1967](#)), so the manner in which volume fraction varies with other measures will be important to understanding how the softness of the colloids changes their dynamics. We compare particle-particle and structural arrangement and whether we the behaviour maps through volume fraction to hard sphere like behaviour. We vary viscoelastic material parameters, as the softness

## 4. QUIESCENT SIMULATIONS

---

of particles has been shown previously to affect on packed dynamics and structure (Mattsson *et al.*, 2009) and indeed change the control parameter of this systems, if a single one exists at all. Particle bulk and shear moduli and viscosities are also parameters that we are uniquely able to vary with FFEA in a physically meaningful way, within bounds originating from direct measurement (Aufderhorst-Roberts *et al.*, 2018; Voudouris *et al.*, 2013). We initially target thermal motion of colloids as it quickly demonstrates meaningful differences from both hard spheres, which would jam at the packing fractions we observe (Hunter & Weeks, 2012) and other simulations of soft spheres, which do not tend to be thermally active as we discussed in section 1.5. We can also uniquely investigate stress due to the ability to carry out simulations of large numbers of truly deformable and compressible three-dimensional colloids as continua.

In this chapter we first compare the true observed volume fraction (after particle decompression) with the effective volume fraction we use to define the parameter space. We also discuss the structural arrangement of particles, calculating representative static structure factors to investigate the extent and distance of correlated structures within the systems. We then discuss the time-dependent Mean-Square Displacement (MSD), discussing what we would expect to see if cage-breaking is occurring on the timescales we can investigate. To underline this point, we present a small number of representative visualisations of particle trajectories with the highest displacement. We then further discuss the indication of cage-breaking through an investigation of the extent to which the distribution of particle displacements is non-Gaussian, both with use of a non-Gaussian parameter and via explicit sampling of the distribution for various time lags. We briefly discuss simple measures of correlations between the asphericity

and velocity of colloids, as an initial means to probe whether particle deformation affects cage-breaking events. Finally, we discuss the stress autocorrelation function, which gives the modulus of relaxation of an instantaneous step-strain for our simulation, and discuss the implications of the results.

## 4.1 Parameter space

The reasons for the choice of parameter space and key research questions are discussed in [Chapter 3](#). We were inspired by the experimental studies of ‘soft’ matter colloidal systems, and seek to investigate the extent to which FFEA can be used to probe their behaviour in a manner that other simulation techniques cannot. Looking at commonly used microgel systems such as pNIPAM ([Aufderhorst-Roberts \*et al.\*, 2018](#); [Bachman \*et al.\*, 2015](#); [Hunter & Weeks, 2012](#); [Sierra-Martin \*et al.\*, 2011](#); [Voudouris \*et al.\*, 2013](#)), we use representative experimental parameter values, shown in detail in [Table 4.1](#), that overlap with the regimes we expect FFEA to be most likely to be relevant to study.

Our exploration of phase space is split into 3 tranches, as illustrated in [Figure 4.1](#): (i) an exploration of  $\zeta_e$  with the bulk modulus,  $K$ , held at 12kPa; (ii) an exploration of  $\zeta_e$  with  $K$  held at 2kPa; (iii) simulations with  $K$  varied from 2kPa to 12kPa, with  $\zeta_e$  held at 0.7. The Poisson ratio is held fixed at 0.33 throughout. These tranches will be referred to in the rest of the chapter by the shorthand [12kPa varied  $\zeta_e$ ], [2kPa varied  $\zeta_e$ ] and [ $\zeta_e = 0.7$ , varied  $K$ ], respectively.

The above ranges were chosen to explore whether there are qualitative differences in these simulations within a physically reasonable parameter space for pNIPAM-based experimental systems, as discussed in [Aufderhorst-Roberts \*et al.\*](#)

## 4. QUIESCENT SIMULATIONS

---

(2018), with the Poisson ratio chosen for pNIPAM microgels near the Lower Critical Solution Temperature from Voudouris *et al.* (2013). Additionally, this range is further constrained by simulation stability and the timescales we can reach, both of which are affected negatively by higher moduli. Thus, we explore the softer end of the relevant modulus space, largely due to these computational considerations.

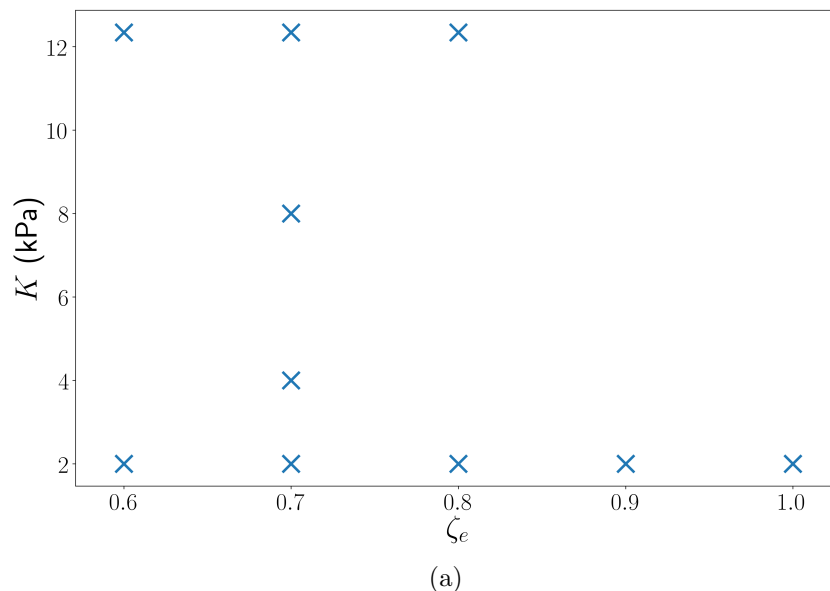


Figure 4.1: Space explored with quiescent simulations.

## 4.2 Repeated simulations and consistency

With the chosen simulation parameters, simulations corresponding to a timescale of  $9.5 \times 10^{-3}$ s were possible within reasonable time, taking up to a month of compute time to simulate. Such simulations would gather good statistics for events occurring on short timescales (e.g  $10^{-7}$ s to  $10^{-3}$ s), but may not adequately

---

## 4.2 Repeated simulations and consistency

sample dynamics for longer times. Additionally, if a simulation does not fully relax from its initial configuration in  $9.5 \times 10^{-3}$ s, that initial configuration may significantly weight the results of that simulation. Hence, we aim for 10 repeat simulations at each set of parameters to probe variation from initial conditions, though for some parameters not all of these simulations were viable, as we will discuss in this section. The population size of these systems was also varied, to see if finite size effects were experienced.

### 4.2.1 Overlapping simulations

While there was an aim to have 10 instances of each simulation, an issue occurred in some simulations where the steric repulsive interactions were not sufficient to prevent significant overlap of colloids. When this occurred, for a pair of colloids, the two particles would overlap almost completely and remain overlapped for the remainder of the simulation with centres of mass within  $10^{-8}$ m of each other. Interactions with surrounding particles prevent escape from the overlapped state. The remedy to this behaviour was to increase the voxel length, which eliminated the issue at a cost of performance.

The 2kPa simulations and nine of ten each of 4kPa and 8kPa simulations did not exhibit this behaviour, and so the original simulations were retained. As can be seen in [Figure 4.2](#) changing the voxel length does result in slightly quantitatively different behaviour for the same material parameters. We utilise only the results from the simulations with larger surface interaction length for the [12kPa varied  $\zeta_e$ ] simulations, but care should be taken when comparing these results with those from the simulations with softer moduli, as they are likely to

## 4. QUIESCENT SIMULATIONS

---

be comparing slightly different dynamics due to the different force calculations. It is interesting to note that capturing more interactions enables faster dynamics.

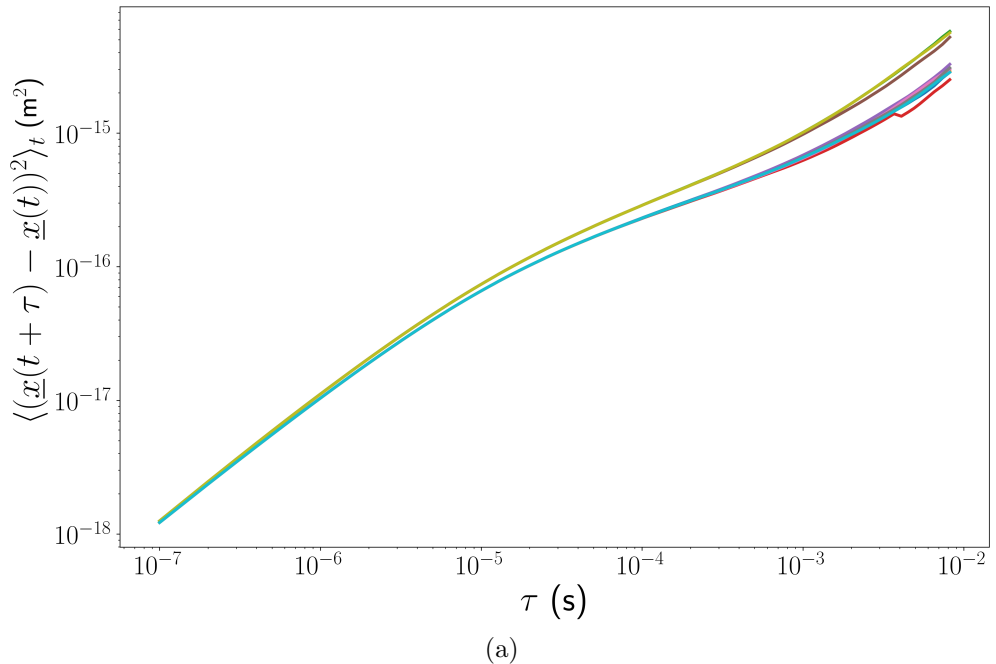


Figure 4.2: Quantitative difference between simulation instances with larger surface interaction cutoff (upper curves) and original interaction cutoff (lower curves) for 12kPa simulations with  $\zeta_e = 0.6$ .

### 4.2.2 Finite size effects and Convergence

In addition to considerations of the resolution of individual colloids, we must also consider the effects of the finite size of the simulation box. To probe this effect, we simulated systems with populations of  $N = 100$  and  $N = 1000$ , attempting to reach longer timescales with fewer colloids and testing what size of simulations we could run on an acceptable timescale. Additionally populations up to  $N = 8000$

## 4.2 Repeated simulations and consistency

---

were trialled, but time and computational resource constraints, as well as the inherent lower stability of larger populations sizes in a system with stochastic dynamics did not allow this to be properly explored. While time and computational resource constraints limited us in this way, works such as Seth *et al.* (2011) do not see observe substantively different dynamics moving from populations of  $10^3$  to populations of  $10^4$ . This suggests populations of  $10^3$  can be sufficient, but we have been unable to ascertain the extent of finite size effects beyond this population size in these simulations, which are thermally active, whereas particles in the work of Seth *et al.* (2011) were not.

In Figure 4.3 we can see that for the less populous simulations we found significant differences within each volume fraction depending on initial configuration; some configurations reach a second diffusive regime, while other simulations plateau indefinitely. This difference in behaviour is evident even in a sample size of ten, and is observed multiple times. With 1000 colloid simulations, behaviour of each set of simulations at a particular effective volume fraction ( $\zeta_e = \frac{NV_0}{V_{box}}$ , where  $N$  is number of particles,  $V_0$  is uncompressed volume of the colloid, and  $V_{box}$  is volume of the box) is more consistent, and we do not observe the plateauing subtype of simulation. Comparing to systems of 1000 particles, the MSD observed also diverges significantly at longer timescales between the two system sizes. Given the clear finite size effects occurring here, we in general chose the population of  $N = 1000$  colloid simulations as the largest size we would reasonably be able to simulate.

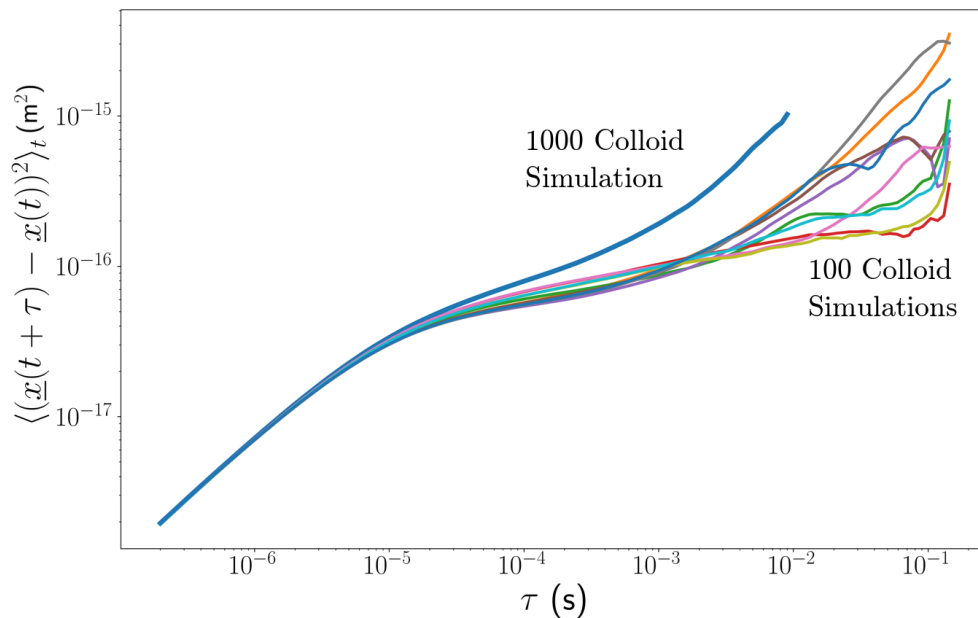
In general, the degree to which the simulations are converged will vary in several ways and depend on the measure we are discussing. Firstly, we have the finite size effects already mentioned, although the closer behaviour in multiple

## 4. QUIESCENT SIMULATIONS

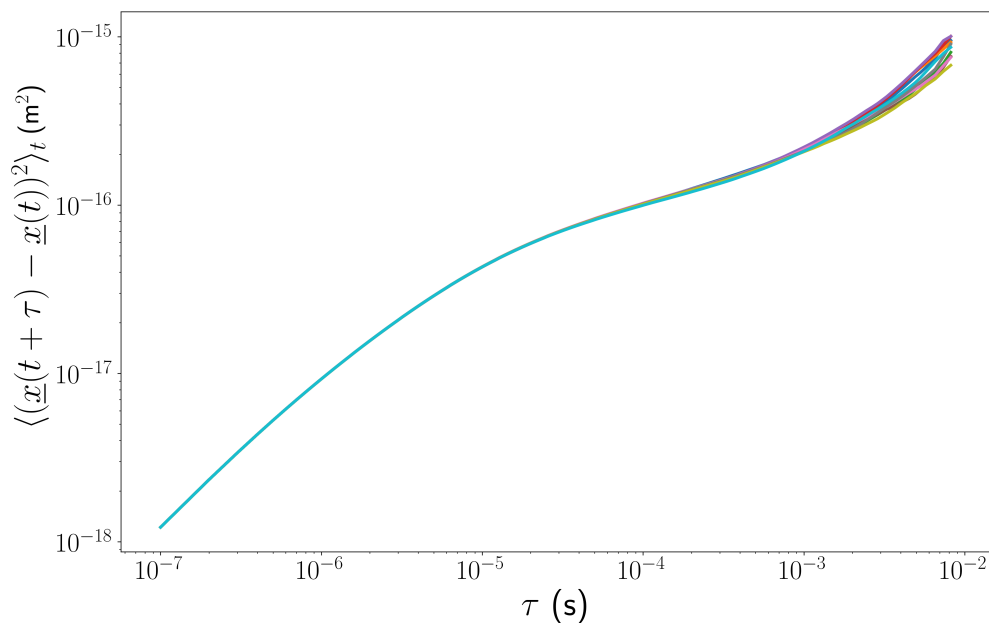
---

realisations of the system with the larger populations suggests that we have simulated a population that is at least somewhat close to convergence. Secondly, we can consider the resolution of the particles. As mentioned in [subsection 3.1.1](#), there is a balance between computational stability and efficiency and the resolution of the meshes used. Unlike many finite element approaches, we cannot arbitrarily increase the refinement of meshes due to the stochastic nature of the simulations. Refinement will increase the likelihood of element inversion due to stochastic stress, and relative strains will be larger due to smaller elements, as well as our elements eventually being so small their elements are smaller than atoms. Because of this, we must choose a level of coarse-graining, and therefore convergence to the behaviour of true sphere, for example, may not be perfectly attainable. Thirdly, in measures such as Mean Squared Displacement the longest timescales in a simulation of arbitrary length will not converge, i.e. we must simulate significantly longer than the timescale of interest to be confident of converged behaviour in a single simulation. Instead, one must simulate sufficient realisations of the same set of parameters, and infer through an ensemble that behaviour is converged. We have taken precautions to have the simulations as close to convergence as possible balanced against suitable performance to actually be able to observe interesting dynamics, and have sampled an ensemble to ensure these issues are not overwhelming otherwise. We also pursue multiple measures to verify the existence of unconverged behaviour at the longest timescales, i.e the second diffusive regime.

## 4.2 Repeated simulations and consistency



(a)



(b)

Figure 4.3: (a) Plot of MSD of 10 instances of 100-colloid systems at  $\zeta_e = 0.8$ , and a single instance of an 1000-colloid system at the same  $\zeta_e$ . The 100 colloid systems have significant variance in behaviour, and diverge significantly from the 1000-colloid results due to finite size effects. (b) Consistency in MSD of ten 1000 colloid simulations at  $\zeta_e = 0.8$ .

## 4. QUIESCENT SIMULATIONS

---

$\zeta_e$	$K$ (kPa)	$G$ (kPa)	No. of cells	Interaction Cutoff (m)	Steric Factor	No. of Vi- able Runs
0.6	12.34	3.700	25	$3.51 \times 10^{-8}$	$1 \times 10^{-5}$	3
0.7	12.34	3.700	26	$3.48 \times 10^{-8}$	$1 \times 10^{-5}$	7
0.8	12.34	3.700	26	$3.07 \times 10^{-8}$	$1 \times 10^{-5}$	10
0.7	8.00	2.400	45	$1.86 \times 10^{-8}$	$2.59 \times 10^{-5}$	9
0.7	4.00	1.200	45	$1.86 \times 10^{-8}$	$1.30 \times 10^{-5}$	9
0.6	2.00	0.600	45	$1.65 \times 10^{-8}$	$6.48 \times 10^{-6}$	10
0.7	2.00	0.600	45	$1.86 \times 10^{-8}$	$6.48 \times 10^{-6}$	10
0.8	2.00	0.600	45	$1.77 \times 10^{-8}$	$6.48 \times 10^{-6}$	10
0.9	2.00	0.600	45	$1.70 \times 10^{-8}$	$6.48 \times 10^{-6}$	10
1.0	2.00	0.600	45	$1.65 \times 10^{-8}$	$6.48 \times 10^{-6}$	10

Table 4.1: Table of parameters varied in quiescent simulations

### 4.3 Observed volume fraction

Before discussing any other results from the quiescent simulations, we must first discuss the actual observed volume fractions for these simulations. The behaviour of systems of monodisperse hard-sphere colloids are mainly characterised by the volume fraction  $\phi = \frac{nV}{V_{Tot}}$ , where  $n$  is the number of particles,  $V$  is the volume of a particle, and  $V_{Tot}$  is the total volume of the system. In a system of soft, compressible particles, we can only initialise systems according to the effective volume fraction  $\zeta_e = \frac{nV_0}{V_{Tot}}$ , where we use the uncompressed, undeformed volume of the colloid,  $V_0$ .

The difference between these may be instructive - to what extent does  $\phi$  alone determine the dynamics of soft colloidal systems? We can see from [Figure 4.4](#) that harder and softer systems often have quite similar  $\phi$  with different initial  $\zeta_e$ . So we can compare the results from simulations with similar  $\phi$  but different modulus, specifically:  $\zeta_e = 0.7, K = 2\text{kPa}$  and  $\zeta_e = 0.6, K = 12\text{kPa}$  have  $\phi = 0.594, 0.590$ , respectively;  $\zeta_e = 0.9, K = 2\text{kPa}$  and  $\zeta_e = 0.7, K = 12\text{kPa}$  have  $\phi = 0.684, 0.673$ ,

### 4.3 Observed volume fraction

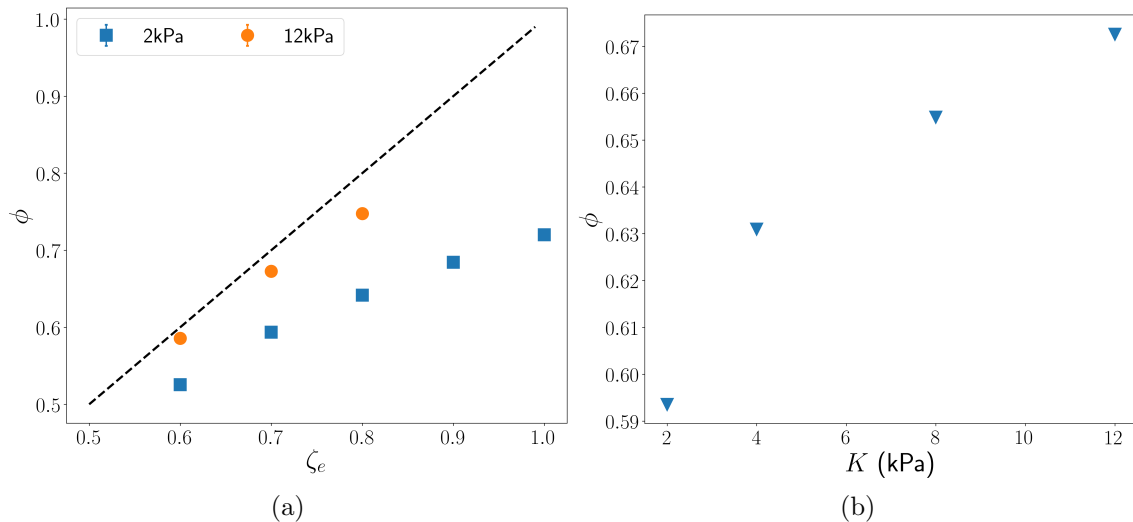


Figure 4.4: (a) Observed real volume fraction  $\phi$  versus  $\zeta_e$  for 12kPa and 2kPa series, dashed line indicates  $\phi = \zeta_e$ . (b)  $\phi$  versus bulk modulus  $K$ .

respectively; and finally  $\zeta_e = 0.8$ ,  $K = 2$  kPa has a value intermediate to  $\zeta_e = 0.7$ ,  $K = 4, 8$  kPa with  $\phi = 0.642, 0.631, 0.655$ , respectively.

The trends visible in Figure 4.4 are expected. As we increase  $\zeta_e$  in both harder and softer colloids,  $\phi$  increases. In both plots, we can see that higher moduli result in higher volume fractions. Interestingly, we do not see a  $\phi$  higher than approximately the limit of ordered hard-sphere packing,  $\phi = 0.74$ , and it appears from the limited data points we have that the curve could be approaching a maximum value. For those simulations where we can directly compare  $\phi$  and  $\zeta_e$ , increasing  $\zeta_e$  results in a larger deviation from  $\phi = \zeta_e$ . All sampling errors are smaller than the markers as plotted, so  $\phi$  is very closely determined by the corresponding  $\zeta_e$  and material parameters of the system. Observed  $\phi$  values are featured in parentheses on relevant plot legends to three significant figures in all subsequent plots. Without thermal fluctuations, we would expect  $\phi$  to be a

## 4. QUIESCENT SIMULATIONS

---

$\zeta_e$	$K$ (kPa)	$ \underline{q} $ Scaling	$S( \underline{q} )$ Scaling	$S( \underline{q} )$ Vertical translation
0.6	12.00	1.135	0.6	0.35
0.8	12.00	1.2	0.65	0.33
0.6	2.00	1.15	0.65	0.0.35
0.8	2.00	1.25	0.65	0.35
1.0	2.00	1.325	0.65	0.35

Table 4.2: Table of Scaling factors for Scattering radial profiles for various simulation parameters.

unique function of  $\zeta_e$ , especially as we disallow large overlaps. One such possible function appears in the work of [van der Scheer \*et al.\* \(2017\)](#).

### 4.4 Structure

To investigate the structure of the systems, we calculate for each checkpoint output from the simulation the average of the scattering intensity,  $|\rho_q|^2$ . We calculate  $\rho_q$  from:

$$\rho_q = \frac{1}{N_p} \sum_{\alpha}^{N_p} \exp(i\underline{q} \cdot \underline{r}_{\alpha}) \quad (4.1)$$

where  $\underline{r}_{\alpha}$  is the position of the centre of mass of particle  $\alpha$  and  $N_p$  is the number of particles. Since simulations are performed in a periodic box,  $\underline{q}$  is chosen from the set of wavevectors consistent with box periodicity, i.e.

$$\underline{q} = 2\pi \left( \frac{l}{L_x}, \frac{m}{L_y}, \frac{n}{L_z} \right) \quad (4.2)$$

where  $L_x, L_y, L_z$  are the simulation box length in the corresponding dimension and choices of  $l, m, n$  are integers. For computational efficiency, and to restrict

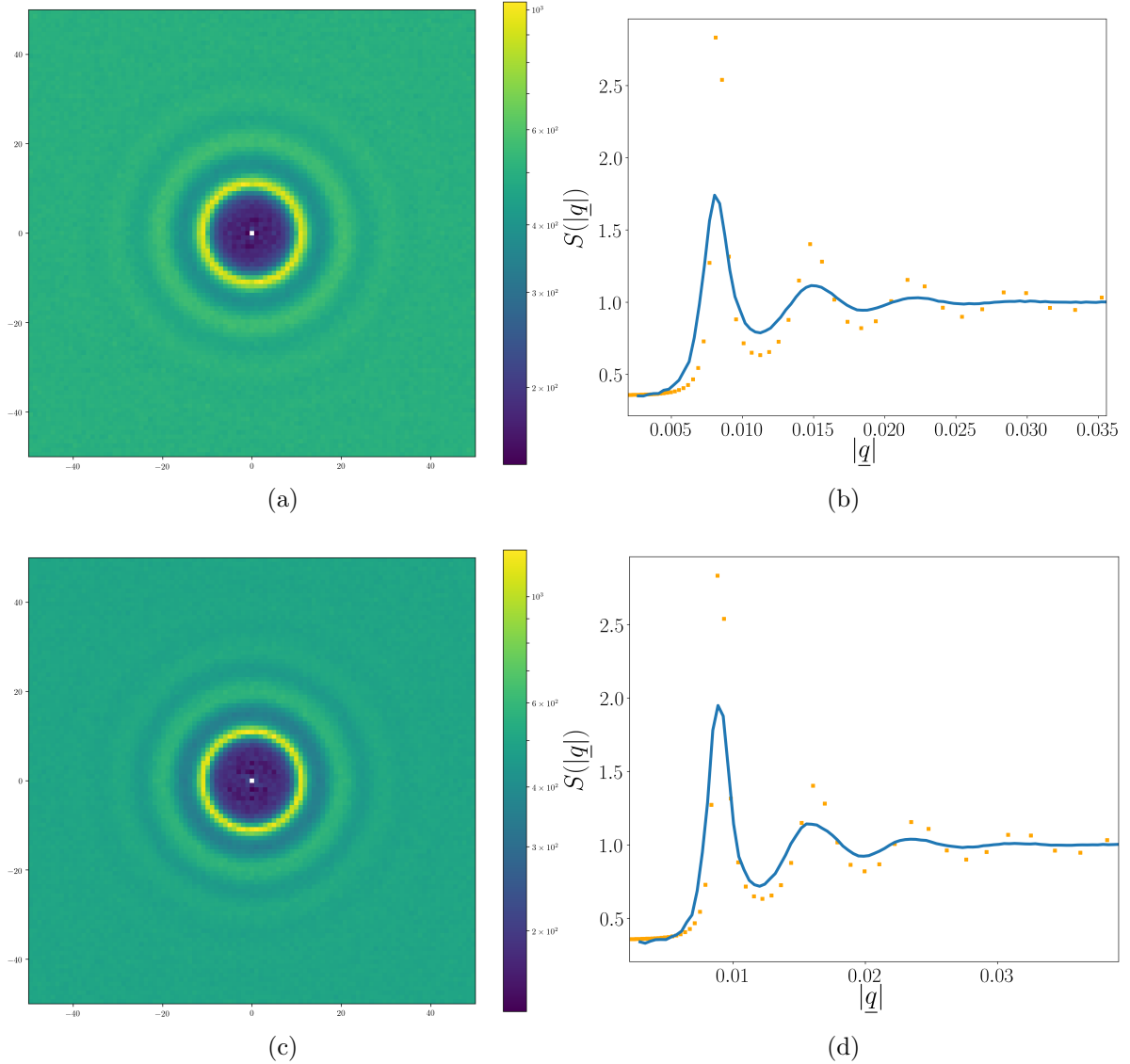


Figure 4.5: Representative sample of scattering amplitude averaged over  $x-y$ ,  $y-z$ ,  $x-z$  planes for all simulations and every 10<sup>th</sup> simulation checkpoint output at given parameter values. The solid line in radial profiles represent spherical average of the corresponding data, while the square markers represent Percus-Yevick behaviour (Percus & Yevick, 1958) for  $\phi = 0.55$  with an effective radius of the particles is 500nm, scaled to have a coincident first peak, y-intercept and high  $|q|$  value, as a representative example of amorphous hard-sphere behaviour. Results shown for (a)  $\zeta_e = 0.6$ ,  $K = 2\text{kPa}$ ,  $\phi = 0.525$ , (b) Radial profile of **a**, (c)  $\zeta_e = 0.8$ ,  $K = 2\text{kPa}$ ,  $\phi = 0.642$ , (d) Radial profile of **c**.

## 4. QUIESCENT SIMULATIONS

---

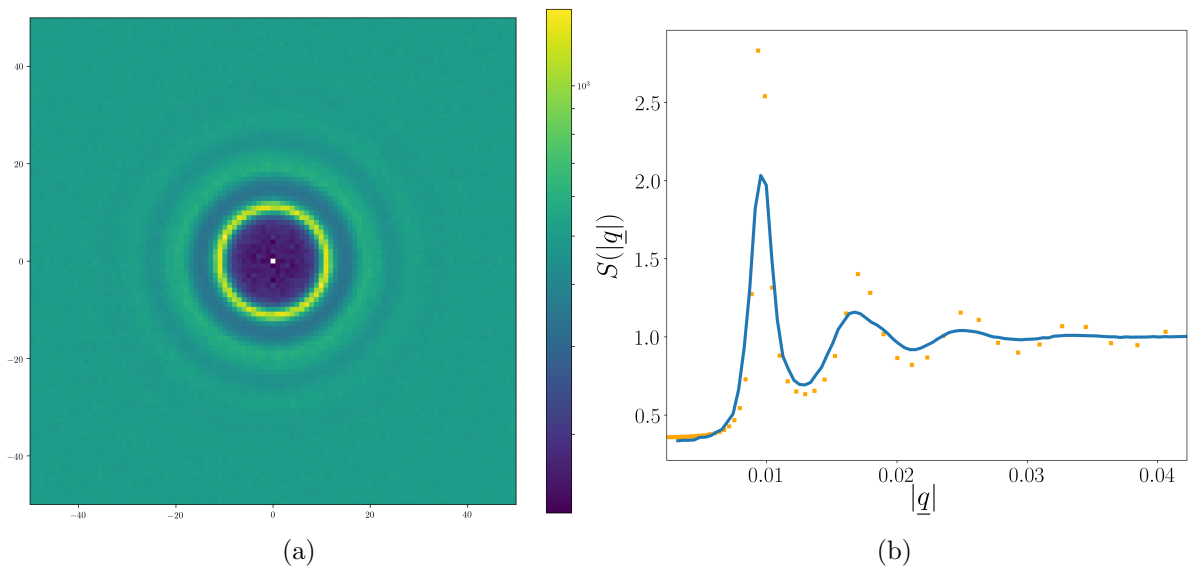


Figure 4.6: Representative sample of scattering amplitude averaged over  $x-y$ ,  $y-z$ ,  $x-z$  planes for all simulations and every 10<sup>th</sup> simulation checkpoint output at given parameter values. The solid line in radial profiles represent spherical average of the corresponding data, while the square markers represent Percus-Yevick behaviour (Percus & Yevick, 1958) for  $\phi = 0.55$  with an effective radius of the particles is 500nm, scaled to have a coincident first peak, y-intercept and high  $|q|$  value, as a representative example of amorphous hard-sphere behaviour. Results shown for (a)  $\zeta_e = 1.0$ ,  $K = 2\text{kPa}$ ,  $\phi = 0.720$ , (b) Radial profile of **a**.

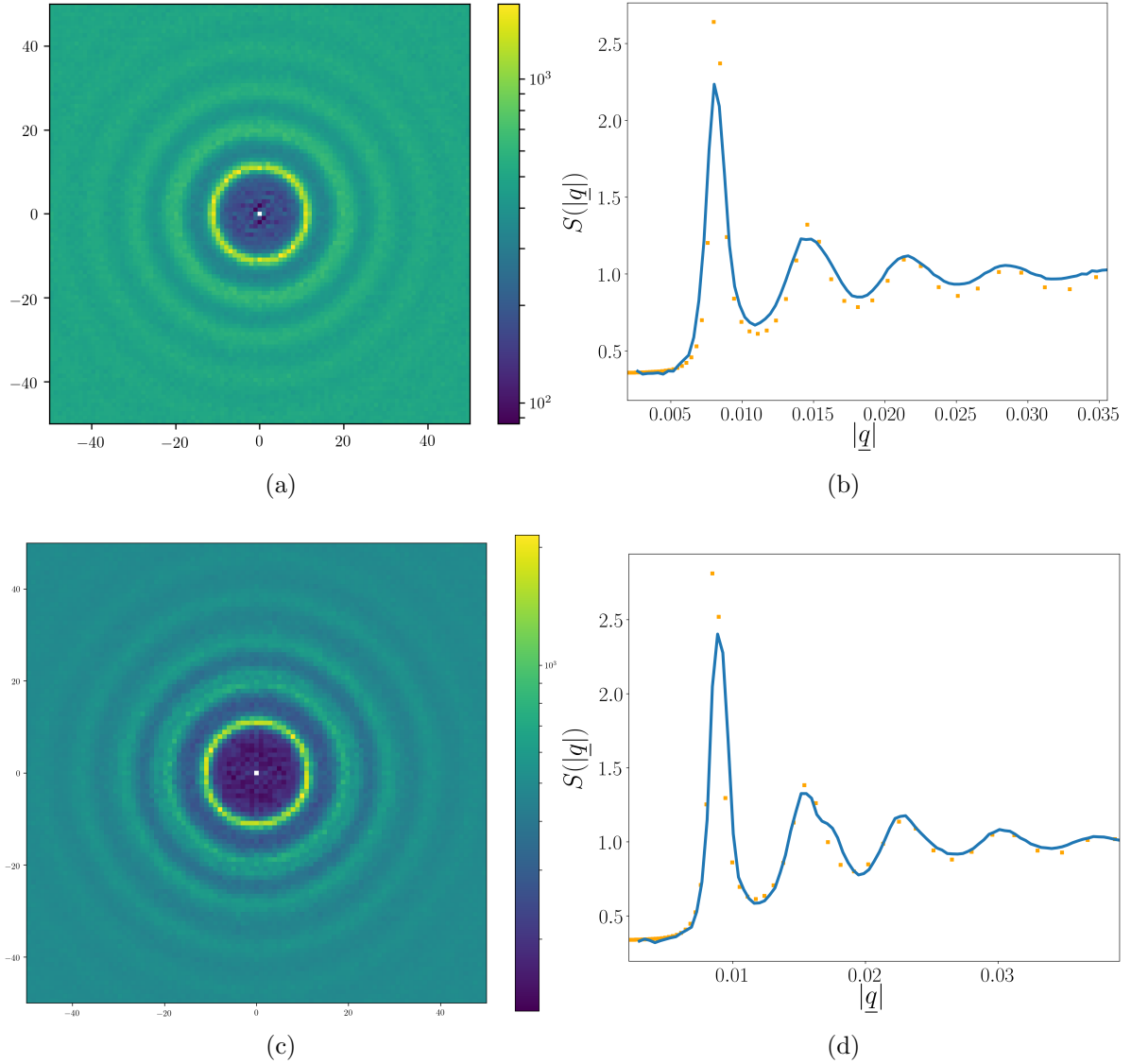


Figure 4.7: Representative sample of scattering amplitude averaged over  $x-y$ ,  $y-z$ ,  $x-z$  planes for all simulations and every 10<sup>th</sup> simulation checkpoint output at given parameter values. The solid line in radial profiles represent spherical average of the corresponding data, while the square markers represent Percus-Yevick behaviour (Percus & Yevick, 1958) for  $\phi = 0.55$  with an effective radius of the particles is 500nm, scaled to have a coincident first peak, y-intercept and high  $|q|$  value, as a representative example of amorphous hard-sphere behaviour. Results shown for (a)  $\zeta_e = 0.6$ ,  $K = 12\text{kPa}$ ,  $\phi = 0.586$ , (b) Radial profile of **a**, (c)  $\zeta_e = 0.8$ ,  $K = 12\text{kPa}$ ,  $\phi = 0.748$ , (d) Radial profile of **c**.

#### 4. QUIESCENT SIMULATIONS

---

the range of wavevectors to a two-dimensional plane, we restrict the range of integers to

$$l = 0, m = (-m_{max}, m_{max}), n = (-n_{max}, n_{max}) \quad (4.3)$$

$$m = 0, l = (-l_{max}, l_{max}), n = (-n_{max}, n_{max}) \quad (4.4)$$

$$n = 0, l = (-l_{max}, l_{max}), m = (-m_{max}, m_{max}) \quad (4.5)$$

where  $l_{max}, m_{max}, n_{max} = 50$ . We evaluate  $|\rho_q|^2$  for each  $\underline{q}$  for every tenth saved checkpoint step (or every  $10^{-4}$ s). All instances of each set of parameters and from all 3 planes are averaged into a single two-dimensional plane, as we would assume isotropy with monodisperse, identical particles. The resulting average intensity  $S(|\underline{q}|) = \langle |\rho_q|^2 \rangle$  is then colormapped logarithmically, and the results can be seen in [Figure 4.5](#), [Figure 4.6](#), and [Figure 4.7](#) for the same representative sample of parameter choices covered in [section 4.6](#), alongside a radial average of each scattering plot. This representative set of simulations was chosen to bound the parameter space we explore. Time constraints prevented calculation of this quantity for all simulated systems.

The quantity  $S(|\underline{q}|)$  is the three-dimensional Fourier transform of  $\langle \rho(r)\rho(0) \rangle = g(r)\rho_0^2$ . We will briefly discuss the features we would expect to see in various circumstances. In the case where crystalline order is present, we would expect to see clear peaks in a lattice ordering in the plot, which would correspond to the reciprocal lattice of whichever crystalline form was present. As we do not observe such peaks in any of the plots in this section, we will not discuss this in detail. These behaviours can be seen in [Foss & Brady \(2000\)](#). More broadly, if there is no long range order or crystallinity, the key features of these plots will come from

local order, so the nearest neighbour cage or at most the second shell. If there is a sharp, well defined nearest neighbour distance,  $S(|\underline{q}|)$  will feature multiple defined rings - when taking a radial profile, this signature would be similar to the Percus-Yevick profile (Percus & Yevick, 1958) we plot against. A broader distribution of distances will give fewer, broader rings. Finally, even if long range order is not present local correlations of non-contacting particles that still fall close to the nearest neighbour shell will give shoulders in those peaks, where the transform of the peaks from two different distances are superposed.

In Figure 4.5, Figure 4.6 and Figure 4.7, we can see that none of the systems display signs of crystallinity as no reciprocal lattice is visible. Focussing on the  $K = 2\text{kPa}$  simulations in Figure 4.5 and Figure 4.6 we can see only a few rings, suggesting that the distribution of nearest neighbour lengths is wide enough that the transform of this measurement is weak. For the  $K = 12\text{kPa}$  simulations in Figure 4.7, we can see significantly more rings, suggesting that the distribution of nearest neighbour distances is tighter, therefore giving a greater quantity of more pronounced peaks in the transform of this quantity. Additionally, we can clearly see in Figure 4.7d a shoulder in the second peak, which indicates that there is a local ordering close to hexagonal close packing, but only within the diameter of another particle. We can deduce this as longer range order would not show up as rings, and that a shoulder indicates there are two close but subtly different length scales at play. Additionally, the non-zero value of the  $y$ -intercept arises from the compressibility of the system.

We also compare the radial profile of our plots to the idealised hard sphere structure factor for amorphous monodisperse hard spheres, generated by using the SasView implementation of the Percus-Yevick (Percus & Yevick, 1958) model

#### 4. QUIESCENT SIMULATIONS

---

with an effective radius of 500nm and  $\phi = 0.55$ . This model was then scaled along the  $|q|$ -axis so that the position of the first peak coincides with the data, and then scaled in  $S(|q|)$  as  $S(|q|) = a + bS_{P-Y}(|q|)$  where  $a$  vertically translates and  $b$  scales the Perkus-Yevick result  $S_{P-Y}$  to give a rough visual aid for interpreting the results with matched  $y$ -intercept and high  $|q|$  values. These scaling quantities are included in [Table 4.2](#). Discussing the  $K = 12\text{kPa}$  results first, we can see that using this simple scaling we achieve a good agreement at both values of  $\zeta_e$ . We have matched the  $y$ -intercept and the approximate size and width of most of the peaks. We interpret this as that the structural arrangement of these colloids with harder moduli somewhat matches a significantly less packed amorphous system just below the onset of the glassy regime, where thermal rearrangement is still possible, though the actual  $\phi$  of these 12kPa systems is 0.59 and 0.74, compared to a scaled Perkus-Yevick curve for  $\phi = 0.55$ . It is important to remember the shoulder in [Figure 4.7d](#) - these are volume fractions that would be hexagonally close packed for hard spheres, but this is disrupted at any longer range by the softness and thermal activity of the colloids. Of note in the  $K = 2\text{kPa}$  simulations in [Figure 4.5](#) and [Figure 4.6](#) is that we cannot achieve good agreement with the Perkus-Yevick predictions. The peaks for these predictions are higher and narrower, and therefore persist to higher  $|q|$ , regardless of our choice of scaling. We also conducted this analysis on a  $K = 8\text{kPa}$ ,  $\zeta_e = 0.7$ , and found similar results to  $K = 12\text{kPa}$ ,  $\zeta_e = 0.6$ , indicating the structure cannot be used to differentiate between these simulation parameters, which as we will see in [Figure 4.9](#) give very similar mean-square displacement results. That we can effectively scale this hard-sphere theory for results for harder spheres that are still deformable, but not for the softer spheres is an interesting result, suggesting the softness allows for

quite different structuring than the harder counterpart. Given this observation, it is also interesting that the hexagonal close packing is still somewhat visible, suggesting short range order may vary with  $\phi$  while longer range order is destroyed by the softness of the particles.

## 4.5 Mean-Squared Displacement

### 4.5.1 Expected behaviour

As a first measure to probe rearrangement of particles, we choose the time-dependent Mean-Squared Displacement, or MSD, of their centre of mass. For free diffusion of a sphere in three dimensions, we would expect the standard results of  $\langle \underline{x}(\tau) \rangle = \underline{0}$  and  $\langle \underline{x}(\tau)^2 \rangle = 6D\tau$ , where  $x$  is the displacement over some time lag  $\tau$  as a scalar value, and  $D$  is diffusivity. This is because we expect each step in the diffusion of a free sphere to be uncorrelated in time and space, and therefore when sufficiently well sampled any exploration in one direction will eventually be cancelled out by an equivalent exploration in the opposite direction. However, the mean square displacement, considering the magnitude of the displacement and not its direction, will continuously grow.

In the case of a packed system where each particle is surrounded by a cage of other particles, we would expect the centre of mass of a particle to first explore its own cage in a manner similar to a free particle. It would then transition to experiencing caging effects, and enter a regime where it is more restricted by its cage. If the particles are truly caged, then this plateau would continue indefinitely. However, if the particles are able to rearrange to escape their cage,

## 4. QUIESCENT SIMULATIONS

we would expect to see a second diffusive regime, in which  $\langle \underline{x}(\tau)^2 \rangle$  is again roughly proportional to  $\tau$ , but with a smaller diffusivity. Here, hopping between the cages is analogous to diffusion on a discrete grid. In addition to plotting MSD versus  $\tau$ , we also show  $\frac{\langle \underline{x}(\tau)^2 \rangle}{\tau}$  versus  $\tau$ . In the latter, we would expect diffusive regimes to be plateaus, with the plateau value of  $6D$ , and caged regimes to be downward slopes. As discussed in [section 3.4](#), the displayed results for MSD have the diffusion of the entire system removed from particle displacements.

### 4.5.2 Results and discussion

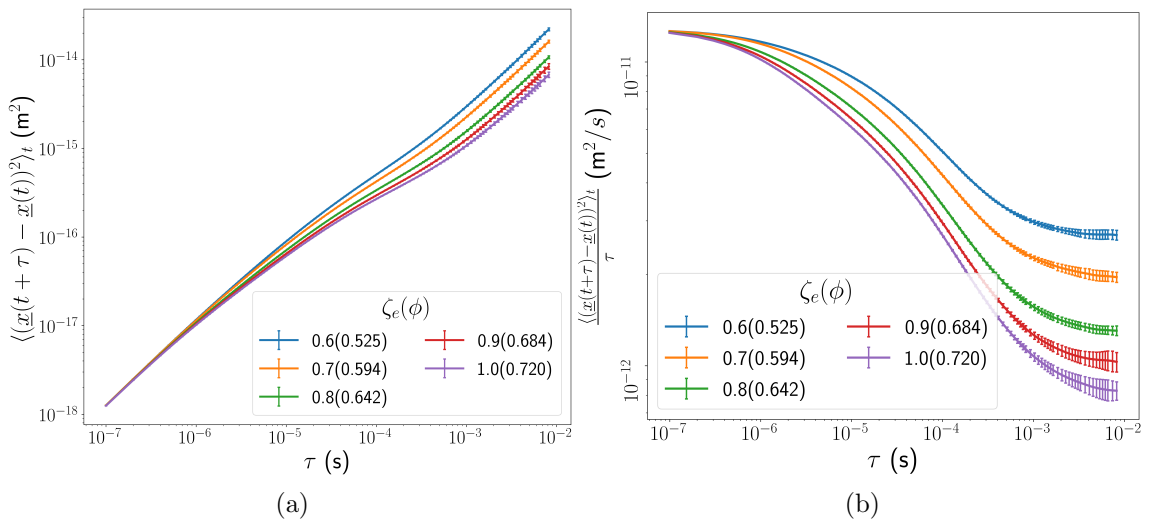


Figure 4.8: MSD of [2kPa varied  $\zeta_e$ ]: (a) Simple MSD, (b) MSD divided by  $\tau$ .

First, we discuss the [2kPa varied  $\zeta_e$ ] Simulations. We can see clearly in [Figure 4.8a](#) that while these systems all appear to have 3 regimes in their MSD, they do not exhibit a strong plateau in the MSD. Although the particles in these systems are experiencing some caging effects, they are not experiencing them strongly enough to obviously produce a true cage at any timescale. We can also

## 4.5 Mean-Squared Displacement

---

see that while the  $\zeta_e = 0.6$  curve appears to have little deviation from diffusive behaviour plotted in this manner, the middle regime where caging is most strongly felt grows more pronounced as the effective volume fraction is raised, and is most clear when  $\zeta_e = 1.0$ .

Looking instead at [Figure 4.8b](#), we can see the 3 distinct regimes quite clearly when divided through by  $\tau$ . This is a consequence of dividing MSD by  $\tau$  to remove the leading order diffusive behaviour: as a result the y-axis in [Figure 4.8b](#) covers a range of 1 decade, so that the 3 regimes are clear. Here plateaus are diffusive regimes, and downward slopes are caging effects. We can see in the short timescales that the higher volume fractions feel their cage more strongly and sooner, curving off the plateau immediately, whereas  $\zeta_e = 0.6, 0.7$  briefly have an initial diffusive plateau before fully experiencing their cage. All appear to return towards a plateau, indicating the emergence of a second diffusive regime, between cages. While they may not have fully reached that plateau, with the corroboration of the analysis included in the rest of the chapter, a return to a second diffusive regime is certainly indicated.

For the MSD results for the [ $\zeta_e = 0.7$ , Varied  $K$ ] systems in [Figure 4.9](#), we must first observe that the 8kPa and 12kPa results track each other almost exactly in longer timescales. This is an intriguing result, but is possibly an artifact of the difference in surface interaction length discussed in [section 4.2](#). This is therefore likely a demonstration of softness of particles being quite difficult to define - both the interactions between particles and the material parameters of the particles themselves contribute to the effective softness and dynamics. It is also interesting that on short timescales the 12kPa system tracks the 4kPa system before switching to the 8kPa.

## 4. QUIESCENT SIMULATIONS

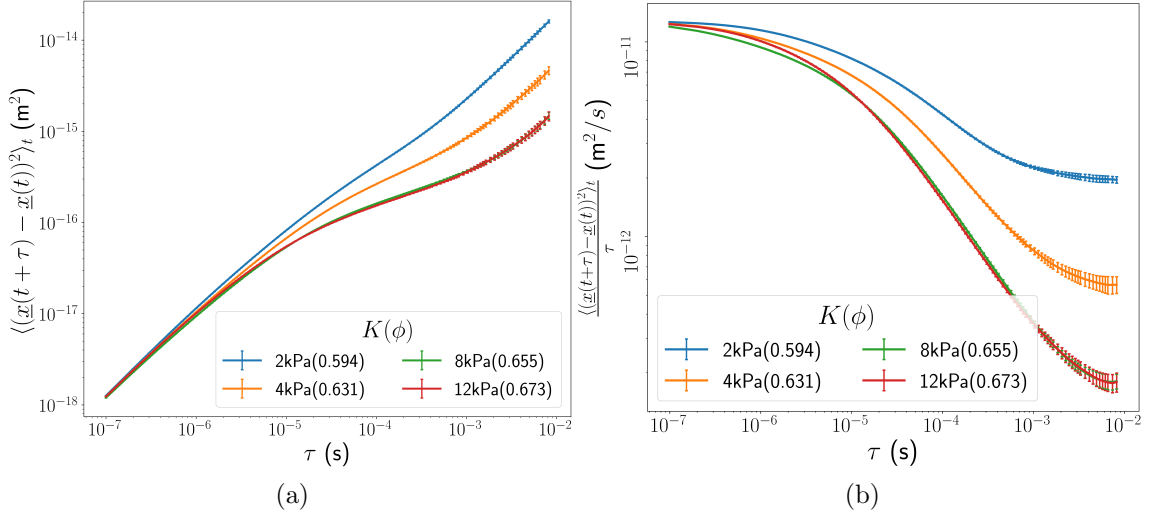


Figure 4.9: MSD of  $[\zeta_e = 0.7, \text{ Varied } K]$ : (a) Simple MSD, (b) MSD divided by  $\tau$ .

As we increase the moduli, we can see that the middle, caged regime is more obviously separate from the entirely diffusive regimes, and in a more significant way than when was obtained by varying  $\zeta_e$ . It would be interesting in further work to attempt to simulate higher volume fractions for this reason - we are comparing logarithmic variation in moduli to a geometric variation in  $\zeta_e$  at the low modulus of 2kPa. Again, [Figure 4.9b](#) makes clear that at least 2 clear regimes exist in all cases, and there is a tendency towards a 3rd emerging.

Finally, we present the [2kPa varied  $\zeta_e$ ] simulations. We can observe the three regimes in [Figure 4.10a](#) for all packing fractions, with the middle regime more pronounced at higher  $\zeta_e$ . In [Figure 4.10b](#) we can see that again, the higher the  $\zeta_e$ , the earlier the cage is felt. We can also observe that none of these systems have fully established a second diffusive regime.

In [Figure 4.11](#), we compare systems from the previous datasets with similar

## 4.5 Mean-Squared Displacement

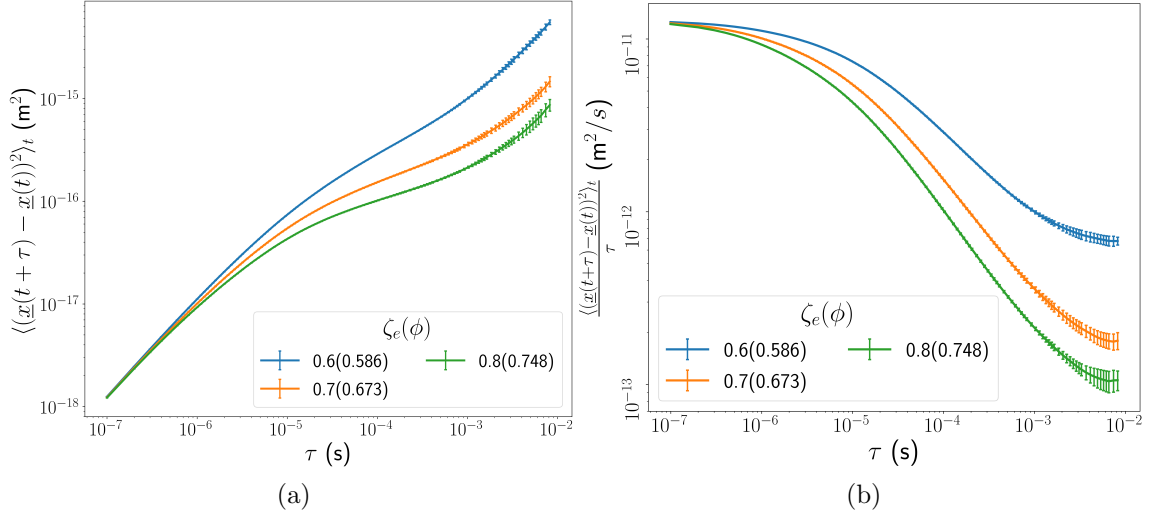


Figure 4.10: MSD of [12kPa varied  $\zeta_e$ ]: (a) Simple MSD, (b) MSD divided by  $\tau$ .

observed volume fraction  $\phi$ . From this we can assert that the dynamics of these soft colloidal systems do not appear to be dictated entirely by their volume fraction, but rather that the modulus of the colloids is also a strong determining factor for the dynamics. Of note is that short timescale behaviour is quite similar between systems of similar  $\phi$ , which is a sensible but perhaps not obvious result. Cage size is likely to be defined largely by  $\phi$  and therefore the time for the centre of mass to diffuse long enough to encounter the resistance of that cage is likely to be similar, even though the resistance of that cage is quite different.

To approximate the diffusion coefficient,  $D$ , we assume diffusive behaviour, i.e.  $\langle r^2 \rangle = 6D\tau$ , and use the final value from each  $\frac{\langle (x(t+\tau) - x(t))^2 \rangle_t}{\tau}$  curve. As these simulations have not definitively reached their second diffusive plateau, these are approximations and we cannot reasonably calculate error, but they may still be instructive. We can see these values plotted against observed volume fraction  $\phi$  in [Figure 4.12](#) for the series [2kPa varied  $\zeta_e$ ], [12kPa varied  $\zeta_e$ ], [ $\zeta_e = 0.7$ ,

## 4. QUIESCENT SIMULATIONS

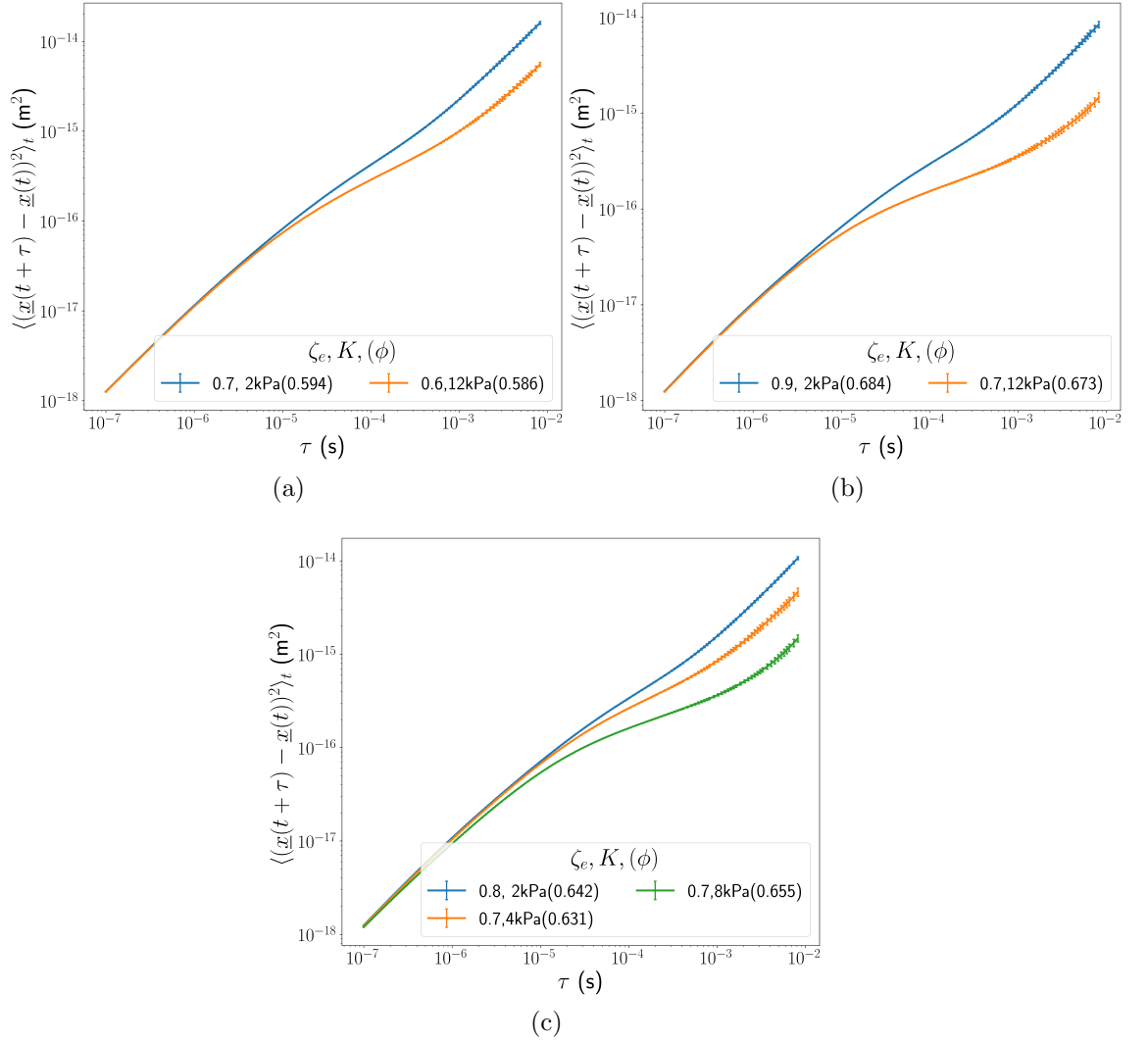


Figure 4.11: Comparisons of MSD for systems with similar  $\phi$ : (a) Systems with  $\phi \simeq 0.59$ , (b) Systems with  $\phi \simeq 0.68$ , (c) Systems with  $\phi \simeq 0.64$ .

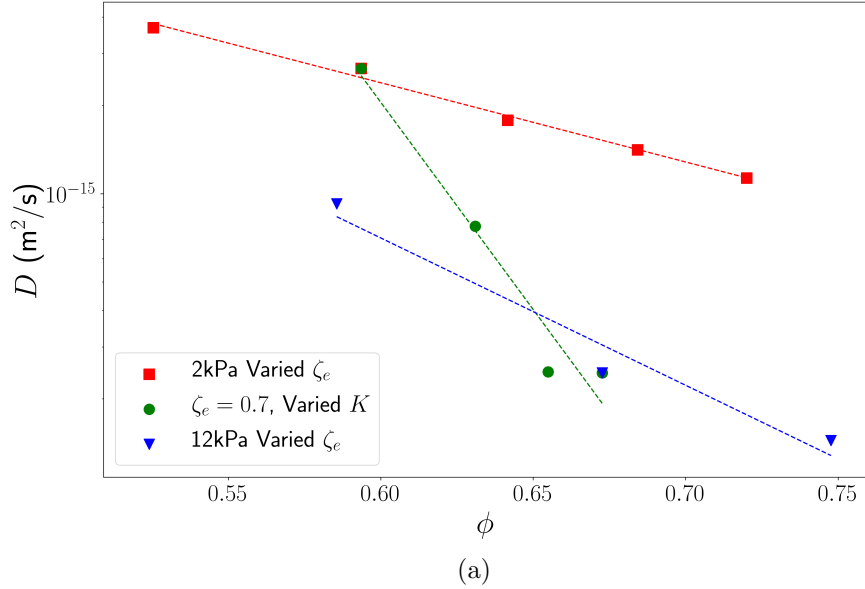


Figure 4.12: Approximate diffusivities against  $\phi$  for all simulations.

varied  $K$ ]. Here we confirm that similar volume fractions do not necessarily have similar diffusivities, and therefore that the material properties of the colloids are relevant to the mobility of the colloids as well as the volume fraction. For the softest colloids, we can see that the relationship between  $D$  and volume fraction  $\phi$  is roughly linear, whereas for the hardest this is less clear - there may be a curve in this data, but we have too few datapoints to be sure. This linear behaviour to non-linear or a different linear behaviour, if confirmed, could be symptomatic of a transition into a different regime.

Additionally, we can discuss the lengthscale of cage-breaking, which has two components; the displacement of a single particle moving between cages, and the lengthscale of any cooperative deformation that may occur between multiple shells of particles. The first we can extract from the MSD at the second shoulder,

## 4. QUIESCENT SIMULATIONS

---

which we would expect to be approximately the average diameter of a compressed particle, which we find to be correct. We can see in [Figure 4.8a](#), [Figure 4.10a](#) and [Figure 4.9a](#) that increasing the moduli and effective volume fraction  $\zeta_e$ , which both lead to lower volume fraction  $\phi$ , gives lower lengthscales of rearrangement. All of these values are within approximately one compressed particle diameter. The second is harder to directly calculate using the information we have measured and analysed within this work. However, we can estimate it using evidence discussed in [subsection 4.2.2](#): the smaller simulations clearly have finite size effects at play, suggesting a lengthscale longer than 2 particle diameters radially around any given particle, given a population of 100 particles is a little under five in each spatial dimension. That these finite size effects are significantly less at 1000, or ten in each spatial dimension, suggests a lengthscale in these simulations of less than approximately 5 particle diameters, though subtler effects may remain at still larger populations.

To conclude, we can in general observe that there is a tendency towards a second diffusive regime in all cases. Higher  $\zeta_e$  and higher moduli both result in the particle feeling the cage at shorter timescales and in more pronounced ways, as would be expected. We have also found that the dynamics of these systems do not appear to be dominated simply by the true volume fraction  $\phi$ , except possibly on the shortest timescales. These conclusions have much in common with the results for softer potentials in [Gnan & Zaccarelli \(2019\)](#), where colloids are represented 2-dimensionally by a ring of particles experiencing a Hertzian potential, which acts to capture shape deformation information. A key difference is that the simulations we present uniformly display two diffusive regimes with an intermediate caged regime, whereas their simulations display similar regimes to ours at lower volume

## 4.6 Visualisation of trajectories of colloids

---

fraction, to a truly caged state at a higher volume fraction, and finally re-entrant melting at still higher volume fraction, although at much higher  $\zeta_e$  than we probe in this thesis, and with a potential that does not easily map onto our parameters for comparison. Closer to our results are the three-dimensional simulations of [Lo Verso \*et al.\* \(2016\)](#), using deformable coarse-grained MD models of spherical nanoparticles, going to  $\zeta_e$  of well above two and not observing this re-entrant melting behaviour, though they only report this for a single type of nanoparticle, and it is unclear how our continuum moduli would correspond. Similar results were also observed in the work of [Gebremichael \*et al.\* \(2001\)](#) with bead-spring simulations of polymer melts, and in [Holler \*et al.\* \(2018\)](#) probing the MSD of branch points in entangled star polymers. In terms of experimental results, the three regimes we observe are largely seen for sub-glassy volume fractions for hard sphere colloids ([Hunter & Weeks, 2012](#); [Weeks & Weitz, 2002](#)), but have also been observed in soft colloidal experimental systems such as [Yoon \*et al.\* \(2018\)](#) using Diffusion Wave spectroscopy to extract MSD at  $\phi = 0.6$ , although extracting measurements at higher volume fractions is challenging due to the sheer number of objects to resolve.

## 4.6 Visualisation of trajectories of colloids

In this section we use the simulation trajectories to corroborate the occurrence of rearrangement. We do this by showing a representative sample of visualised trajectories of the particles with the highest displacement over the course of the simulation. We show their behaviour matches what we would expect for an initially caged particle that eventually breaks its cage.

## 4. QUIESCENT SIMULATIONS

---

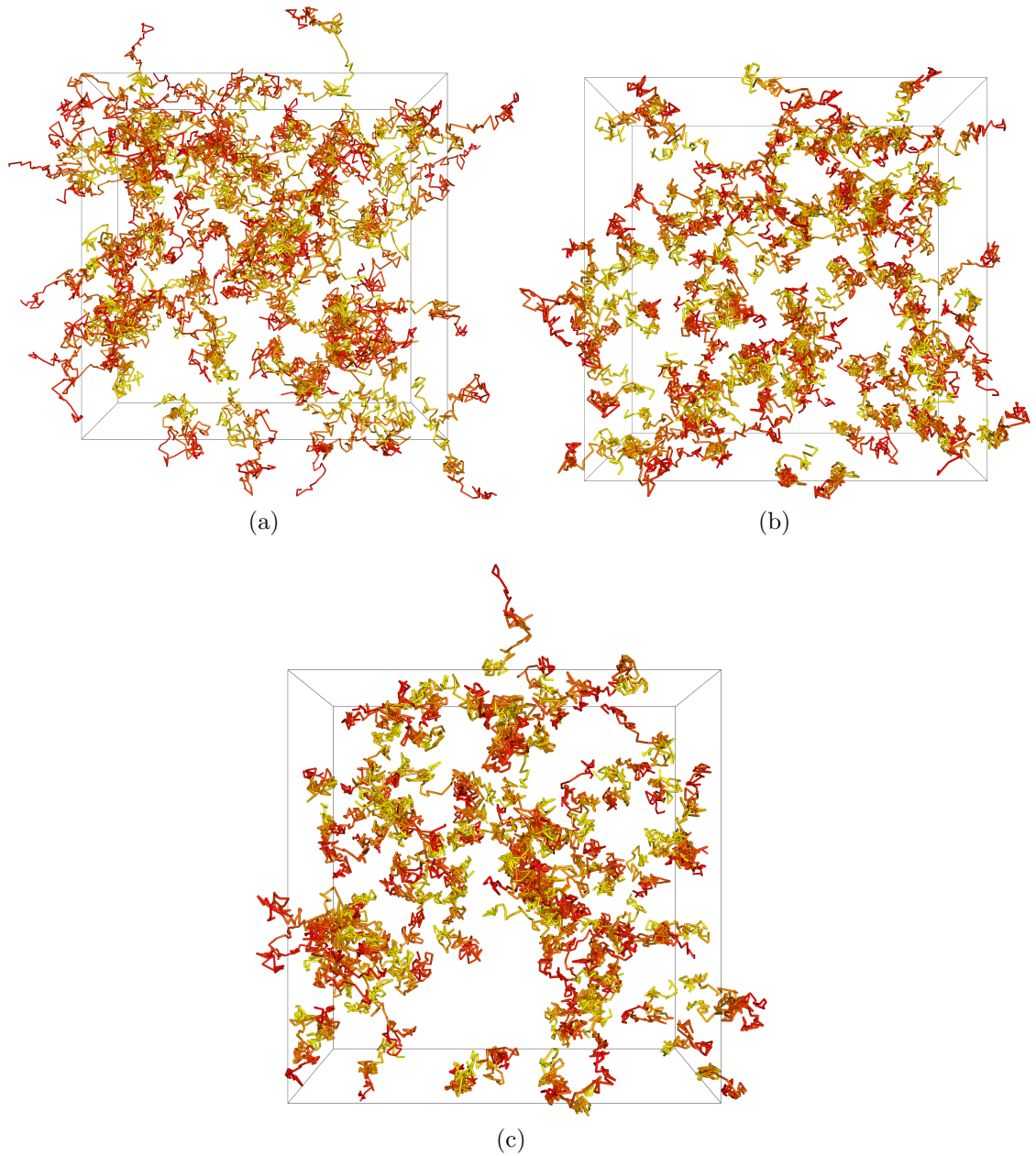


Figure 4.13: Representative sample of particle trajectories for 50 particles with highest displacement over course of simulation. Particle begins at yellow and transitions to red, with each section of the trajectory representing displacement over  $10^{-4}$ s. Results shown for systems where  $K = 2\text{kPa}$ : (a)  $\zeta_e = 0.6$ ,  $\phi = 0.525$ , (b)  $\zeta_e = 0.8$ ,  $\phi = 0.642$ , (c)  $\zeta_e = 1.0$ ,  $\phi = 0.720$ .

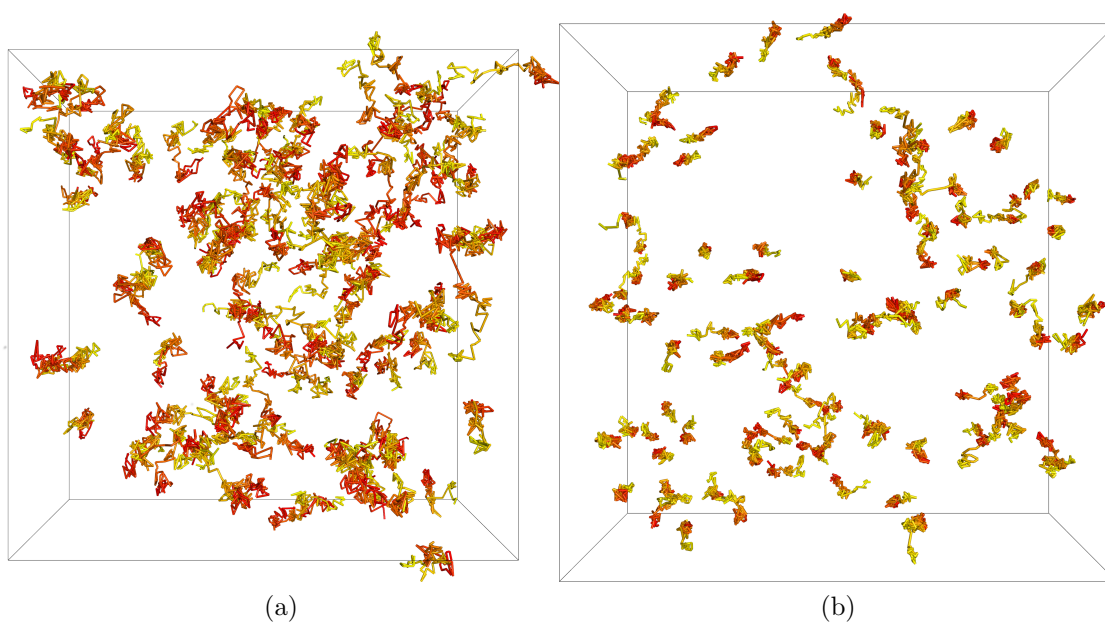


Figure 4.14: Representative sample of particle trajectories for 50 particles with highest displacement over course of simulation. Particle begins at yellow and transitions to red, with each section of the trajectory representing displacement over  $10^{-4}$ s. Results shown for systems where  $K = 12\text{kPa}$ : (a)  $\zeta_e = 0.6$ ,  $\phi = 0.586$ , (b)  $\zeta_e = 0.8$ ,  $\phi = 0.748$ .

## 4. QUIESCENT SIMULATIONS

---

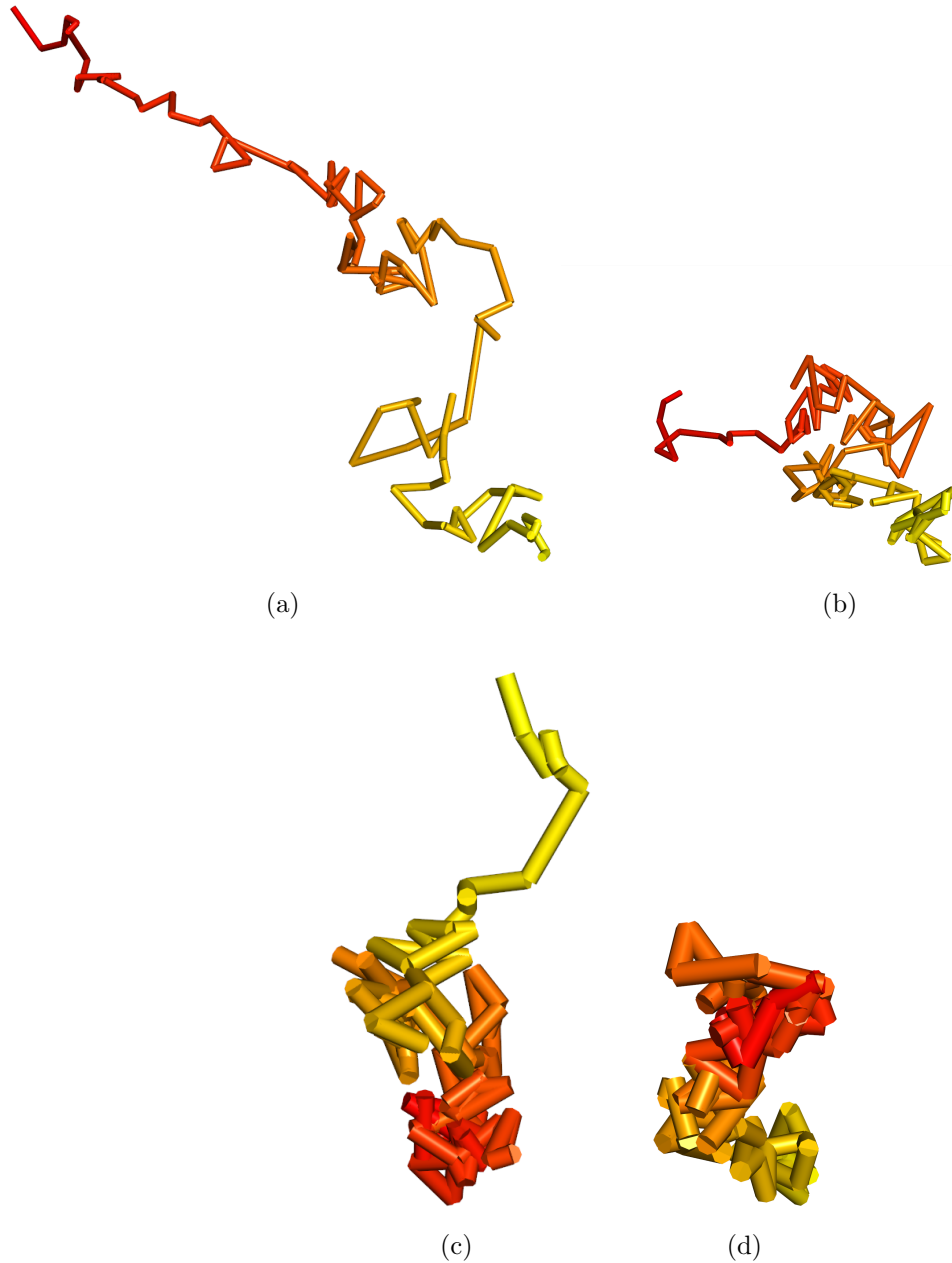


Figure 4.15: Single particle trajectories of particle with highest displacement over course of simulation. Particle begins at yellow and transitions to red, with each section of the trajectory representing displacement over  $10^{-4}$ s. Results shown for softest, least packed system and most packed hard system: (a)  $\zeta_e = 0.6$ ,  $K = 2\text{kPa}$ ,  $\phi = 0.525$ . (b) 50th highest displacement particle in simulation a, showing more intermittent cage breaking. (c)  $\zeta_e = 0.8$ ,  $K = 12\text{kPa}$ ,  $\phi = 0.748$ . (d) 50th highest-displacement particle in simulation c, showing a greater degree of caging.

## 4.6 Visualisation of trajectories of colloids

---

Figure 4.13 and Figure 4.14 show a representative sample of visualisations of particle trajectories, chosen from simulations at the boundary of the parameter space. If we observe common behaviour in these, it is likely that the simulations within with intermediate parameter choices also share these behaviours. These images take the 50 particles with the largest displacement over the course of the simulation and show the 3-D trajectories of those particles over  $9 \times 10^{-3}$ s.

For particles jumping between cages, we expect a period in which they ‘rattle’ in their cages (many low displacement jumps confined to a local area) followed by occasional escapes (particles travel a significant distance in a short time). We would expect very few particles to experience multiple jumps, given that we have not definitively reached a second diffusive regime with the timescales we have access to. Indeed, this is what we observe, across the full range of simulation parameters, with a representative sample of single particles shown in Figure 4.15. An example of similar plots can be seen in [Holler \*et al.\* \(2018\)](#).

As we raise the volume fraction, we can see that the particle trajectories become more confined, and we have fewer large jumps, and likewise when the particle moduli increase. We can see that the  $\zeta_e = 0.6$ ,  $K = 2$ kPa system appears relatively unconfined, while the  $\zeta_e = 0.8$ ,  $K = 12$ kPa system is almost entirely confined, with only a few cage escapes even when viewing the 50 particles with largest displacement. All  $K = 2$ kPa systems experience greater rearrangement, and even the most packed of those systems still appears to contain particles that change cages multiple times.

One might expect to see some correlation or clustering of particles with large displacement, i.e. motion of one particle creates motion of others nearby, as has been observed in both hard and soft sphere systems, both experimentally

## 4. QUIESCENT SIMULATIONS

---

and with simulation (Franklin & Weeks, 2014; Gnan & Zaccarelli, 2019; Laevi & Glotzer, 2004; Rahmani *et al.*, 2012). In general, it does appear that there may be a weak clustering of the particles with largest displacement, or possibly even a network of rearrangements. Speculating this from visual evidence is very poorly-sampled, as we show only a single realisation. This means the evidence is quite weak at this time. This would require a quantitative measure in future work.

### 4.7 Peak in non-Gaussian behaviour

As another tool to assess the particle dynamics and whether we have truly reached timescales sufficient to observe an approach to a second diffusive regime, we investigate how Gaussian the behaviour of the systems appear. That is, we assess whether there is a move away from Gaussian behaviour paired with a subsequent partial relative return to Gaussian behaviour. For a random walk in three-dimensional space, we would expect the probability distribution of particle displacements over a fixed time interval to be a Gaussian, or Normal, distribution. This is due to the Central Limit Theorem. The sum of a large number of random variables (i.e the displacement of diffusing particles) should be a Gaussian distribution. However, one of the ways this theorem can begin to fail is when a small number of the elements of this sum are extremely large, so that the sum is dominated by a few large values. In the case where we are only beginning to approach the second diffusive regime, only a few particles will have broken their cages - meaning a very few particles take large steps, and the distribution will diverge from Gaussian behaviour. Once the timescale reaches closer to a true diffusive

## 4.7 Peak in non-Gaussian behaviour

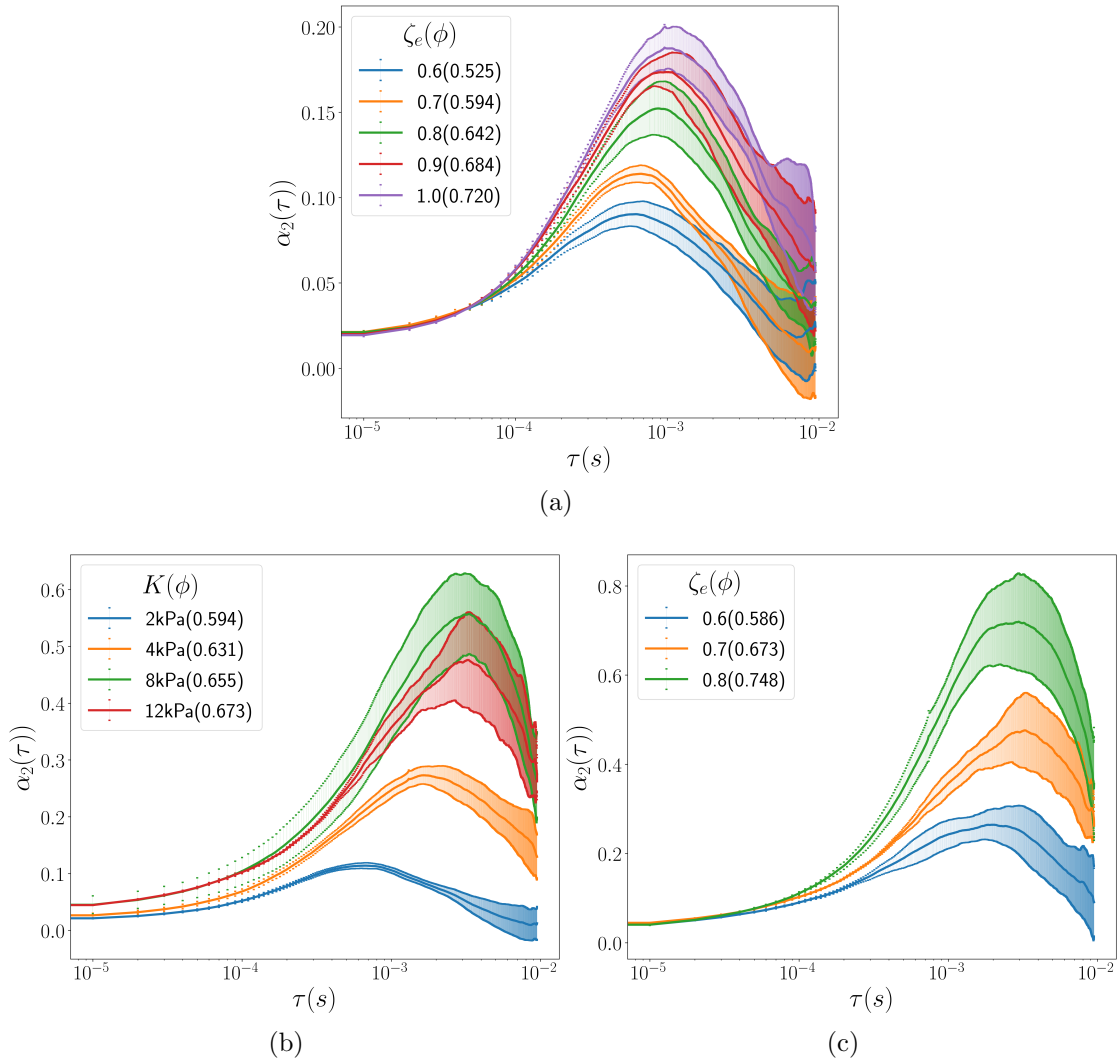


Figure 4.16: Non-gaussian parameter  $\alpha_2(\tau)$  for each set of parameters for (a) 2kPa varied  $\zeta_e$ , (b) Varied moduli,  $\zeta_e = 0.7$ . (c) 12kPa varied  $\zeta_e$ .

#### 4. QUIESCENT SIMULATIONS

---

regime, we return to a Gaussian behaviour, with motion between cages rather than diffusion of the centre of mass within a cage. This measure has been used for some time in the study of glassy dynamics, where they expected and observed the results outlined here: for a numerical model for cage to cage movement glassy dynamics (Vorselaars *et al.*, 2007); with confocal microscopy with packed samples (Weeks *et al.*, 2007); in mobility of colloidal liquid crystals (Cuetos *et al.*, 2018); in shear melting of a colloidal glass (Eisenmann *et al.*, 2010); in glassy behaviour at grain boundaries of colloidal crystals (Nagamanasa *et al.*, 2011). All measures in this section were based on post-processed data from trajectory files (i.e not calculated during simulation), and therefore cover only timescales from  $10^{-5}s$  to  $10^{-2}s$  at most. We calculate error bars through taking the sample standard deviation from the multiple instances of each set of parameters.

We initially calculate a Non-Gaussian parameter. Our choice of Non-Gaussian parameter  $\alpha_2(\tau)$  (Vorselaars *et al.*, 2007; Weeks *et al.*, 2000) is:

$$\alpha_2(\tau) = \frac{\langle \Delta \underline{r}(\tau)^4 \rangle}{\frac{5}{3} \langle \Delta \underline{r}(\tau)^2 \rangle^2} - 1. \quad (4.6)$$

where  $\Delta \underline{r}(\tau) = |\underline{r}(t_0 + \tau) - \underline{r}(t_0)|$  for some time lag  $\tau$ . This measure will be zero when behaviour is Gaussian, and can peak and then fall for a move from a caged regime to a diffusive regime as in Vorselaars *et al.* (2007).

As we can see from Figure 4.16, we have a peak in Non-Gaussian behaviour in all simulations, followed by a return to Gaussian behaviour closer to the full timescale of the simulations. This peak has a mild tendency to occur at longer timescales as we increase both  $\zeta_e$  and  $K$ , apart from the most packed system at  $K=2\text{kPa}$ . We can also see that the return to Gaussian behaviour is almost com-

## 4.7 Peak in non-Gaussian behaviour

---

plete (i.e values of  $\alpha_2$  are close to zero) in the less packed  $\phi = 2\text{kPa}$  simulations, indicating that these have reached the second diffusive regime, while the more packed and harder simulations still have high values of  $\alpha_2$  at longer timescales. This indicates that while the peak, and subsequent fall of  $\alpha_2$  is universal in our simulations and all are tending towards a return to the diffusive regime, not all have reached it, and the harder and more packed the system is, the less likely it is to have returned to the second diffusive regime in simulated timescales.

We can also see that the modulus  $K$  has the most significant effect on the magnitude of  $\alpha_2(\tau)$ . We can also observe that the  $K=12\text{kPa}$  simulations have a lower peak than the  $8\text{kPa}$  simulations, which we interpret as arising from the longer interaction length for the  $12\text{kPa}$  as discussed in [section 4.2](#). Another observation is that the non-Gaussian parameter for glassy or supercooled systems is typically 1-6 ([Guan \*et al.\*, 2014](#)), while values for the simulated systems here are far below this number. As our systems are fluids in all cases, we can see this as a manifestation of the fluidity of the system and softness of the particles.

We again plot systems with similar  $\phi$  in [Figure 4.17](#). Here we see that the non-Gaussian behaviour of these systems differs quite significantly, with higher values at longer timescales for systems with higher moduli. In [Figure 4.17c](#) especially, we see that the system with intermediate  $\phi$  has the lowest value and earliest peak, again confirming that  $\phi$  alone is not a sufficient predictor of the dynamics of these soft systems. To further probe the deviation from Gaussian distribution of particle displacement, we also construct histograms of particle displacements  $\Delta \underline{r}(\tau) = |\underline{r}(t_0 + \tau) - \underline{r}(t_0)|$  with various time lags  $\tau$ , and compare it to the Probability Distribution Function (PDF) we would expect for a Gaussian system

## 4. QUIESCENT SIMULATIONS

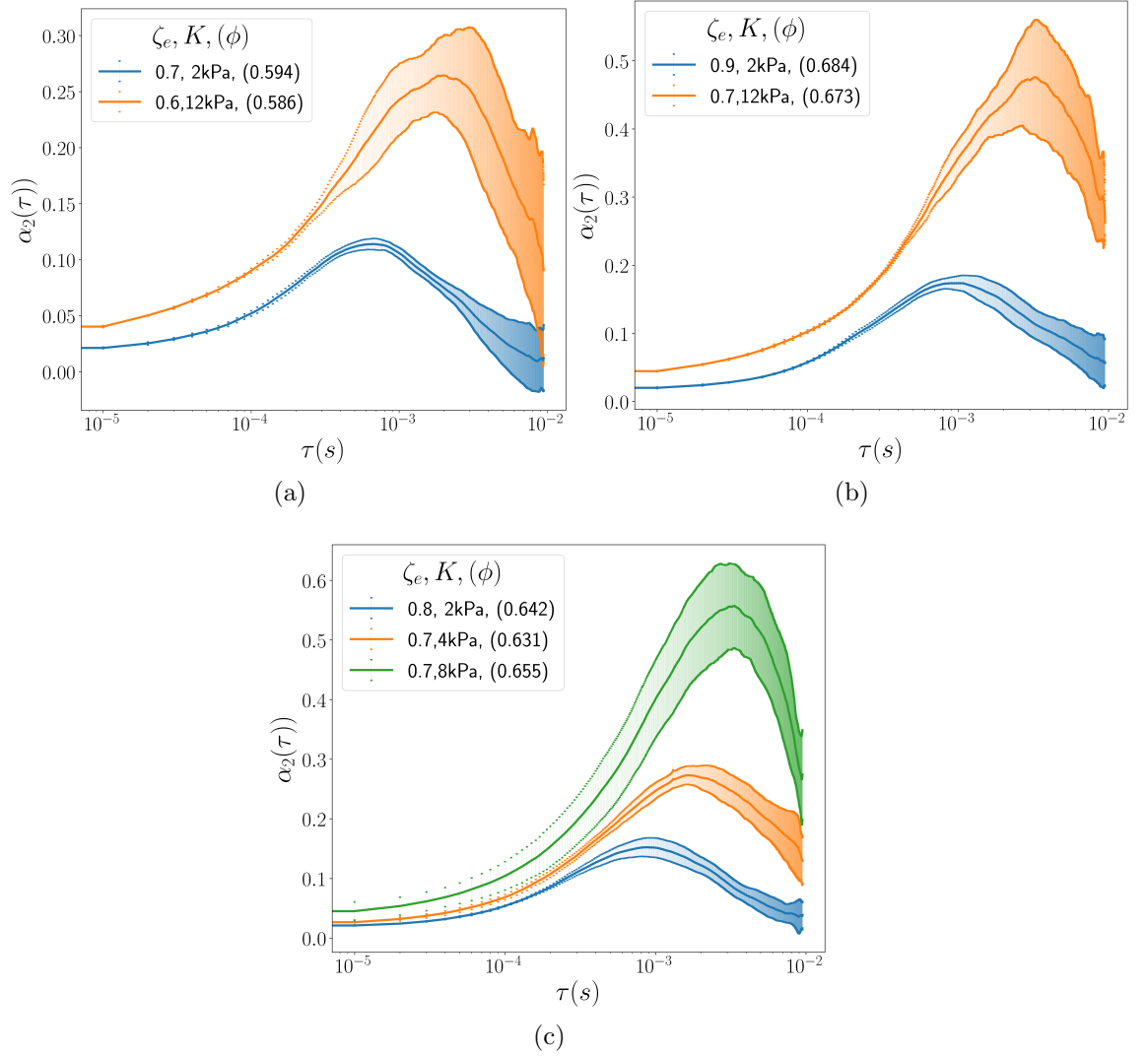


Figure 4.17: Comparisons of non-Gaussian parameter  $\alpha_2$  for systems with similar  $\phi$ : (a) Systems with  $\phi \simeq 0.59$ , (b) Systems with  $\phi \simeq 0.68$ , (c) Systems with  $\phi \simeq 0.64$ .

## 4.7 Peak in non-Gaussian behaviour

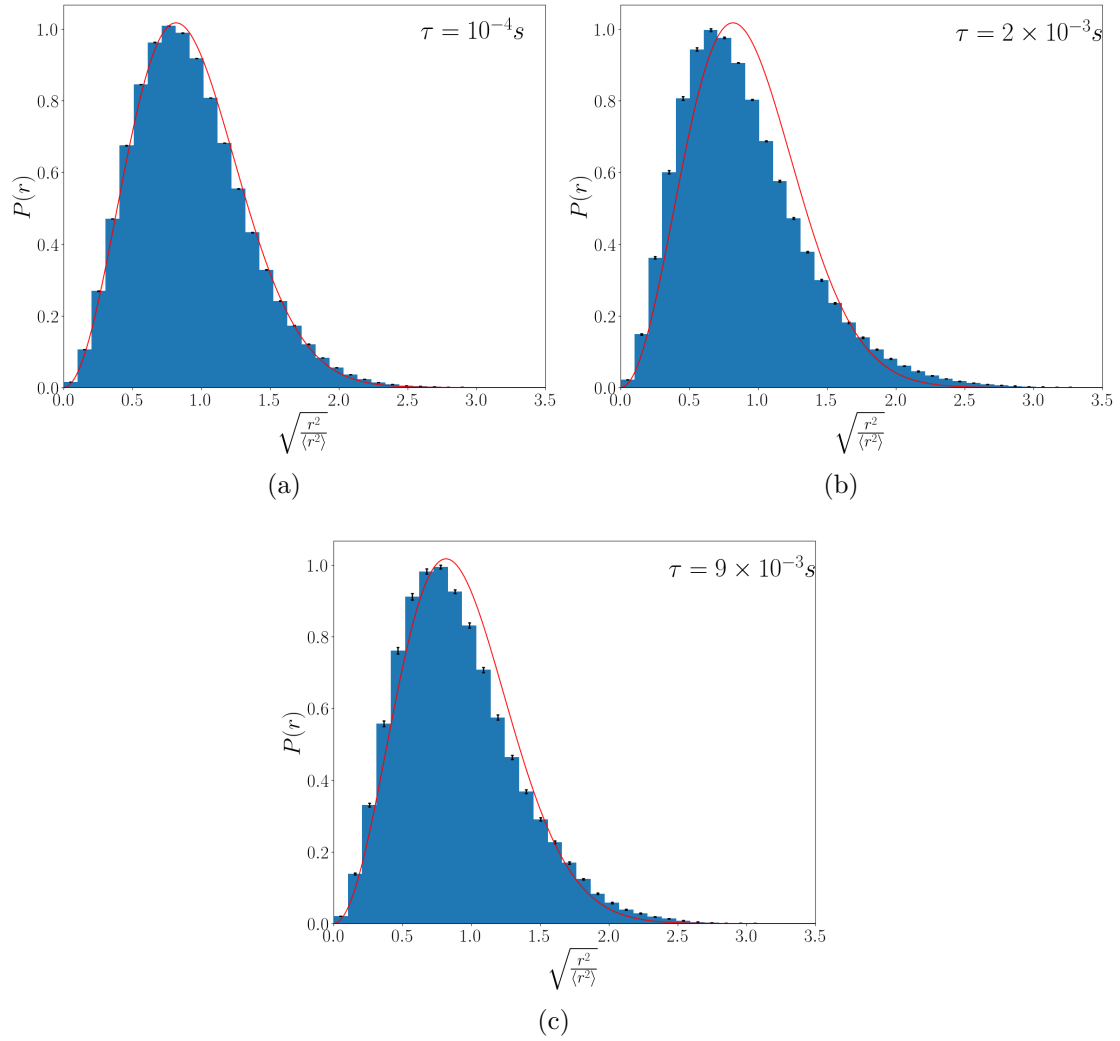


Figure 4.18: Histogram of displacements in units of RMSD for  $\zeta_e = 0.7$ ,  $K = 4\text{kPa}$  simulations for various timelags as denoted in the plots. Red line represents the PDF for a gaussian system with the MSD of this system.

## 4. QUIESCENT SIMULATIONS

---

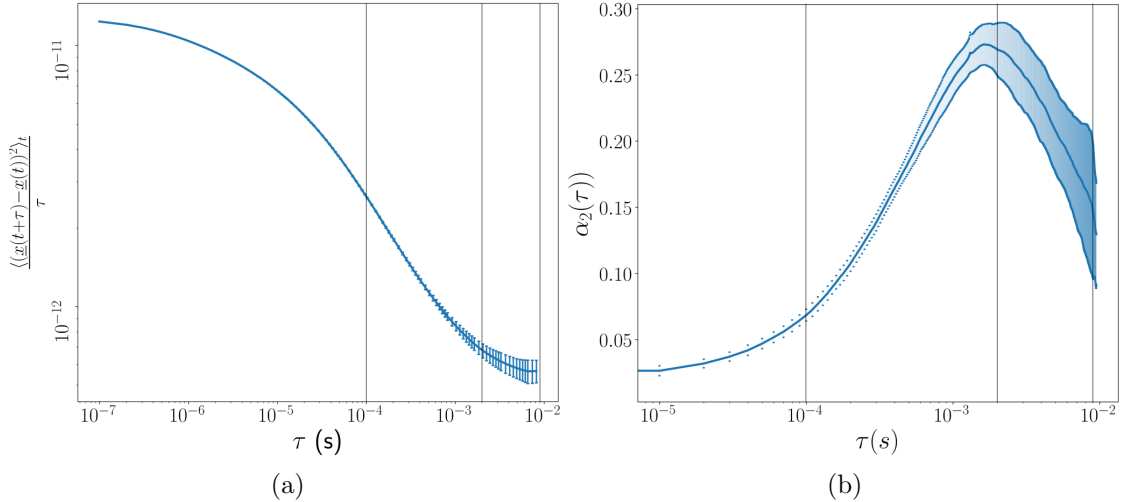


Figure 4.19: MSD divided by  $\tau$  and  $\alpha_2$  for  $\zeta_e = 0.7$ ,  $K = 4\text{kPa}$  simulations with timescales used for displacement histograms marked.

with the same MSD diffusing in three-dimensional space, given by:

$$P(r) = \frac{4\pi r^2}{\left(\frac{2}{3}\pi\langle r^2 \rangle\right)^{3/2}} e^{\frac{-r^2}{\frac{2}{3}\langle r^2 \rangle}} \quad (4.7)$$

We pick a single set of simulation parameters, as showing this data for all systems at a selection of timescales would be unfeasible in this format. A representative example is shown in [Figure 4.18](#) for  $\zeta_e = 0.7$ ,  $k = 4\text{kPa}$ . We can see on short timescales a very Gaussian behaviour, in which the histogram closely matches the Gaussian PDF. At later times, there is a shift away from Gaussian behaviour, approximately at the timescale of the second shoulder in the corresponding MSD. Finally, there is a partial return to Gaussian behaviour. We observe similar results in all simulations, though the largest deviation from Gaussianity depends on the simulation. Simulations with softer moduli do not shift as far away from Gaussian behaviour as the harder systems. Harder and more packed systems have a less

## 4.8 Correlation between particle deformation and motion

---

pronounced return to Gaussian behaviour at the lowest simulation times, which we would expect as these systems do not have as pronounced a return to a second diffusive regime. We expect that if simulations could be run for longer, eventually Gaussian behaviour would be observed.

## 4.8 Correlation between particle deformation and motion

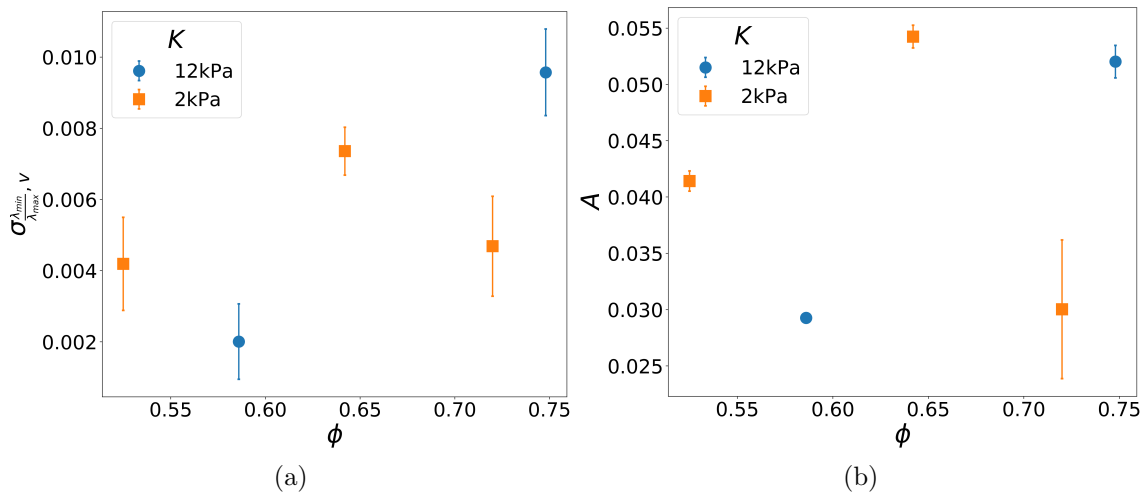


Figure 4.20: (a) Covariance of instantaneous velocity with ratio  $\frac{\lambda_{max}}{\lambda_{min}}$  of the shape tensor of the particle for a representative sample of simulations. (b) Measure of correlation of eigenvector corresponding to  $\lambda_{max}$  and instantaneous velocity.

Given that the simulated particles are able to alter their shape due to thermal fluctuations, we might expect that there is a correlation between particle deformation and particle motion, i.e. a deformed particle can more easily ‘break its cage’. Such behaviour could not be observed in simulations with radially symmetric particle interactions. As a simple attempt to see whether the shape of

#### 4. QUIESCENT SIMULATIONS

---

particles is correlated with their velocity, we have calculated two quantities for a representative set of simulations. We have been limited by time constraints and the computational expense of these calculations.

The first quantity calculated,  $\sigma_{\frac{\lambda_{max}}{\lambda_{min}},v}$  is the covariance between the average particle velocity,  $|v|$ , and the quantity  $\frac{\lambda_{max}}{\lambda_{min}}$ . The average velocity  $\underline{v}_i$  for a particular checkpoint  $i$  is given by a central difference:

$$\underline{v} = \frac{\underline{x}_{i+1} - \underline{x}_{i-1}}{2\Delta t} \quad (4.8)$$

where  $\underline{x}_i$  is the displacement of the centre of mass of the particle at checkpoint  $i$ , and  $\Delta t$  is the time between checkpoint output. The value  $\frac{\lambda_{max}}{\lambda_{min}}$  is the ratio of the largest and smallest eigenvalues of the shape tensor, which is given for a finite element simulation by:

$$\mathbf{S} = \left[ \frac{1}{M} \sum_e m_e \mathbf{Y}_e \right] - \underline{X}_c \otimes \underline{X}_c, \quad (4.9)$$

where  $M$  is the mass of the colloid, subscript  $e$  denotes elements,  $m_e$  is the mass of element  $e$ ,  $\otimes$  is the outer product,  $\underline{X}_c$  is the centre of mass of the colloid and  $\mathbf{Y}_e$  is given by

$$\mathbf{Y}_e = \frac{1}{20} \left( \sum_i \sum_j \underline{X}_i \otimes \underline{X}_j + \sum_i \underline{X}_i \otimes \underline{X}_i \right) \quad (4.10)$$

where indices  $i, j$  denote nodes in the element.

The eigenvalues of this shape tensor correspond to the semi-axes of an ellipsoid: each eigenvalue is  $\frac{1}{5}a^2$ , where  $a$  is the relevant semi-axis. The ratio  $\frac{\lambda_{max}}{\lambda_{min}}$  then gives us a rough measure of how distended the particle is. The covariance

## 4.8 Correlation between particle deformation and motion

---

is averaged over all particles on all checkpoints output over all realisations of a system. This measure investigates whether colloids that are more deformed than average move faster than average.

Our second measure again uses the eigenvalues and eigenvectors of the shape tensor. For this measure, we calculate the quantity:

$$A = 3 \frac{\langle (\underline{e}_{i,\alpha} \cdot \underline{v}_{i,\alpha})^2 \rangle_{i,\alpha}}{\langle \underline{v}_{i,\alpha} \cdot \underline{v}_{i,\alpha} \rangle_{i,\alpha}} - 1 \quad (4.11)$$

where  $\underline{e}_i$  is the eigenvector of the largest eigenvalue of the shape tensor for particle  $\alpha$  at frame  $i$ , and  $\underline{v}_{i,\alpha}$  is the central difference of the velocity for particle  $\alpha$  at frame  $i$ . This is averaged over all particles on all checkpoints output over all instances of a system with a particular set of parameters. This quantity measures whether particles tend to move in the direction of their largest semi-axis. We have  $A > 0$  if  $\underline{v}_{i,\alpha}$  tends to be directed along  $\underline{e}_{i,\alpha}$ , but zero if  $\underline{v}_{i,\alpha}$  is isotropic.

While we can see in [Figure 4.20](#) that neither of these measures suggest a strong correlation between particle deformation and motion of the centre of mass of the colloid, they are both consistently positively correlated in all the simulations we have analysed. They also both appear to peak at  $\zeta_e = 0.8$  for both measures for the 2kPa simulations, though with the paucity of information we have here this conclusion can be drawn only weakly. It is interesting to note that we have a slight positive correlation in both measures. The covariance measures whether colloids more deformed than average move faster than average, whilst the second measure simply checks whether particles tend to move in the direction of the eigenvector with the largest eigenvalue. In this latter measure the particles do not need to be more deformed than the average. It is interesting both of these

## 4. QUIESCENT SIMULATIONS

---

measures should give a positive result.

A weakness of the approach we take here is that we have only approached the analysis through post-processing. As a result, the velocity we are using is averaged over a significant timescale rather than being instantaneous, whilst we can only calculate an instantaneous value of the asphericity of the particles, and these quantities may not be correspondingly representative of motion and deformation in that period, given the lack of inertia in the simulations. If we were to repeat this analysis, we might compute the asphericity as a rolling average on the fly during simulations, with a similar window as the velocity. It might be interesting in further work also to see if there are sub-populations of faster moving particles that behave differently with regards to shape, rather than averaging overall populations. [Gnan & Zaccarelli \(2019\)](#) study an asphericity parameter for motion of rings in two dimensions, and while their work is two dimensional and the asphericity measures are not directly comparable, they find that the rings with largest asphericity are not the fastest rings, and also that there are significant differences in behaviour of sub-populations.

### 4.9 Stress correlator

We calculate a correlation function for the deviatoric stress. The stress tensor for the simulation is calculated as described in [section 3.3](#) and the correlation function is calculated as described in [subsection 3.4.2](#). To remind the reader, the

## 4.9 Stress correlator

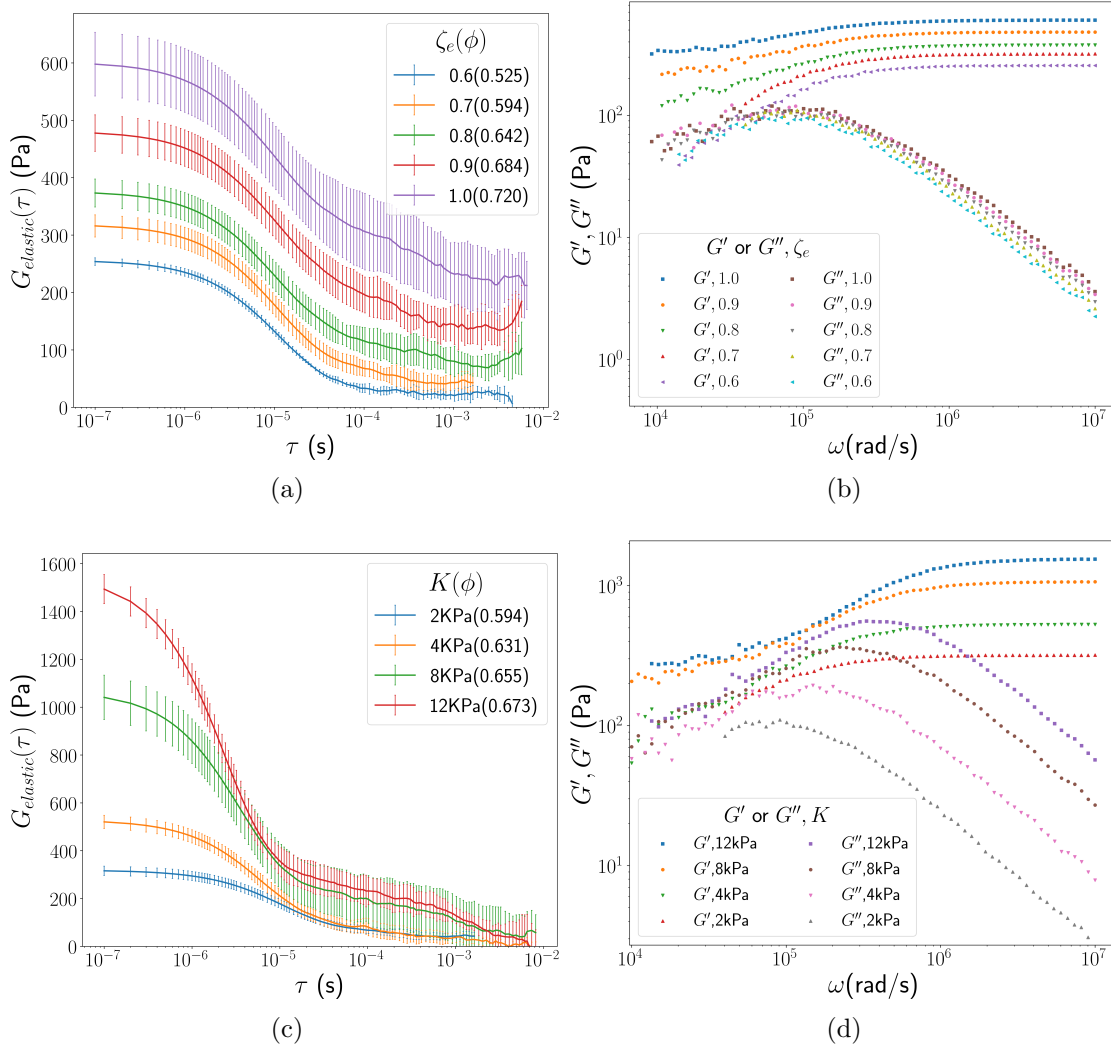


Figure 4.21: Stress correlation function against time lag  $\tau$  and i-Rheo (Tassieri *et al.*, 2018) converter embedded in RepTate (Boudara *et al.*, 2020) deconvolution of  $G'$ ,  $G''$  for (a) 2kPa varied  $\zeta_e$ , (b)  $G'$ ,  $G''$  generated using data from a, (c) Varied moduli,  $\zeta_e = 0.7$ , (d)  $G'$ ,  $G''$  generated using data from c.

## 4. QUIESCENT SIMULATIONS

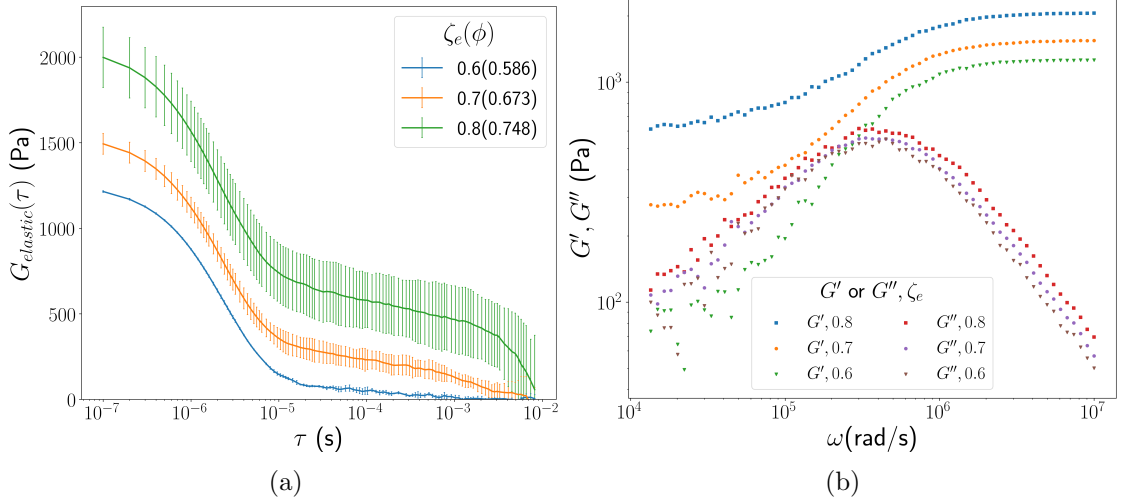


Figure 4.22: Stress correlation function against time lag  $\tau$  and i-Rheo (Tassieri *et al.*, 2018) converter embedded in RepTate (Boudara *et al.*, 2020) deconvolution of  $G'$ ,  $G''$  for (a) 12kPa varied  $\zeta_e$ , (b)  $G'$ ,  $G''$  generated using data from **a**.

correlation function calculated is:

$$G(\tau) = \frac{V}{5k_bT} [\langle \sigma_{xy}(\tau)\sigma_{xy}(0) \rangle + \langle \sigma_{yz}(\tau)\sigma_{yz}(0) \rangle + \langle \sigma_{zx}(\tau)\sigma_{zx}(0) \rangle] + \frac{V}{30k_bT} [\langle N_{xy}(\tau)N_{xy}(0) \rangle + \langle N_{yz}(\tau)N_{yz}(0) \rangle + \langle N_{xz}(\tau)N_{xz}(0) \rangle] \quad (4.12)$$

where  $\sigma_{\alpha\beta}$  denotes a component of the stress tensor for the system,  $N_{\alpha\beta} = \sigma_{\alpha\alpha} - \sigma_{\beta\beta}$  correspond to normal stress differences,  $V$  is volume and  $T$  is temperature. This considers correlations of the deviatoric stress, i.e. stress related to changes of particle shape, as opposed to changes in particle volume, which relate to pressure.

For a liquid system that has a single characteristic timescale for relaxation, we would expect  $G(\tau)$  to reach zero beyond that timescale. We would further expect, for systems that establish a second diffusive regime in MSD, that this ability to rearrange particles would also allow them to completely relax the stress, i.e. we expect  $G(\tau) \rightarrow 0$  as the second diffusive regime is established. We can see from

Figure 4.21 and Figure 4.22 that this has only happened in a few simulations on the timescales that we are currently able to reach. In this Figure, we show the total elastic  $G(\tau)$ , left. We also show the storage and loss moduli,  $G', G''$  as a function of frequency as obtained using the i-Rheo (Tassieri *et al.*, 2018) converter embedded within RepTate (Boudara *et al.*, 2020).

We can see from these plots that we have a characteristic shape in all simulations with a first decay at short timescales, and a slowly relaxing decay at long timescales. We attribute the short timescale relaxation to the relaxation of individual particle stresses, which we evidence by considering the timescale over which we would expect this relaxation, given by  $\tau_{Particle} = \frac{\zeta_{Particle}}{G_{Particle}}$ , and find rough agreement for the timescale of relaxation. From this ratio, we would also expect that particles with higher modulus would perform this initial decay more rapidly, which we also observe. This also corresponds roughly to the timescale where the MSD goes from the initial diffusive to the plateau regime. The long timescale relaxation we then attribute to structural stress arising from particle-particle interactions. In many simulations this does not relax entirely. These typical relaxation times depend on the choice of parameters in manners we shall now discuss.

We can observe in Figure 4.21 that the stress component from individual particle stresses increases with particle modulus, but is not strongly varying with  $\zeta_e$  or  $\phi$ , i.e. there is a consistent surplus above the structural stress. Again, the short-term relaxation time decreases as modulus increases. For the long timescale stress, we can see from a representative example in Figure 4.23 that there is a consistent shape and rate of relaxation of structural stress across different instances of the same parameter, suggesting that there is a dependence of the autocorre-

## 4. QUIESCENT SIMULATIONS

---

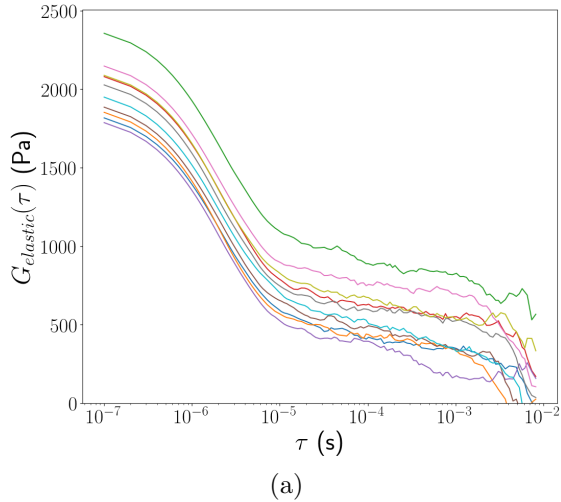


Figure 4.23: Output of stress correlation function against time lag  $\tau$  for all instances of simulation at  $\zeta_e = 0.8, K = 12\text{kPa}$ .

lation of the structural stress on the initial configuration. This manifests as a constant error for the plots on all regimes, as they can all only relax differing amounts of structural stress in different configurations at the same rate. As a general trend, we can also see that increasing packing at a fixed particle modulus increases the long term structural modulus, and likely results in a slower rate of relaxation of that modulus.

We now turn our attention to simulations with similar  $\phi$  where other values are varied, shown in [Figure 4.24](#). While the individual particle moduli are, as expected, quite different, the long term structural modulus seems much more similar for simulations with similar  $\phi$ . A larger value of  $\phi$  here corresponds to a larger intermediate value of the modulus, even for particles with higher modulus. In this case the simulations in [Figure 4.24c](#) are ordered relative to  $\phi$ , which was not true for their MSD.

Given this observation, we now plot in [Figure 4.25](#) the moduli of these sys-

## 4.9 Stress correlator

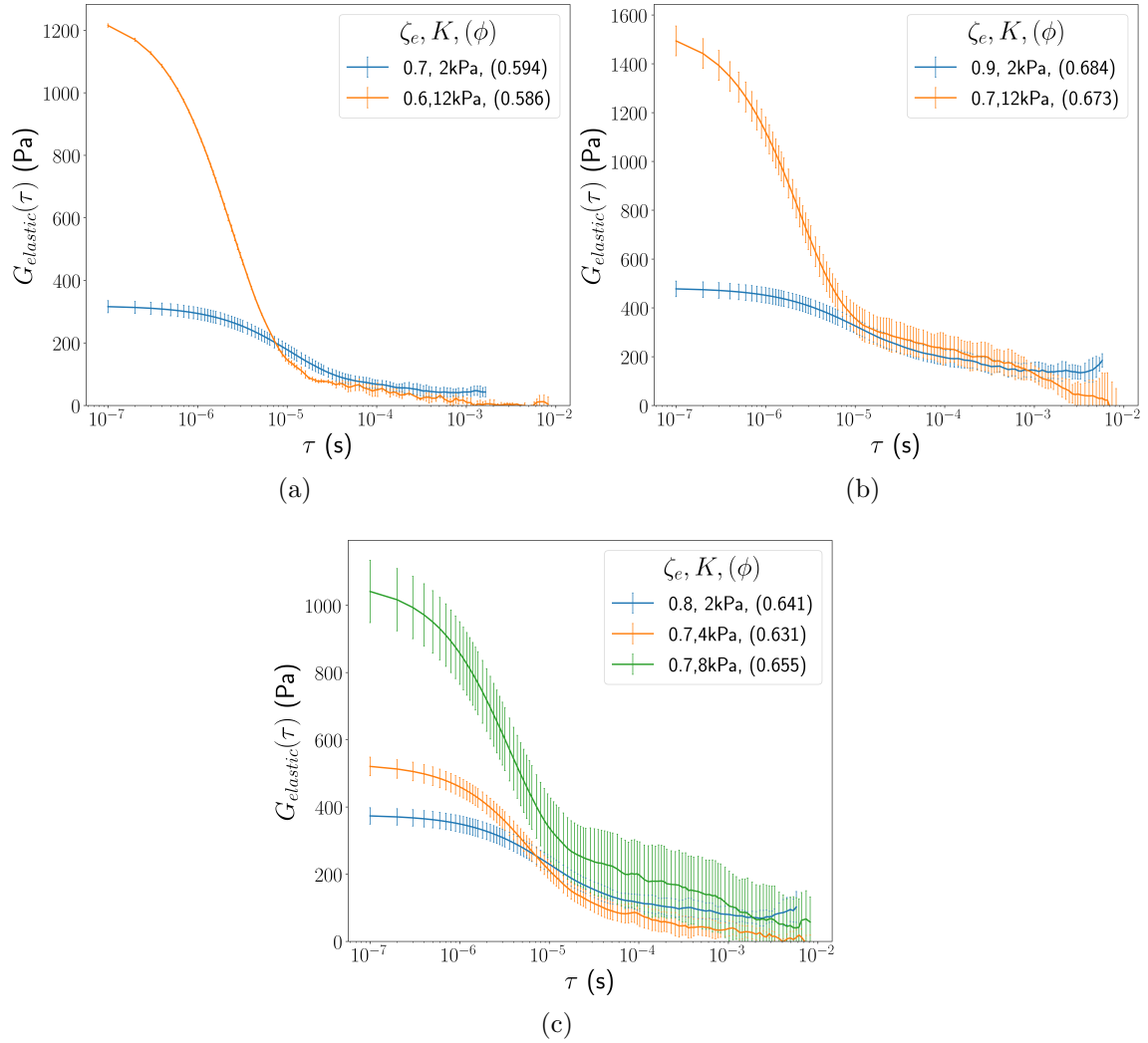


Figure 4.24: Comparisons of deviatoric stress correlation functions for systems with similar  $\phi$ .

## 4. QUIESCENT SIMULATIONS

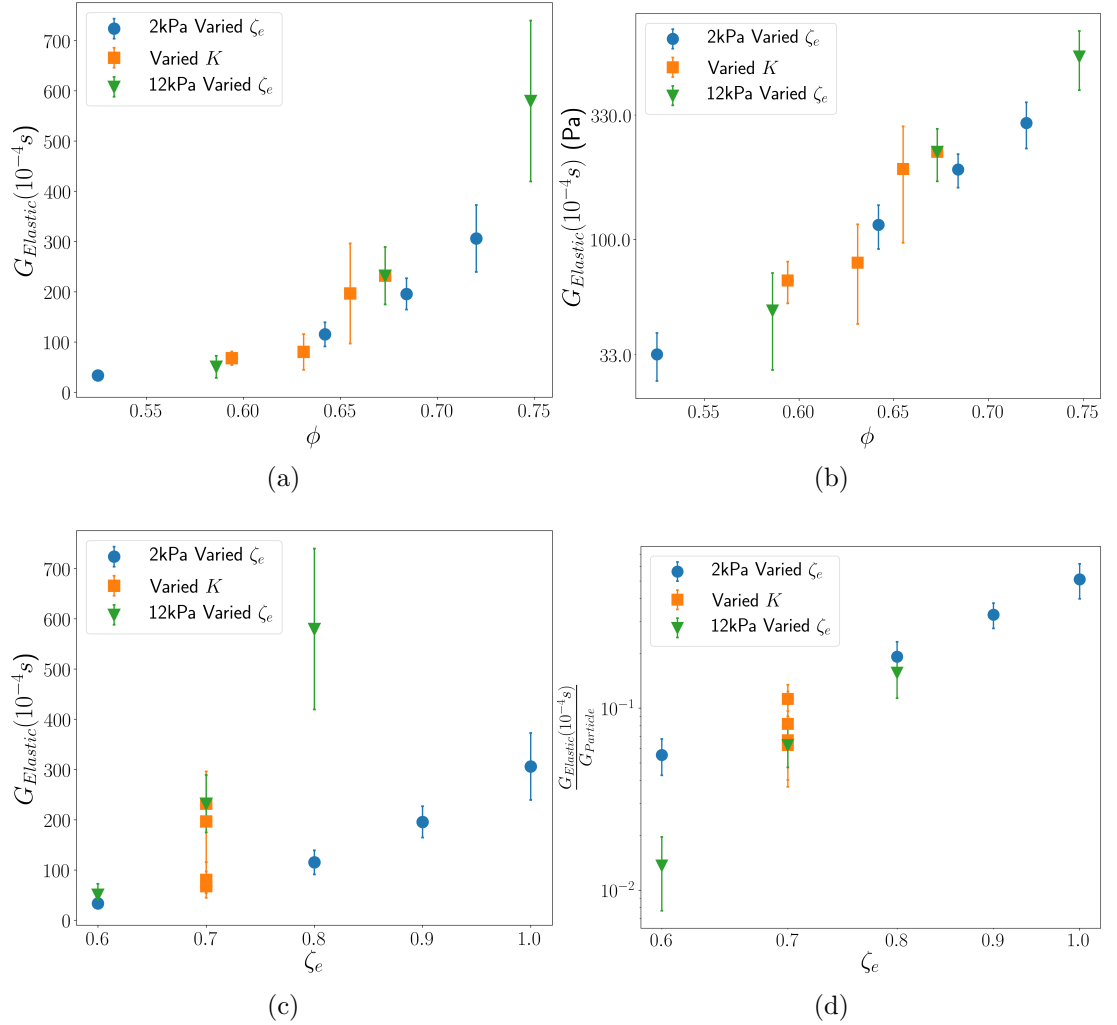


Figure 4.25: Comparisons of deviatoric stress correlation functions at intermediate value of  $10^{-4}$  s versus (a) volume fraction  $\phi$ , linear scaled, (b)  $\phi$ , log scaled in  $G_{Elastic}$ , (c) effective volume fraction  $\zeta_e$ , (d)  $\zeta_e$ , with  $G_{Elastic}$  scaled by  $\frac{1}{G_{Particle}}$ , log scaled in  $\frac{G_{Elastic}}{G_{Particle}}$ .

tems observed at a typical intermediate timescale of  $10^{-4}$ s to investigate the dependence of the structural modulus on relevant parameters. We can see from [Figure 4.25a](#) and [Figure 4.25b](#) that there is a clear dependence of the structural modulus of our systems at intermediate timescale on  $\phi$ , that is not true for  $\zeta_e$  in [Figure 4.25c](#). It is a curious result the long time modulus appears to depend on  $\phi$  independently of  $G_{Particle}$ , as  $G_{Elastic}$  has units of Pa, whilst  $\phi$  is dimensionless. We therefore normalise by  $G_{Particle}$  in [Figure 4.25d](#), as a candidate modulus for scaling, but as we can see this does not scale the systems well at low  $\zeta_e$ , though it appears to collapse better as  $\zeta_e$  increases, though simulations with higher modulus at higher  $\zeta_e$  would be necessary to confirm this. Without thermal fluctuations, we would expect  $\phi$  to be a unique function of  $\zeta_e$ , especially as we disallow large overlaps. As the thermal fluctuations allow for substantial shape changes (as discussed in [subsection 3.1.1](#)), especially in the softest particles, these simulations can reach better packed states, there is no longer a unique relationship between  $\phi$  and  $\zeta_e$ . One further combination of parameters with dimensions of modulus is the ratio  $\frac{k_B T}{V_{Particle}}$ . It is possible that there is a relationship similar to  $G(10^{-4}s) = \frac{k_B T}{V_{Particle}} \frac{1}{1-k\phi}$ , where  $k$  is some constant. In this scenario,  $(1 - k\phi)$  represents a measure of free volume per particle, rather than simple volume per particle. This has a modulus arising from an entropic argument - that there is some amount of space for the particle to ‘rattle’ in its cage. As hardness increases, the space in which which the colloid can rattle decreases, working against entropy and increasing the modulus. This scaling, in the limit of infinite hardness, would also need to map back onto hard sphere behaviour, as the modulus in hard sphere systems arises entirely from entropic arguments ([Petekidis \*et al.\*, 2004](#)). Finally, it is possible that the long time modulus could depend on a combination of mul-

## 4. QUIESCENT SIMULATIONS

multiple different dimensionless groups, or another effective modulus that we have overlooked. There may be a transition from an entropy dominated stress to a modulus dominated one when the system is more constrained at high volume fraction. Additionally, the monodisperse nature of our systems perhaps makes these effects stronger than they would be for polydisperse systems, which can pack in different ways to monodisperse systems. Ultimately, the results are so far not conclusive, and would need targeted exploration to elucidate, exploring higher volume fractions at higher moduli, and whether all moduli still collapse onto the same trend.

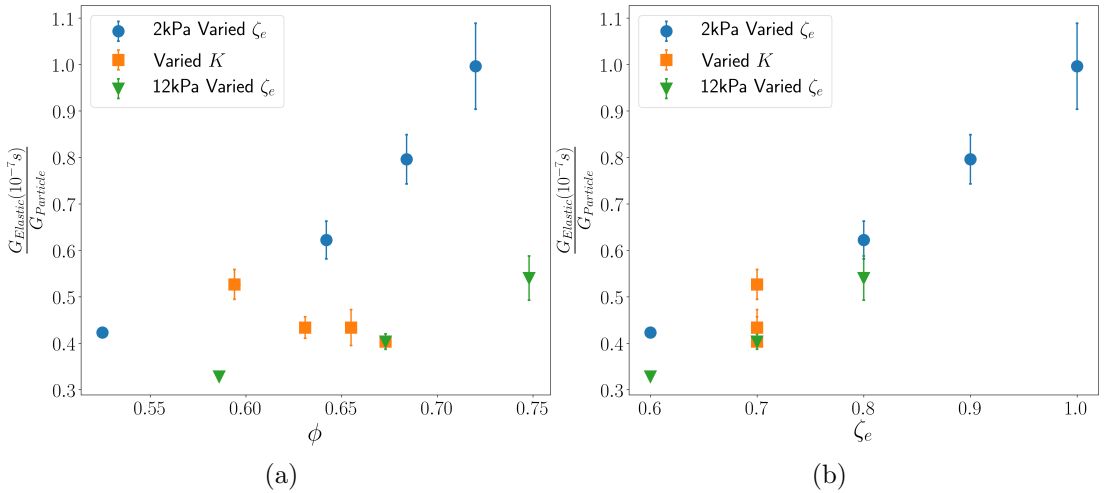


Figure 4.26: Comparisons of deviatoric stress correlation functions at short timescale of  $10^{-7}$ s normalised by  $\frac{1}{G_{Particle}}$  versus (a) volume fraction  $\phi$ , (b) effective volume fraction  $\zeta_e$ .

Taking the short timescale values of  $G_{Elastic}$  normalised by  $\frac{1}{G_{Particle}}$  plotted in Figure 4.26, we can see that this collapses to some extent against  $\zeta_e$ , but does not collapse for  $\phi$ , confirming the early decay does arise from individual particle stresses. We should note though that these short time moduli do vary with  $\phi$  even

at fixed  $\zeta_e$ , indicating that while the initial decay arises from the decay of individual particles stresses and therefore corresponds to individual particle moduli, the short time value depends on the structural stress as well. We might expect the short time modulus to set cage-breaking times for our system, as cage-breaks would be fast events, even if they enable relaxation of stress on longer timescales. Relating this to the MSD, neither the short time nor long time modulus appear entirely consistent with setting the cage-breaking time, as both are dependent on the structural stress which varies significantly between simulated instances of each set of parameters, while MSD and  $\phi$  both vary little across instances. However, cage-breaking clearly must involve particle deformation, and must therefore be dependent on the particle modulus.

The work of [van der Scheer \*et al.\* \(2017\)](#) may be relevant here, as they present a simple model that nonlinearly relates  $\zeta_e$  and  $\phi$ , through osmotic deswelling. The degree of nonlinearity depends only on the elastic energy per particle which scales inversely with particle volume. However, as can be seen in [section 4.5](#), the dynamics of the system are not set by the true value of  $\phi$ , so this or a similar model would not account for all the behaviour we observe.

This result is significant in two important aspects. Firstly, only methods of simulation that take into account anisotropic deformation could probe this behaviour. Secondly, this result directly relates microscopic dynamics and structure to a macroscopic quantity. Hertzian soft spheres such as [Bonnecaze \*et al.\* \(2020\)](#) cannot relate these quantities in this way, as the stress calculation arises simply from Hertzian deformation and does not fully address multiple contacts, although the dynamics of the systems in that paper do follow from excess entropy and confinement. Similarly, approaches such as Brownian dynamics only

## 4. QUIESCENT SIMULATIONS

---

take into account thermal stress and distance between two particles (Zia *et al.*, 2014).

### 4.10 Conclusion

In this chapter, we have presented quiescent simulation results showing rearrangements in all simulations at all effective volume fractions and material parameters attempted, and the tendency towards a second diffusive regime between cages in all cases. We have discussed the relationship between observed volume fraction and effective volume fraction, showing that even at the limit of  $\phi$  for monodisperse hard spheres, we still witness rearrangement. We have found no evidence of long-range ordering in our soft colloidal systems, but we have some agreement with sub-glassy hard sphere theory in structure of our higher moduli systems and some short-range HCP ordering. We have shown that MSD results are consistent with (if not wholly conclusive in isolation) all systems approaching a cage breaking diffusive regime, as well as demonstrating that MSD behaviour is not dominated by  $\phi$ . We have demonstrated that there is a rise, peak and fall in non-Gaussian behaviour, consistent with an approach to a cage-breaking regime. We have made a limited investigation of correlations between particle shape and motion, but have concluded that more targeted work would need to be done to reach more substantial conclusions. Investigating the stress autocorrelation function, we find a superposition of intra-particle and structural deviatoric stresses, and observe that the structural stress scales with  $\phi$ , in opposition to the MSD, and conduct a preliminary discussion of the cause.

While simulations with spherically symmetric potentials may include thermal

noise acting on each particle, this generally results in systems that are athermal, as these simplistic potentials can only produce sensible results when considering particles that are relatively stiff compared to those simulated in this work. Alongside this, if we simulated only the response to the deformation and compression of particles, without thermally driven shape fluctuations, the system would eventually reach an equilibrium configuration. This would also have resulted in a different, single equilibrium structure per simulation, possibly crystalline due to the monodisperse particles, rather than the structural behaviours recovered. Alongside the evidence of a second diffusive regime, this shows that the simulation of thermal fluctuations resulting in deformation is a key component of the novelty of this work.

## 4. QUIESCENT SIMULATIONS

---

# Chapter 5

## Experimental Rheology

In this chapter I describe experimental measurements on microgel colloids conducted at École supérieure de physique et de chimie industrielles de la Ville de Paris (ESPCI Paris) Matière Molle et Chimie (MMC, Soft Matter and Chemistry) lab, under the supervision of Dr. Michel Cloitre during a secondment as part of my studies. These measurements were performed on a set of microgels with very low crosslink density which [Mattiello \(2018\)](#) proposed as a new class of soft microgels, referred to as ultrasoft microgels. The least densely crosslinked microgels studied display qualitatively different behaviour than most soft microgels, and in some ways are much more similar to star polymers ([Likos \*et al.\*, 1998](#); [Singh \*et al.\*, 2011, 2013](#)).

For most soft colloids, two distinct regimes of glassy behaviour can be observed; entropic glass near the liquid-solid transition, and a jammed glass regime at higher concentrations. In the entropic glass regime, dynamics are controlled by kinetic arrest of the particles. The particles are caged, but are not yet in continuous contact. This caging gives rise to entropic elasticity, which at maximum

## 5. EXPERIMENTAL RHEOLOGY

---

reaches  $100k_B T$  for hard spheres (Petekidis *et al.*, 2004), and does not scale with concentration. This can be seen in the first regime of Figure 5.1a. The onset of the jammed glass regime occurs only in highly packed soft colloidal systems, where suspension elasticity arises from elastic contacts between particles due to deformation. The rheological properties of the jammed regime exhibit linear scaling of the elastic modulus with concentration as can be seen in the second regime of Figure 5.1a, and are not influenced by temperature. The yield strain,  $\gamma_y$  increases with concentration, due to rearrangement and yielding being more challenging with greater crowding. For most soft particles, we would expect a discontinuity in  $G_0$ , the low-frequency modulus, which can be seen in Figure 5.1a and Figure 5.1c, and in experimental studies such as Pellet & Cloitre (2016). This quantity is approximated by taking the value of  $G'$  at the minimum of  $G''$  in a frequency sweep. Flow curves (discussed in subsection 5.3.2) for the jammed regime can be collapsed onto a master curve with the stress scaled by  $\frac{1}{\sigma_y}$  and shear rate by characteristic time  $\frac{\eta_s}{G_0}$ . These behaviours have been qualitatively reproduced in simulations (Mohan *et al.*, 2013; Seth *et al.*, 2011).

For ultrasoft microgels, entropic and jammed glass regimes cannot be distinguished, with the elastic modulus increasing across the liquid-solid regime in a way that does not correspond to either standard regime, as can be seen in Figure 5.1. This behaviour is discussed for star polymers in Erwin *et al.* (2010). The yield strain does not depend on concentration, suggesting that crowding effects are not dominant in the way particles escape their cage under strain, compared to standard soft colloids. Additionally, the yield point is frequency dependent, so if the microgels have more time to deform, they yield at lower deformation. As a consequence the dependence on the time scale  $\frac{\eta_s}{G_0}$  is not found, with scaling

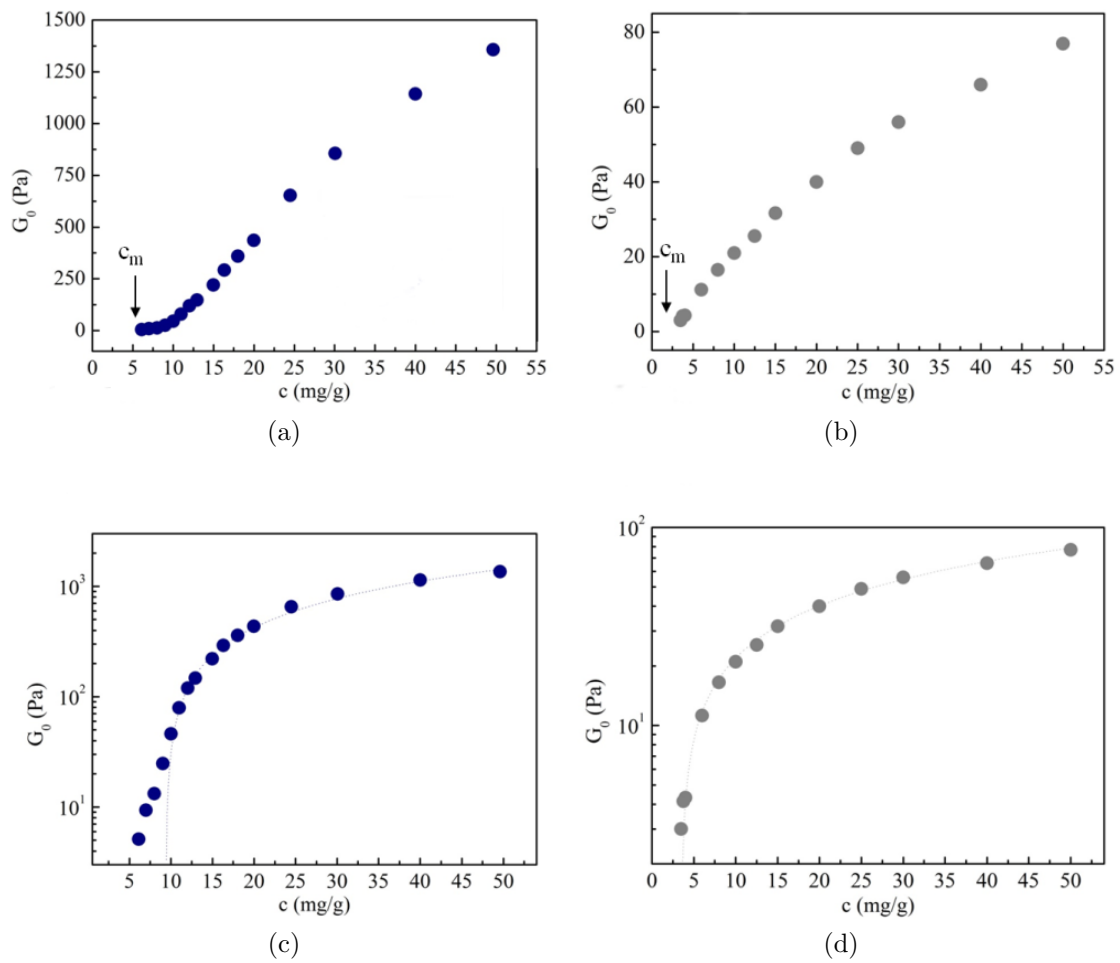


Figure 5.1: Variation of elastic modulus  $G_0$  with concentration for lin-lin plots of (a) Standard soft colloid, (b) Ultrasoft colloid and the same data on log-lin plots for (c) and (d). Plots and data from [Mattiello \(2018\)](#).

## 5. EXPERIMENTAL RHEOLOGY

---

onto a master curve only requiring the  $\sigma_y$  correction. [Mattiello \(2018\)](#) posit that the extreme softness of their particles allows deformation and yielding without the energetically costly deformation of the cage, and that they have the capability of self-squeezing for rearrangement. To the best of the author’s knowledge, rearrangement attributes have only previously been reproduced through simulation with techniques that represent and directly simulate particle deformation or compressibility ([Gnan & Zaccarelli, 2019](#); [Lo Verso \*et al.\*, 2016](#); [Zakhari \*et al.\*, 2018](#)), and the indistinguishable regimes have not been reproduced. We discuss the synthesis and preparation of these microgels in [section 5.1](#).

We therefore conducted an experimental investigation of the ultrasoft microgels, to confirm this behaviour and compare them to our simulation results, which are discussed in [Chapter 6](#), with the practical experimental results discussed in isolation here.

In the following sections, we discuss the microgels themselves and how they are prepared, and tested for the presence of free chains of polymer which could distort the results. Once this is excluded, we move onto steady state and oscillatory rheology, and discuss differences between specific syntheses of microgels, the possibility of aging behaviour where rheological responses could change over time, and to what extent the results obtained are consistent with behaviours of [Erwin \*et al.\* \(2010\)](#); [Mattiello \(2018\)](#).

## 5.1 Microgels

### 5.1.1 Material

The French company *Coatex Sas*, a subsidiary of the Arkema group, supplied the microgels used in these experiments to MMC. A non-disclosure agreement relates to MMC's collaboration with the synthesising company, and some details of the synthesis are omitted.

These microgels were synthesised using starved-fed direct emulsion polymerisation. They are polymer networks, smaller than  $1\mu\text{m}$ , made of a copolymer of Ethyl-Acrylate (EA) and Methacrylic Acid (MAA). These copolymers are cross-linked using Trimethylpropane Triacrylate (TMPTA). The reaction occurs in a micellar dispersion of surfactants and microdroplets of monomer, with water as the continuous phase. The initiator is a hydrophilic module added to the continuous phase, which decomposes and forms radicals on monomers that migrate to the surfactant micelles. The micelles act as the site for polymerisation. To better control the microgel growth, only a small amount of reagent is initially put in the reactor, with further reagent added slowly and steadily during the course of the reaction. This is to allow for finer control of the composition of the polymer network, and to create a more uniform, more sparse distribution of crosslinks within microgels to ensure softness (Acciario *et al.*, 2011; Still *et al.*, 2013). This is in contrast to the more widely used precipitation polymerisation commonly used in Poly(N-isopropylacrylamide) (pNIPAM) synthesis, which produces a structure with a denser core and less dense outer layers (Fernandez-Nieves *et al.*, 2011; Romeo & Ciamarra, 2013; Scheffold *et al.*, 2010; Stieger *et al.*, 2004).

This synthesis process yields a highly concentrated colloidal suspension of the

## 5. EXPERIMENTAL RHEOLOGY

---

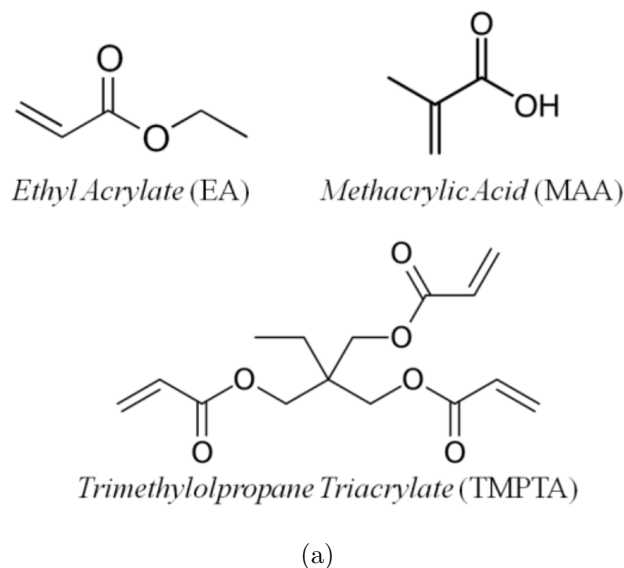


Figure 5.2: Constituent monomers of the microgel polymer network. Above, the two monomers EA and MAA, and below the crosslinker TMPTA. Figure from [Mattiello \(2018\)](#).

gels of approx. 30wt%, verified both by the supplying company and by [Mattiello \(2018\)](#). These suspensions will be referred to as stock solutions. The copolymer is hydrophobic and the backbone is not charged, so the microgels do not swell in pure water. Adding a salt to ionise the acidic functions of MAA generates counter ions that increase the osmotic pressure in the microgel, causing an influx of water into the microgel that leads to swelling. As the water swells these particles, it can also be expelled, meaning these particles are compressible and deformable. As the swelled state is their preferred state, they also have material modulus, and have viscoelastic properties.

As these microgels are extremely soft, have an amount of polydispersity, and are a swollen network rather than a continuous particle, it is difficult to determine a volume fraction. For this reason we vary weight concentration, which will be a

related variable to volume fraction.

For the rheological experiments included here, we use a single, loosely crosslinked example of this type of microgel. As shown by [Mattiello \(2018\)](#) the amount of crosslinker reagent affects crosslink density and therefore softness, as well as changing the general profile of the rheological response. The chemical make up of this sample as described is 59.68% EA, 40.22% MAA and 0.20% TMPTA. We measured the rheological behaviour of two batches of microgels synthesised by *Coatex Sas*, noted as Batch 1 and 2 in results. Batch 1 is used in the work of [Mattiello \(2018\)](#), and Batch 2 is a newer batch following identical synthesis and preparation procedures. The differences between these two batches will be discussed in [subsection 5.4.1](#).

### 5.1.2 Sample preparation

To prepare the sample, the first step is to dilute the original stock solution in a flask with half the volume of the deionised water necessary to reach the required dilution. The required amount of NaOH is mixed with the remaining half of the deionised water in second flask, to ionise the MAA functions. The second flask is poured into the first while the first is tilted and rotated, to ensure the solutions are well mixed. To rid the sample of air bubbles, the sample is placed on a shaker for at least 24 hours, prior to centrifugation at 8000 RPM for 5 minutes to remove bubbles, with temperature at 25°C in a TA10-4-50t rotor.

The amount of NaOH is chosen so that the ionisation ratio, defined as:

$$\alpha = \frac{[NaOH]}{[-COOH]}, \quad (5.1)$$

## 5. EXPERIMENTAL RHEOLOGY

---

where  $[NaOH]$  is the molar amount of NaOH added to achieve ionisation and  $[-COOH]$  the molar amount of acid functions in the microgels, is equal to one as this results in maximal swelling (Mattiello, 2018). The measured microgel radius is approximately  $335 \pm 12 \text{ nm}$  for Batch 1 as shown in the work of Mattiello (2018), and  $240 \pm 10 \text{ nm}$  for batch 2, measured by another member of the laboratory.

### 5.2 Free chains

To test for the presence of free chains of polymer after synthesis, we used Static Light Scattering (SLS) and thermogravimetry. This was necessary to ensure that rheological results are purely due to the nature of the microgels, and are not influenced by free-chains interacting with or between microgels, or with other free-chains, which might give more complicated polymer entanglement behaviour.

Due to the homogeneous crosslinking of this microgel, Mattiello (2018) estimates the free chain length at the edges as  $10 \text{ nm}$ , which is too short for interdigitation. This quantity was calculated by assuming a uniform distribution of the crosslink density in the polymer network, the hydrodynamic radius obtained from Light Scattering experiments, and the number of monomer units between crosslinks.

#### 5.2.1 Sample preparation

Before performing Static light scattering or thermogravimetric analysis, we microfiltered a low wt% sample to filter out the microgels, which would be swollen, leaving only objects significantly smaller or capable of presenting a much smaller aspect in the suspension, such as free polymer chains. To prepare the samples for

analysis, a 0.1wt% suspension of microgels was prepared as described in [subsection 5.1.2](#), except using filtered deionised water. This was run through a 10kDa microfilter while being stirred and pressurised, and three 3-4ml samples taken of the product using a pipette, and transferred directly into a clean cylindrical light scattering sample tube and sealed. The filtration was then repeated on the product and 3 more samples taken in the same manner. The outside of the sealed tube was then cleaned again using ethanol, directly before being placed into the sample chamber.

### 5.2.2 Static Light Scattering

Static light scattering in the dilute regime was performed with an ALV/CGS-3 Compact Goniometer System combined with a He-Ne laser with  $\lambda = 632.8\text{nm}$ . The scattered intensity was collected by two photomultipliers, located on a goniometer that can span scattering angles between  $20^\circ$  and  $150^\circ$  with respect to the direction of the incident beam. The temperature of the measuring cell was kept constant by a thermostatic bath at  $20^\circ\text{C}$ . We took the mean of three 60 second measurements every  $10^\circ$  from  $30^\circ$  to  $150^\circ$  for all samples.

Samples taken as described in [subsection 5.2.1](#) are first compared to reference values for a sample tube containing only filtered deionised water, and the count rate of these was subtracted. Next, a sample containing the unfiltered suspension of microgels is analysed. For this and the filtered samples, the measurement  $\frac{CR}{I}$  was taken. Here,  $CR$  is the count rate, the number count of photons scattered towards the detector by the scattering objects in a second, and  $I$  is the intensity. Comparing the ratio of this value for filtered and unfiltered measurements gives us

## 5. EXPERIMENTAL RHEOLOGY

---

an approximation of the relative amount of matter in the sample. The maximum value of this ratio for sample SLS measurements across all samples and angles measured was 0.007. This indicates that free chain content in these systems is within experimental error of zero, and therefore negligible or non-existent.

### 5.2.3 Thermogravimetry

To corroborate the SLS, thermogravimetric analysis was performed on two of the samples after performing light scattering. This analysis allows us to weigh the solid content of our sample, removing the solvent. Performing this on the filtered sample will allow us to measure the mass of the free chain content of the sample, if it exists. A metal sample tray with a weighing paper was placed in a thermogravimetric device. This device was calibrated by raising the temperature to 120° C, ensuring the moisture content was removed from the weighing paper; the scale of the device was then zeroed. Approximately 2g of sample was soaked into the paper at room temperature, and the temperature was increased to 120°C until the measured mass stabilised. The mass measured at this point should be the mass of the free-chain content, as the suspending medium should have evaporated. The remaining mass after evaporation from thermogravimetry was within the experimental error of zero, again indicating that free-chain polymer content in these systems is negligible.

### 5.2.4 Centrifugation

An attempt was also made to drop the swollen microgels out of solution using centrifugation, leaving only free chains in the supernatant to be analysed with

## 5.3 Rheological experiments

---

light scattering. However this did not succeed, likely due to an insufficient density differential between the microgels and the suspending medium. This was performed with an ultracentrifuge, reaching acceleration in excess of  $200000g$ , but resulted in no visible deposition occurring, followed by positive detection of microgels while light scattering. To verify the concept of this experiment, this was repeated with more densely cross-linked microgels of similar chemical composition and homogeneity of crosslinking. These microgels visibly deposited and compacted enough that it was necessary to apply manual pressure to clean the inside of the sample tube. While qualitative, this is included as a demonstration of the sparseness of crosslinking of these microgels, as this implies the microgels are very closely density matched with water, in turn indicating a low crosslink density and ideal solvent and counterion condition.

## 5.3 Rheological experiments

The key information we wish to extract from these systems is their rheology, their response to a mechanical stimulus such as shearing in a plate geometry. We are also interested in comparing the macrorheological responses to the results of our simulations, including the macroscopic moduli of the system, or whether there exists a true yield strain or stress, but this will be discussed in [Chapter 6](#).

### 5.3.1 Experimental setup

All measurements in this chapter were performed on stress-imposed rheometers manufactured and maintained by Anton Paar GmbH: the Physica MCR 502 and 302. The geometries used were a cone-plate (CP) geometry with diameter 50mm,

## 5. EXPERIMENTAL RHEOLOGY

---

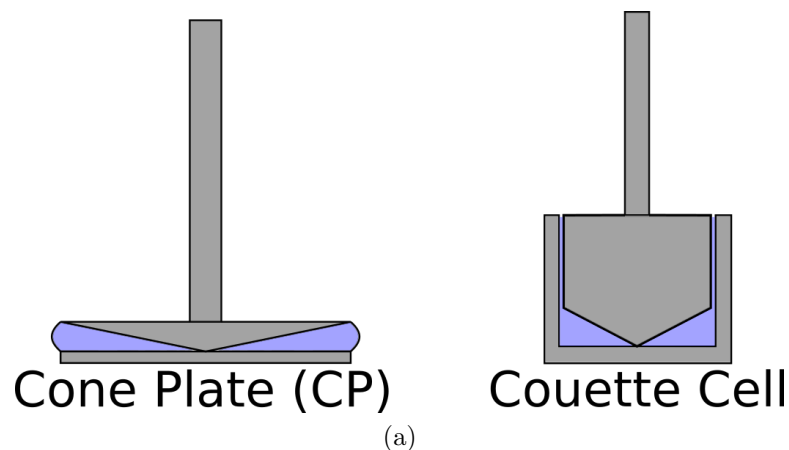


Figure 5.3: Schematic of plate and cell geometries used for rheological measurements.

cone angle  $2^\circ$ , and a simple couette cell with bob diameter 28.7mm and a gap of 0.099mm. A schematic of these geometries can be seen in [Figure 5.3](#).

The CP geometry was used for the majority of measurements, with the couette cell being used to extend the accessible range of shear rates possible in the experiment, which is possible due to the lower inertia of this geometry. With the CP geometry, we systematically use a solvent trap to keep humidity constant close to the sample. All rheological measurements were performed at  $20^\circ\text{C}$ , ensured by a water bath connected to the lower section of the geometry.

In all cases, flowcurve measurements were performed first, with an hour of rest between these and frequency sweep measurements to allow trapped stress to decay.

### 5.3.2 Steady shear

A selection of tests were performed in rotational steady shear. These consist of targeting an applied strain rate,  $\dot{\gamma}$  whilst applying a stress  $\sigma$ , using the measured strain rate to continually adjust the applied stress such that corresponding values are arrived at for a steady state in stress. This may involve an initial 'hump' of stress, as the material resists rearrangement until it yields, so shear rate is held constant until the steady state value is determined. This investigation of the steady shear response is sometimes referred to as a flowcurve experiment. Flow curve experiments were conducted via two different protocols. The originating protocol used is indicated with each set of results. Where it is not indicated, only the automatic protocol was used for that concentration.

The first is to use the automatic protocol of the rheometer, which uses a proprietary algorithm to determine when each measurement has reached its steady state value. The low shear rate stress measurements were verified through setting steady stresses and measuring the shear rate. This is referred to as 'auto' in figures. The second is to manually set a logarithmic ramp, and hold each shear rate constant for a time proportional to the shear rate, and then determine the steady state value from the last 5% of measurements. This is referred to as 'startup'. Both of these measurements were conducted ramping from high shear rates to low,  $10^3 \text{ s}^{-1}$  to  $10^{-2} \text{ s}^{-1}$ , for reproducibility of results, with a logarithmic interval. The rheological response can be history dependent, and the higher initial shear rates will destroy whatever structures are trapping stress in the system, if they exist, giving reproducible data at the more history sensitive lower shear rates. The number of of points per decade is 5 for most measurements, but may vary.

## 5. EXPERIMENTAL RHEOLOGY

---

‘Auto’ and ‘Startup’ terminology are also used for plots of oscillatory data, as described below. This denotes whether they were performed after the corresponding flowcurve experiment, with the same sample and loading. This is indicated as the startup method is likely to keep the sample at high shear rates for significantly longer; rheology can be history dependent, as well as possibly resulting in a change in hydration of the sample even with the solvent trap or the chance of some sample being expelled, though this was not observed upon visual inspection after measurement. If not specifically stated, the measurement is made with the auto method.

Automatic ramping measurements were also conducted with the Couette cell on a few samples, logarithmically ramping both up and down through the range  $1\text{s}^{-1}$  to  $4.5\times 10^4\text{s}^{-1}$ , to extend the experimental range. Due to time pressures, this was only performed with a limited number of samples.

### 5.3.3 Oscillatory rheology

#### Frequency sweep

In the limit of small deformations, oscillatory manipulation can be used to probe the rest structure and morphology of a material. This can be done in the linear regime, where the storage and loss moduli,  $G'$  and  $G''$ , can be decomposed. To probe the structure at rest, a frequency sweep is performed, applying a small sinusoidal oscillatory strain to the sample of the form:

$$\gamma = \gamma_0 \sin(\omega t) \tag{5.2}$$

### 5.3 Rheological experiments

---

where strain  $\gamma_0$  is kept to 1%, and the frequency  $\omega$  is varied logarithmically from 100rad/s to 0.01rad/s.

The standard response received from a viscoelastic fluid is of the form:

$$\sigma = \sigma_0 \sin(\omega t + \delta) \quad (5.3)$$

where  $\delta$  is the phase shift between the applied strain  $\gamma$  and the corresponding stress response  $\sigma$ . In the linear regime, in-phase and out-of-phase responses can be decomposed as:

$$\sigma = \gamma_0 G' \sin(\omega t) + \gamma_0 G'' \cos(\omega t). \quad (5.4)$$

Here,  $G'$  represents the conservative, elastic response in phase with the strain  $\gamma$ , while  $G''$  represents the viscous, dissipative response in phase with the applied strain rate,  $\dot{\gamma}$ . For this reason,  $G'$  and  $G''$  are sometimes referred to as representing ‘solid-like’ and ‘liquid-like’ behaviours respectively. As we used stress-imposed rheometers, we apply a stress and measure the strain or strain-rate. Performing a frequency sweep such as this, we can see whether solid-like or liquid-like behaviour dominates in the range investigated. We can extract the value of  $G'$  at the minimum of  $G''$  to acquire an estimate the value of the elastic modulus of the suspension,  $G_0$ .

#### **Amplitude sweep**

As the amplitude of shear is increased, solid-like suspensions will eventually yield, and begin to flow. This regime is non-linear, and is used here to investigate the yield stress and strain. Similarly to a frequency sweep, we apply oscillatory strain, but instead hold frequency  $\omega$  constant while varying strain  $\gamma_0$ . For each sample,

## 5. EXPERIMENTAL RHEOLOGY

---

unless otherwise specified,  $\omega$  takes values of 0.1, 1 and 10 rad/s for respective amplitude sweeps, with  $\gamma_0$  varied between 0.01% and 1000%, in a logarithmic fashion. Due to time pressure, this was only done with a limited number of samples.

### 5.4 Results and discussion

#### 5.4.1 Batches

The aim of the work discussed in this section was to obtain rheological data on very soft microgels, and assess them as a candidate system to compare our simulation results to, as previous simulation work had been unable to reproduce the rheological properties of these particular microgels. As these were synthesised by a third party and Batch 1 was previously characterised in [Mattiello \(2018\)](#), we include results from this previous work and use it to augment the work carried out. Following this, the aim was to further investigate consistency between Batch 1 and Batch 2.

Firstly, we will discuss the flowcurves, the measurement for which we have the most complete data, then the frequency sweeps, and finally the amplitude sweeps. Data is only included in these plots if we have comparable measurements from Batch 1 and Batch 2. As mentioned, Batch 1 and Batch 2 of this microgel were synthesised and prepared in an identical manner. However, we observe that their rheological response differs.

In [Figure 5.4](#), we observe that in flowcurves for 1.5wt%, 2.5wt%, 3wt%, 4wt% and 5wt%, there is good agreement between our measurements of Batch 1 and the

## 5.4 Results and discussion

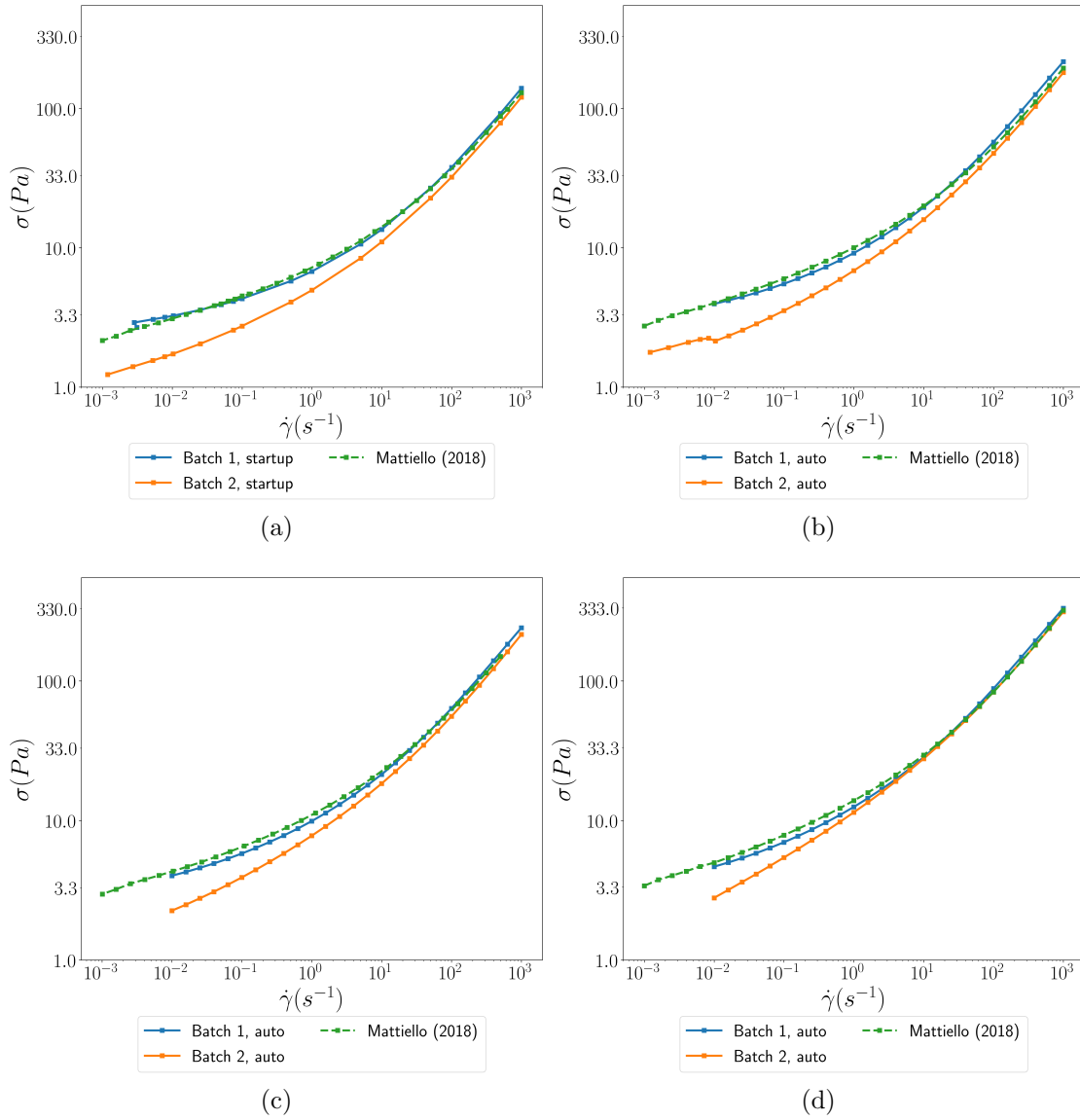


Figure 5.4: Log-log Flowcurves showing difference between previous measurements of Batch 1 by [Mattiello \(2018\)](#), new measurements of Batch 1 and measurements of Batch 2 at various wt% of microgel: (a) 1.5wt%, (b) 2.5wt%, (c) 3wt%, (d) 4wt%,

## 5. EXPERIMENTAL RHEOLOGY

---

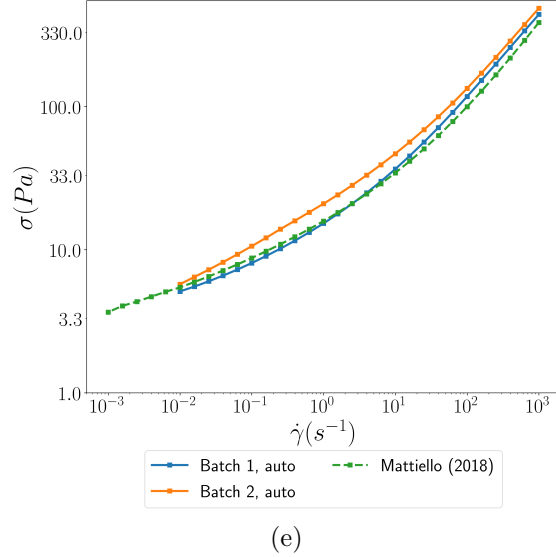


Figure 5.4: (e) 5wt%.

measurements of [Mattiello \(2018\)](#). This both confirms the reproducibility of the data and the stability of these microgels. Additionally, in the high rate regime, we can see similar behaviour between all 3 sets of measurements. However, at lower shear rates we can observe a disparity in responses between Batch 1 and Batch 2. For concentrations of 1.5wt%, 2.5wt%, 3wt%, 4wt%, the lower shear rate stress response of Batch 2 is consistently below that of Batch 1, with Batch 1 producing up to 1 to 2.5 times the stress. Conversely, for the 5wt% flowcurve, batch 2 actually has a higher stress response than Batch 1 measurements, with the maximum ratio of  $1.38\times$ .

Low shear rate values will naturally have the most variation due to their low magnitude and the difficulty of ensuring that the stress response has truly converged to a steady state. As we lower the shear rate, we also raise the importance of the natural relaxation timescales in the measured response - high shear rates or frequencies correspond to forcing the system faster than it is able to rearrange

itself to respond, whereas at lower shear rates the particular response of the system may be more dependent on its ability to rearrange. The significantly smaller dimensions of the microgels in batch 2 would allow faster relaxation of structural stress, as smaller particles would be more mobile. If the batches differ in their ability to dissipate stress, this will manifest most clearly at low shear rates.

Despite differences at low shear rates, it can be seen that the flowcurve response of both batches is qualitatively similar, with both reaching a similar gradient at high shear, and neither displaying a true plateau at low shear rate, indicating that neither is a true yield stress material.

Comparing the linear rheology of the two batches, in [Figure 5.5](#), we can see that for 1.5wt% and 3wt%,  $G'$  and  $G''$  for Batch 1 are greater than their counterparts in Batch 2. Curiously we see that for 5wt%, while  $G'$  is higher for all  $\omega$  for Batch 1,  $G''$  is similar at high shear rates and Batch 2 exceeds that of Batch 1 at lower shear rates. Additionally,  $G''$  converges at the lowest shear rates, although the low frequency  $G''$  measurements are the most likely to have high relative error, due to their low magnitude.

Batch 1 results taken are less consistent than those for the flowcurves, with the work of [Mattiello \(2018\)](#) showing results intermediate between the more recent measures of both batches at 3wt%. It should be noted that the 3wt% results were taken with slightly different experimental conditions due to the difference in flowcurve protocol, as discussed in [subsection 5.3.2](#), which may affect their response. Rheology can be history dependent, and the time that a sample is held at a particular shear rate may affect this, as well as there being the possibility of variation of hydration level, or expulsion of sample. Due to probing of the structure of the sample, frequency sweeps are more likely to be affected by the

## 5. EXPERIMENTAL RHEOLOGY

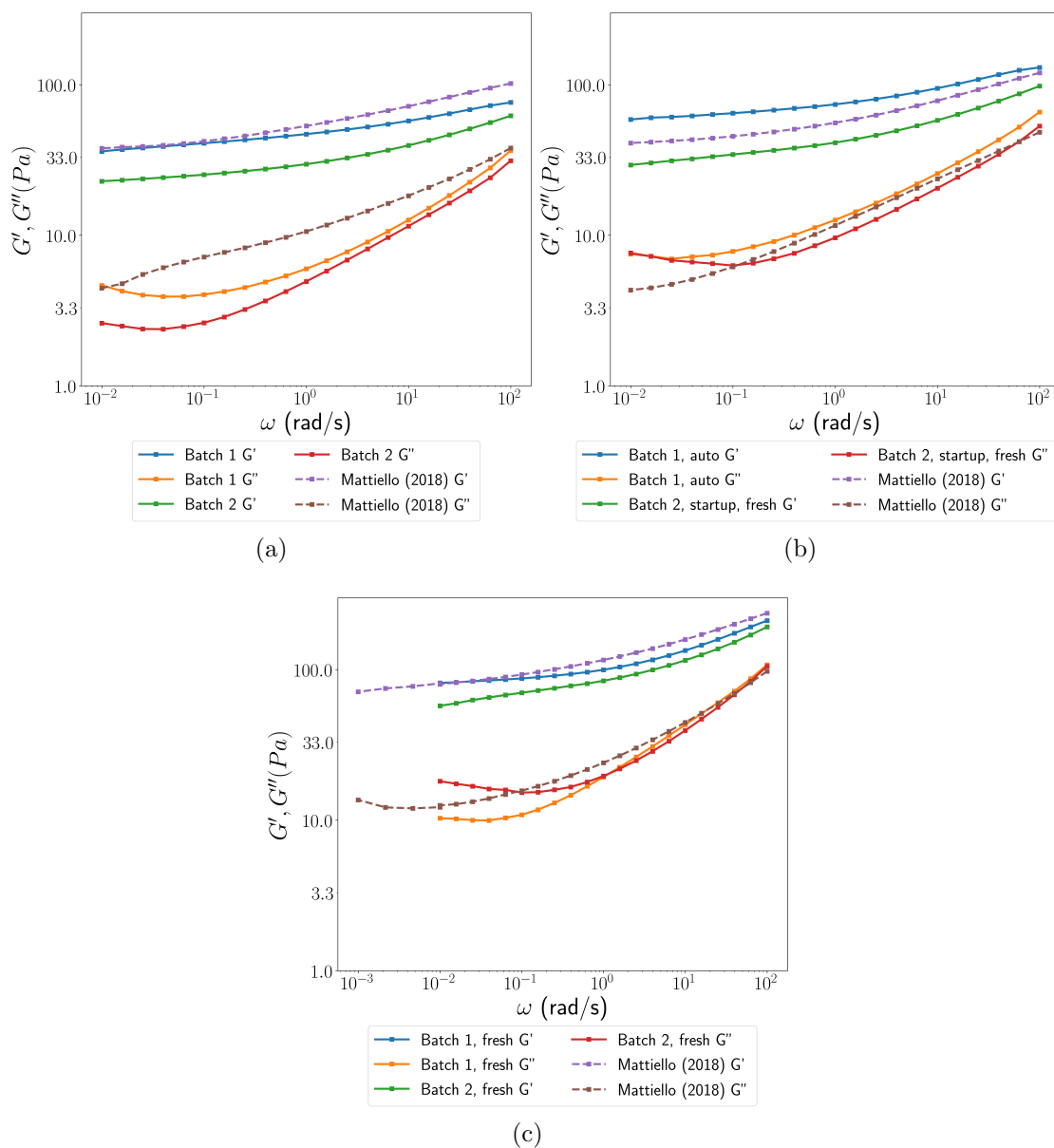


Figure 5.5: Log-log Frequency sweeps showing difference between previous measurements of Batch 1 by [Mattiello \(2018\)](#), new measurements of Batch 1 and measurements of Batch 2 at various wt% of microgel: (a) 1.5wt%, (b) 3wt%, (c) 5wt%.

## 5.4 Results and discussion

history and therefore the structure of the sample. For 5wt%, we again see a slight mismatch between  $G'$  values for high frequencies, although this lessened at lower frequencies.

General behaviour is largely similar for both batches, with both having a primarily elastic response in the regime, and minima in the viscous response within the experimental range. The shape of the decline in both moduli are similar. The appearance and placement of the viscous minima appears to differ between the work of [Mattiello \(2018\)](#), but the experimental protocol may vary slightly; they do not provide detail of whether their experiments are conducted on the same sample loading, which could influence results.

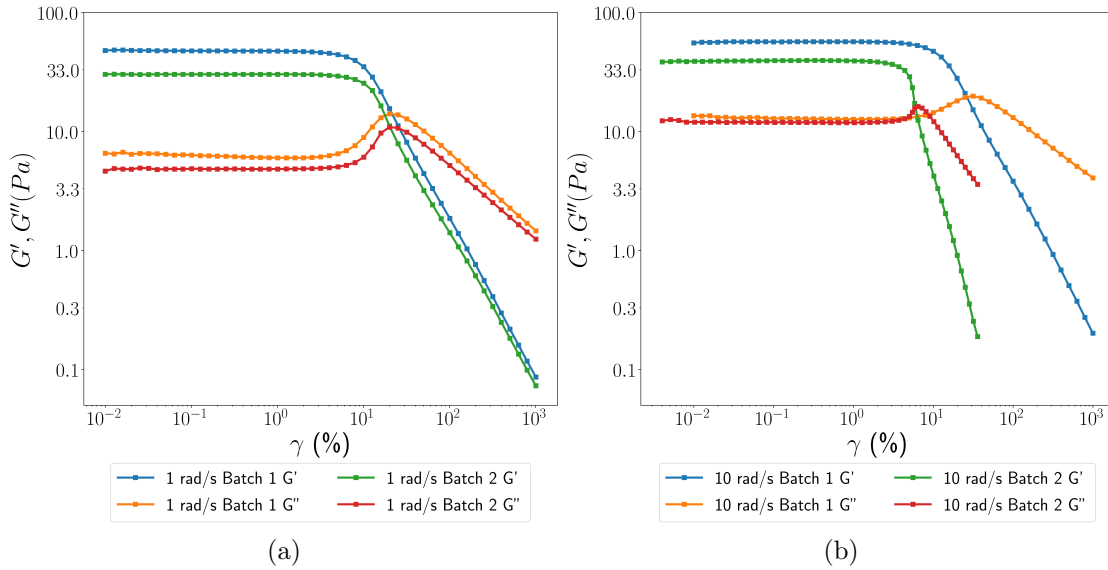


Figure 5.6: Log-log amplitude Sweeps showing difference between measurements of Batch 1 and measurements of Batch 2 at 1.5 wt% of microgel at  $\omega =$  for (a) 1 rads<sup>-1</sup>, (b) 10 rads<sup>-1</sup>.

Amplitude sweeps comparing the two batches were conducted on a single concentration due to time constraints. Stress responses of Batch 1 are higher

## 5. EXPERIMENTAL RHEOLOGY

---

than Batch 2, consistent with other methods of investigation. Yield stress and strain on these plots, indicated by the crossover and subsequent dominance of  $G''$ , is quite similar for the lower frequency, but at the higher frequency we can see that the yield strain is notably lower on Batch 2, although the yield stress is again quite similar.

Unfortunately, time was not sufficient to explore structure differences in Batch 2 through other techniques. It is possible that there are structural differences between the batches, which affect their ability to rearrange at lower shear rates and frequencies. Due to the weakness of crosslinking, there could be an extreme dependence of particle stress response on the internal structure of those particles. It is also possible that the smaller size of Batch 2 contributes to these effects. It is difficult to speculate further without further characterisation of the two batches, or comparing more identically prepared batches to see if a range of behaviours is observed.

To summarise, results between the batches are qualitatively similar, with differences more generally more significant at lower shear rates or frequencies. This is unlikely to arise solely from structural differences of the overall sample as the amplitude sweep shows greater difference at the higher frequency at higher amplitude strain, where the sample structure is likely to have been destroyed. Ideally, a greater number of amplitude sweeps at higher concentrations would have been useful to compare, as we can see from the flowcurves and frequency sweeps that  $10^1 s^{-1}$  at 1.5wt% concentration is lower than the value at which the batches collapse onto the same gradient for this concentration. It would be interesting to see if this crossover of stresses is consistent. It is possible that the difference in size allows for easier relaxation at longer timescales, but further investigation would

be required. Additionally, we have shown there is no significant degradation in the batch over time, as Batch 1 results are in good agreement with the work of [Mattiello \(2018\)](#)

### 5.4.2 Aging and history dependence

For both glassy and soft colloidal systems, relaxation of trapped stress can take a significant amount of time ([Hunter & Weeks, 2012](#)). For this reason, we investigated the aging behaviour of several samples, performing experiments on fresh samples and then allowing them to age for approximately a week, left at rest before repeating.

As can be seen in [Figure 5.7](#), differences between fresh and aged samples of both batches are minimal, and can be reasonably assumed to be within experimental error, given variation between loadings and error of the equipment. There are some indications of a slight relaxation for all samples except for 5wt% of Batch 2 from fresh to aged measurements, but this is not consistent in all cases and is small in magnitude. The minimal ratio is of 5wt% Batch 1, with the aged measurement being 0.83 of the fresh measurement. The flowcurve measurements therefore do not show significant aging in these systems.

Frequency sweep results, as can be seen in [Figure 5.8](#), paint a similar picture. Results are similar between all measurements, although a slight relaxation can possibly be seen for the 3wt% and 5wt% Batch 1 results. Curiously, the results of batch 2 after the startup steady shear experimental protocol appear even more consistent - this possibly indicates dependence on history of the sample, as the startup experimental protocol will always measure at a particular shear rate for

## 5. EXPERIMENTAL RHEOLOGY

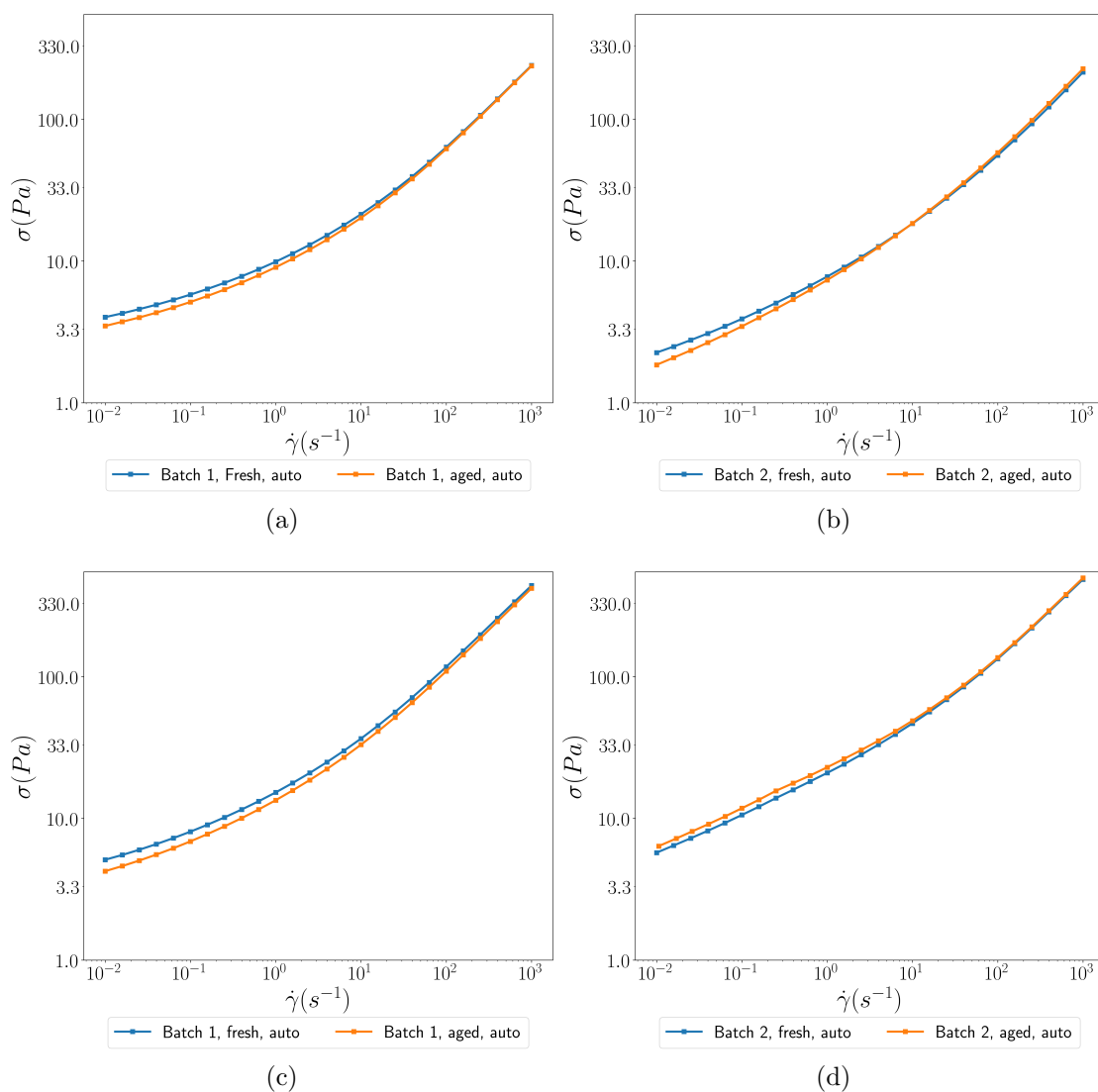


Figure 5.7: Log-log Flowcurves showing difference between measurements fresh (1 day after sample preparation) and aged (1-2 weeks after sample preparation) for (a) 3wt%, Batch 1, (b) 3wt%, Batch 2, (c) 5wt% Batch 1, (d) 5wt% Batch 2.

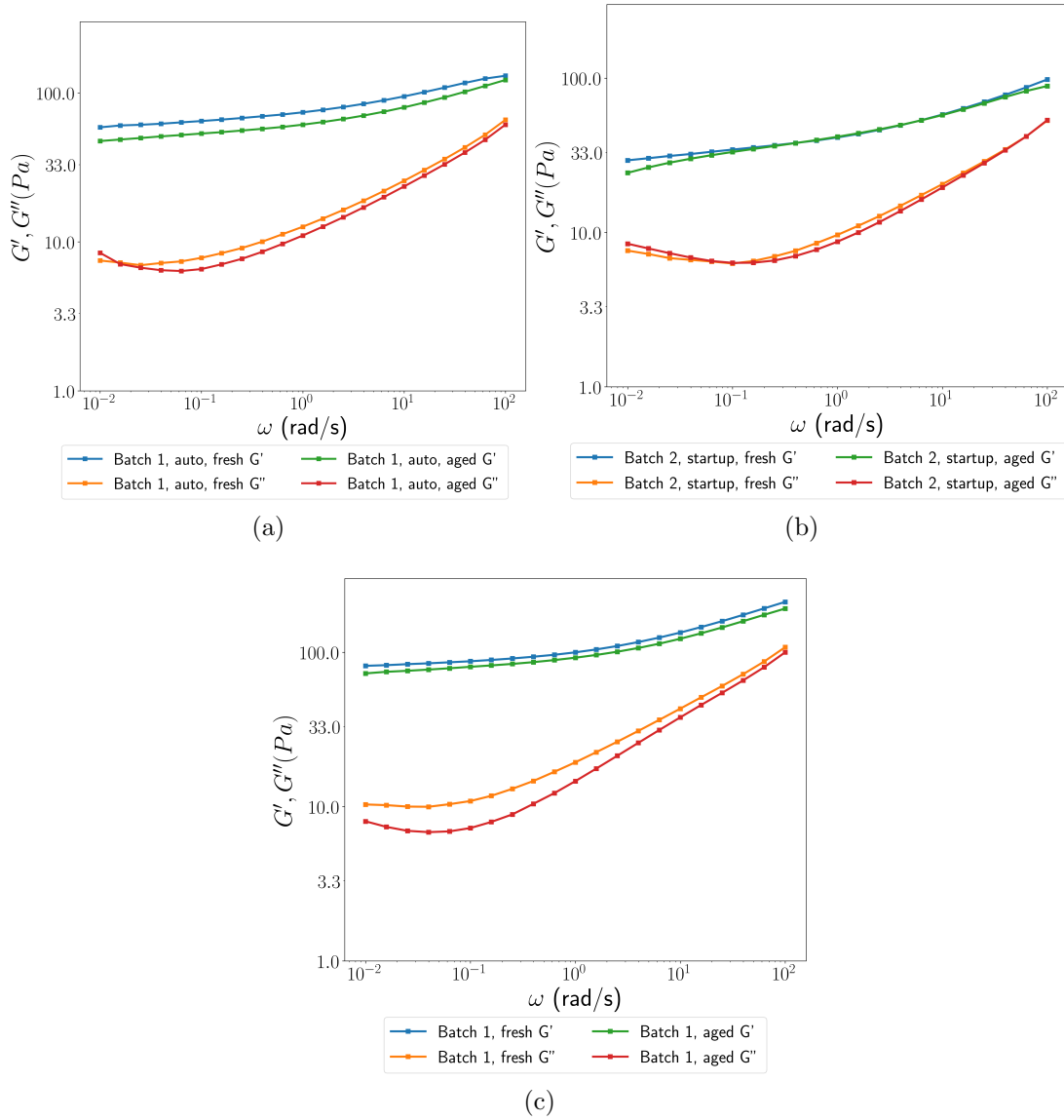


Figure 5.8: Log-log frequency sweeps showing difference between measurements fresh (1 day after sample preparation) and aged (1-2 weeks after sample preparation) for (a) 3wt%, Batch 1, (b) 3wt%, Batch 2, (c) 5wt% Batch 1.

## 5. EXPERIMENTAL RHEOLOGY

---

a fixed time, whereas the auto protocol may vary time overall somewhat. This may indicate a history dependence that is stronger than any aging dependence. If true, this would also suggest that the experimental protocol of an hour rest between steady shear measurement and oscillatory measurement is not enough to relax all trapped stress from the system. However, as we can see in [Figure 5.9](#), while there is a higher stress following the startup flowcurve measurements, this difference is minimal. As measurement for each protocol presented here were taken on a single sample loading, a strong history dependence is not indicated by these results, though they are restricted to a single concentration with a single sample loading for each.

In general, these results do not show a strong dependence on aging in the sample, and do not indicate a strong history dependence, although the history dependence may need more investigation to entirely rule out.

### 5.4.3 Master flowcurve

Through appropriate scaling choices, it is possible to collapse the flowcurves from different concentrations onto a single flowcurve. For the more densely crosslinked syntheses, and other soft matter systems such as emulsions and films, the flowcurves can be collapsed by scaling shear rate with  $\frac{\eta_s}{G_0}$  and stress by  $\frac{1}{\sigma_y}$ , with a high shear gradient of 0.5 generically across different systems ([Basu \*et al.\*, 2014](#); [Bécu \*et al.\*, 2006](#); [Cloitre \*et al.\*, 2003](#); [Liu \*et al.\*, 2018](#); [Mattiello, 2018](#); [Nordstrom \*et al.\*, 2010](#); [Paredes \*et al.\*, 2013](#); [Pellet & Cloitre, 2016](#); [Seth \*et al.\*, 2011](#)). In these scalings,  $\eta_s$  is the viscosity of the solvent,  $G_0$  is the low-frequency modulus, the yield stress  $\sigma_y$  is obtained by taking  $\sigma$  at the point where the gra-

## 5.4 Results and discussion

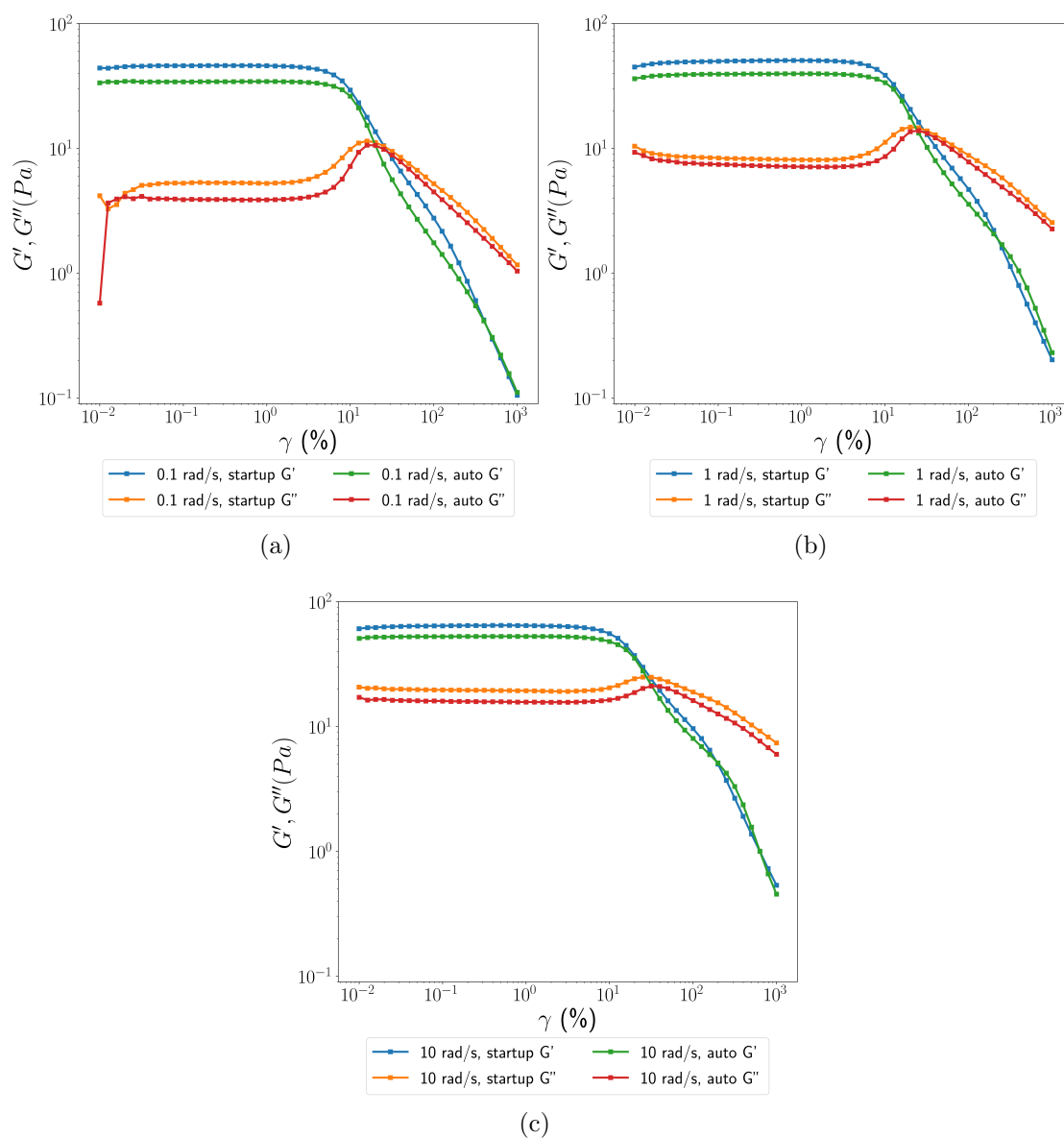


Figure 5.9: Log-log amplitude sweeps showing difference between measurements for 2.5wt% Batch 2 for (a) $0.1\text{rads}^{-1}$ , (b) $1\text{rads}^{-1}$ (c) $10\text{rads}^{-1}$ .

## 5. EXPERIMENTAL RHEOLOGY

---

dient changes when plotting  $\gamma$  against  $\sigma$  from the amplitude sweep experiments from a linear law at low strains; an example can be seen in [Figure 5.10](#). For these syntheses, the master flowcurve is described by the Herschel-Bulkley equation:

$$\frac{\sigma}{\sigma_y} = 1 + k\dot{\gamma}^n \quad (5.5)$$

with an exponent  $n$  of approximately 0.5. However, for the ultrasoft colloids, they

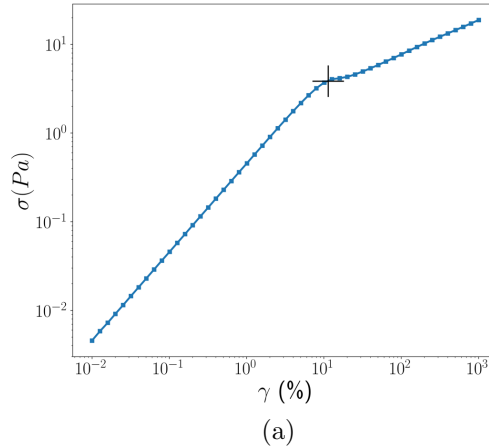


Figure 5.10: Representative stress-strain plot from which we extract  $\sigma_y$ , as an alternate presentation of values from amplitude sweep experiments shown elsewhere in the chapter. Value extracted marked on plot by cross.

found that simply scaling the stress by  $\frac{1}{\sigma_y}$  was sufficient to recover a master curve, meaning that the characteristic timescale of these colloids is independent of volume fraction. However, the resulting curve is not described well by [Equation 5.5](#), as it is not a true yield-stress material, and therefore does not feature the well-defined plateau at low shear rates. Additionally, the high shear rate behaviour follows a power law with an exponent of 0.65, rather than 0.5 as is found for more densely crosslinked colloids. They interpreted this as demonstrating that these

ultrasoft colloids behave quite differently to other soft colloidal systems.

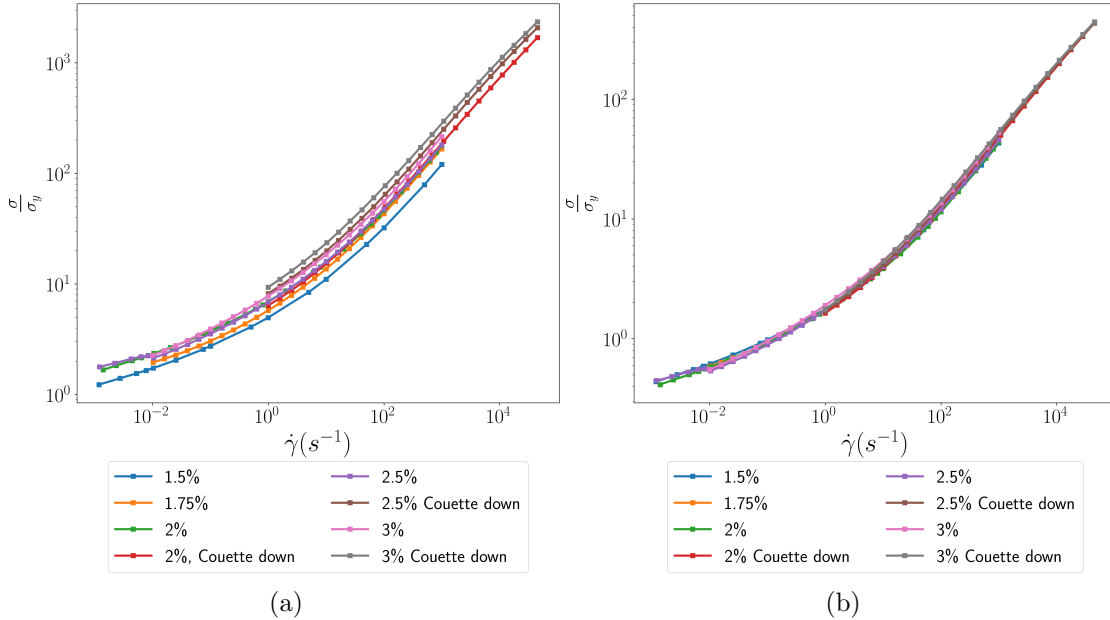


Figure 5.11: Log-log steady-state shear Flowcurves with Couette cell measurements for a range of Batch 2 measurements presented (a)unscaled, (b)scaled as indicated in [Table 5.1](#).

To examine this further we shall consider whether the flowcurves from Batch 2 can be superimposed in a similar manner. In [Figure 5.11](#), we present the unscaled and scaled flowcurves, including Couette cell measurements. We can see that an appropriate vertical scaling does collapse the results into good agreement, suggesting that this scaling behaviour is consistent across both batches. We chose scaling values based on the the gradient change as in [Figure 5.10](#), but altered these values as shown in [Table 5.1](#) to show that better scaling could be achieved. This is justified as the absolute values of  $\sigma_y$  are quite low (between 2.8Pa and 4.1Pa) and so are quite likely to have higher relative error associated

## 5. EXPERIMENTAL RHEOLOGY

---

Measurement	$\sigma_y$ (kPa)	Manual Scaling
1.5%	3	2.8
1.75%	2.9	3.3
2%	4.0	4.0
2% Couette down	4.0	3.9
2.5%	4.0	4.0
2.5% Couette down	4.0	4.8
3%	4.1	4.1
3% Couette down	4.1	5.3

Table 5.1: Table of Scaling factors for Flowcurves.

with them. Additionally, this is a loose approximation in identifying the point at which the gradient changes, and these are not true yield stress fluids. In general, the Couette measurements require different  $\sigma_y$  values to collapse onto the master curve, but as these use a different geometry this is consistent with the scaling. It can be remarked that values of the viscosity  $\eta_s$  and modulus  $G_0$  are in fact very similar between samples, suggesting that the  $x$ -axis can be rescaled to recover the master curve. That we can achieve good agreement scaling only the  $y$ -axis then suggests that the characteristic timescale of these ultrasoft colloidal systems is not dependent on the concentration of the system.

The high shear rate gradient for cone plate measurements up to  $10^3\text{s}^{-1}$ , has an exponent of approximately 0.62, which is similar to the 0.65 found for Batch 1. For the lone Batch 1 curve we have the measurements to scale in this manner, we recover an exponent of 0.62, possibly hinting at a systematic difference between measurements. The Couette measurements, while agreeing with this exponent at the maximum shear rate for the cone and plate, tend to values between 0.52 and 0.55 at the highest shear rates. The high shear Couette measurements do not collapse as well as the lower shear rates, but any relative error in  $\sigma_y$  would create

a greater error in scaling at the highest shear rates. However this does suggest the higher values of the exponent found for the highest rate for Batch 1 may be an intermediate that gives way to a 0.5 scaling at even higher strain rates.

## 5.5 Conclusion

In this Chapter, we have presented experimental results that build upon the work of [Mattiello \(2018\)](#). We have verified that there is a negligible amount of free chain content in these syntheses which does not influence rheological measurement. We have shown that the 2 batches of identically synthesised microgels show somewhat different low shear rate behaviour, but behave similarly at high shear rates. This low shear rate behaviour may also be adequately explained by the difference in volume of the microgels. We also conclude that both batches do not show typical soft microgel behaviour, with no true yield stress, and lend support to the existence of a new class of ultrasoft microgels with qualitatively distinct behaviour. We show that neither Batch has significant aging or history dependent properties, which is consistent with the proposed ability to self-squeeze to rearrange. Finally we find evidence that Batch 2 can be collapsed onto a single master curve solely through scaling by  $\sigma_y$ , though we find a slight mismatch in the exponents we recover.

## 5. EXPERIMENTAL RHEOLOGY

---

# Chapter 6

## Sheared Simulation Results

Having discussed quiescent simulations in [Chapter 4](#) and sheared bulk material responses for a candidate experimental system in [Chapter 5](#), in this chapter we simulate the response of our simulated colloidal systems to steady shear. We characterise the shear response of our simulated systems, and examine the effect shearing has on the rearrangement dynamics of the systems. The measures of rearrangement dynamics again consist of the time-dependent mean-squared displacement of the centre of mass of the colloids, with advective transport subtracted. We discuss the quantitative and qualitative similarities to the rheology from the experimental systems, constructing a flowcurve for steady state shear and the normal stress differences. We also will see the extent to which the randomised initial configuration is relevant to the measured stress. Finally, we will investigate how the structure of the system is altered by applying shear through calculating the scattering amplitude, in a manner suitably modified for a linearly sheared system. As an example of how shear might affect the structure of a system, [Khabaz \*et al.\* \(2017\)](#) find in their soft sphere systems that varying shear

## 6. SHEARED SIMULATION RESULTS

---

rates can induce ordering, such as face centred cubic, hexagonal close packed or layered arrangements - the latter being the existence of discrete layers of particles, with centres of mass of particles within a layer all closely matching the same  $y$ -coordinate within.

### 6.1 Shear

In this section we will briefly reiterate how linear shear is implemented within FFEA. We modify the periodic boundary conditions to Lees-Edwards boundary conditions, where projected images of the system in the gradient direction move in the flow direction relative to the simulation box. In all sheared systems we have simulated, the gradient is in the  $y$ -direction, flow is in the  $x$  direction and vorticity in the  $z$ . For the projected image in the positive  $y$ -direction, the offset distance  $O_{box}$  in the  $x$  direction is

$$O_{box} = \gamma L_y - n L_y \quad (6.1)$$

where  $n \in \mathbb{Z}$  such that  $0 < O_{box} < L_y$ , where  $L_y$  is the dimension of the box in the  $y$ -direction, and the total strain  $\gamma$  is calculated as

$$\gamma = \dot{\gamma} t \quad (6.2)$$

where  $\dot{\gamma}$  is the shear rate or strain rate - they are equivalent in these simulations - and  $t$  is the total time of the simulation. Interactions across box boundaries are modified accordingly, which is detailed in [subsection 3.1.3](#).

Additionally, an implicit linear shear in the solvent is implemented through

---

## 6.2 Parameter space and number of simulations

modification of the drag force on colloids, acting as a force on each node in the simulation of

$$F_x = \dot{\gamma} L_y d_S \left( \frac{y_{node}}{L_y} - \frac{1}{2} \right), \quad (6.3)$$

where  $F_x$  is the  $x$ -component of the drag force,  $\dot{\gamma}$  is the shear rate,  $L_y$  is the length of the simulation box in the  $y$ -direction,  $y_{node}$  is the  $y$  position of the node, and  $d_S$  is the Stokes drag scaling on the node. This gives zero force on the central plane of the box, and a linear velocity gradient in the  $y$ -direction.

## 6.2 Parameter space and number of simulations

We seek to simulate soft colloidal systems and, as discussed in [section 4.1](#), we were guided in our choice of parameter space by a combination of realistic representative values from experimental microgel systems ([Aufderhorst-Roberts \*et al.\*, 2018](#); [Voudouris \*et al.\*, 2013](#)) and practical constraints. As each simulation can take up to a month of compute time, we were forced to be selective in our choices of parameters, with the time available allowing an aim of only 5 instances of each set. Shear rates were chosen to match that of the experimental systems in [Chapter 5](#) for shear rates of simulations with  $\zeta_e = 1.0$ . For the lower value of  $\zeta_e$ , we selected only shear rates where we would reach at least a significant fraction of a strain unit (i.e where the strain is equivalent to a simulation box length.) with the lower effective volume fraction. An initial attempt was made at shearing systems with higher moduli, but system stability with higher moduli and high rates of shear excluded pursuing this further at this time. With further work, it would certainly be interesting to expand to sheared systems with higher moduli for comparison. The higher shear rates are simulated for a shorter time, as they

## 6. SHEARED SIMULATION RESULTS

---

$\zeta_e$	$K$ (kPa)	$G$ (kPa)	$\dot{\gamma}$ ( $s^{-1}$ )	$t$ (s)	Strain Units	No. of Viable Runs
1.0	2.00	0.600	0.01	$9.5 \times 10^{-3}$	$9.5 \times 10^{-5}$	5
1.0	2.00	0.600	0.1	$9.5 \times 10^{-3}$	$9.5 \times 10^{-4}$	4
1.0	2.00	0.600	1	$9.5 \times 10^{-3}$	$9.5 \times 10^{-3}$	4
1.0	2.00	0.600	10	$9.5 \times 10^{-3}$	$9.5 \times 10^{-2}$	5
1.0	2.00	0.600	$10^2$	$9.5 \times 10^{-3}$	0.95	5
1.0	2.00	0.600	$10^3$	$9.5 \times 10^{-3}$	9.5	5
1.0	2.00	0.600	$10^4$	$1.5 \times 10^{-3}$	15	5
1.0	2.00	0.600	$10^5$	$1.5 \times 10^{-3}$	150	5
0.7	2.00	0.600	$10^2$	$9.5 \times 10^{-3}$	0.95	5
0.7	2.00	0.600	$10^3$	$9.5 \times 10^{-3}$	9.5	5
0.7	2.00	0.600	$10^4$	$1.5 \times 10^{-3}$	15	5
0.7	2.00	0.600	$10^5$	$1.5 \times 10^{-3}$	150	4

Table 6.1: Table of parameters varied in sheared simulations

do not require as much time to have experienced at least a strain unit.

## 6.3 Results

### 6.3.1 Observed volume fraction

In a system of soft, compressible particles, we can only initialise our systems according to the effective volume fraction  $\zeta_e = \frac{nV_0}{V_{Tot}}$ , where  $V_0$  is the equilibrium volume of the colloid,  $n$  is number of colloids, and  $V_{Tot}$  is the total volume of the system. This may be quite different from the actual volume fraction  $\phi$ , calculated from the volume of the compressible colloids in the simulation divided by the volume of the simulation box. As a system is sheared, it may adopt a different structure, in a way that is related to the relaxation dynamics of the individual particles (Khabaz *et al.*, 2017). One way we can understand this restructuring is

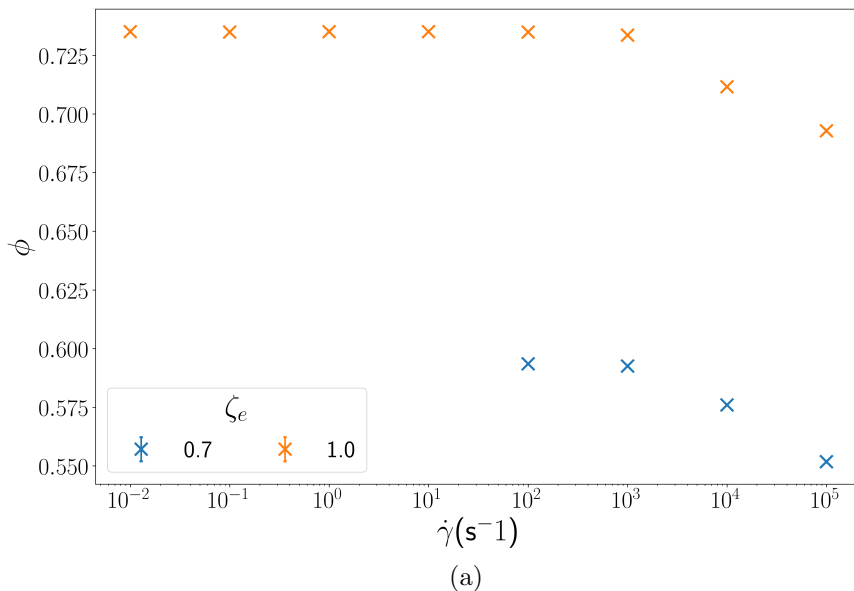


Figure 6.1: Observed Volume Fractions of Sheared simulations.

the shear timescale becoming faster than the relaxation timescale of the system - it can no longer revert to its default state and instead might flow differently. It is also possible that shear may give enough energy to the system to allow it to reach denser states such as crystalline ordering, that it could not easily reach from an initial disordered configuration simply through relaxation.

We display the the observed volume fraction at each shear rate in [Figure 6.1](#). We can see that below a shear rate of  $10^3\text{s}^{-1}$  the mean volume fraction for the simulations is not affected, but above decreases for higher shear rates. As we saw in [Chapter 4](#), the approximate timescale of the second shoulder for quiescent simulations (the return to a second diffusive regime, between the cages) for the 2kPa systems is approximately  $10^{-3}\text{s}$ . This suggests that at lower shear rates, although the shearing may assist cage-breaking, the main mechanism for mobility

## 6. SHEARED SIMULATION RESULTS

---

remains diffusive, between cages. When the shear rate corresponds to a timescale faster than that of the cage-breaking, the reduction in  $\phi$  implies a change in structure of the system.

### 6.3.2 Mean-Squared Displacement

We discussed in detail how we calculate and collect the MSD for sheared systems in [subsection 3.4.4](#), and presented results for quiescent systems in [section 4.5](#). To briefly reiterate, we calculate the time-dependent Mean-Squared displacement, or MSD, of the centre of mass of the colloids. Standard results for free diffusion of a sphere suspended in a fluid are  $\langle \underline{x}(\tau) \rangle = \underline{0}$  and  $\langle \underline{x}(\tau)^2 \rangle = 6D\tau$ , where  $x$  is the displacement over some time lag  $\tau$  as a scalar value, and  $D$  is diffusivity. Each step in diffusion is expected to be uncorrelated, and therefore sufficient sampling in any one direction will eventually be cancelled out by exploration in the opposite direction. We consider the MSD, and therefore magnitude of displacement, which will continuously grow.

As we apply a linear shear gradient through drag against our implicit solvent, each node in each colloid will undergo advective transport, which if used unmodified will be difficult to interpret and compare. We therefore attempt to remove the effects of Taylor dispersion ([Taylor, 1954](#)), by removing homogenous advective transport of the particles due to the shear gradient through Stokes drag against implicit background solvent. This is to isolate diffusion due to cage-breaking. This is discussed in more detail in [subsection 3.4.4](#). When analysing these results, we must consider that we may not entirely remove the effects of advective transport from the MSD - we remove the average of the advective trans-

port applied to each node of the colloid, but calculate MSD only for the centre of mass. As an example, in a large system where shear was applied only through the use of Lees-Edwards boundary conditions, without a shear gradient inside the simulation box, shear banding may occur. In this case, a homogeneous removal of shear would not be appropriate, and instead constructing a velocity field and removing the average of the local velocity would give a more accurate measure, as what we are really interested in is the movement of a particle relative to its nearest neighbours. However, this would require larger numbers of particles than we are able to simulate to be a sensible approach in our simulations, even though we may have advection driven by the boundary conditions.

We present mean-square displacement (MSD) of the sheared systems in [Figure 6.2](#) and [Figure 6.3](#). As in [section 4.5](#), we display our MSD results both in the format of their raw data, where periods of diffusive behaviour will display as linear slopes on a log-log plot, and caging will see a deviation away from that slope. Additionally, we plot this data divided through by the time lag  $\tau$ . As MSD grows as  $\tau$ , this will more clearly display diffusive behaviour as a plateau, caging as a decline, and faster motion than can be explained simply by MSD as an upwards slope. This measure will be a multiple of diffusivity at a plateau, but is more difficult to interpret otherwise as this would not represent perfectly diffusive behaviour.

In [Figure 6.2](#) we present results for the most highly packed systems we have simulated, covering the largest range of shear rates. We can observe that at shear rates of  $10^2\text{s}^{-1}$  and below, we have a very similar behaviour to the quiescent systems. There is a slight upward trend in diffusivity as we raise our shear rate up to this point, but the behaviour of these systems as measured through MSD

## 6. SHEARED SIMULATION RESULTS

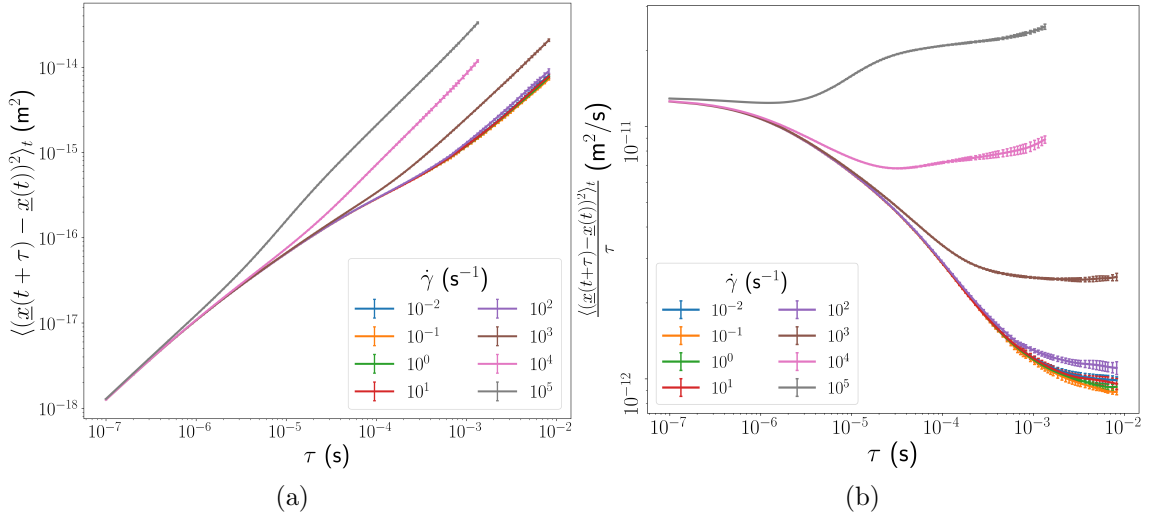


Figure 6.2: MSD of systems with  $\zeta_e = 1.0$  and varied  $\dot{\gamma}$ : (a) Simple MSD, (b) MSD divided by  $\tau$ .

is not greatly altered. At  $10^3 \text{s}^{-1}$ , we see a marked increase in diffusivity, but we still have clearly diffusive behaviour, with the emergence of the second plateau. At the higher shear rates, we transition to an upwards slope in long timescale MSD, which is no longer a normal diffusive behaviour, and for the highest shear rate the colloids do not actually experience a decline in MSD due to caging. We can interpret the long timescale higher diffusivity of the  $10^3 \text{s}^{-1}$  curve (taken from a plateau value in [Figure 6.2b](#)), and the slight increases of diffusivity at lower shear rates as an effective lowering of the energy barrier for rearrangement through shear. From the quiescent results in [Chapter 4](#), a key timescale appears to be approximately  $10^{-3} \text{s}$  (depending on volume fraction and moduli), where the approach to the second diffusive regime occurs, as well as the peak in non-Gaussian measures. We can then interpret the quantitatively different behaviour at this shear rate and the qualitatively different behaviour above it to be the

timescale of the shear approaching, and then exceeding the ability of the system to rearrange itself through thermal and elastic means to remove stress.

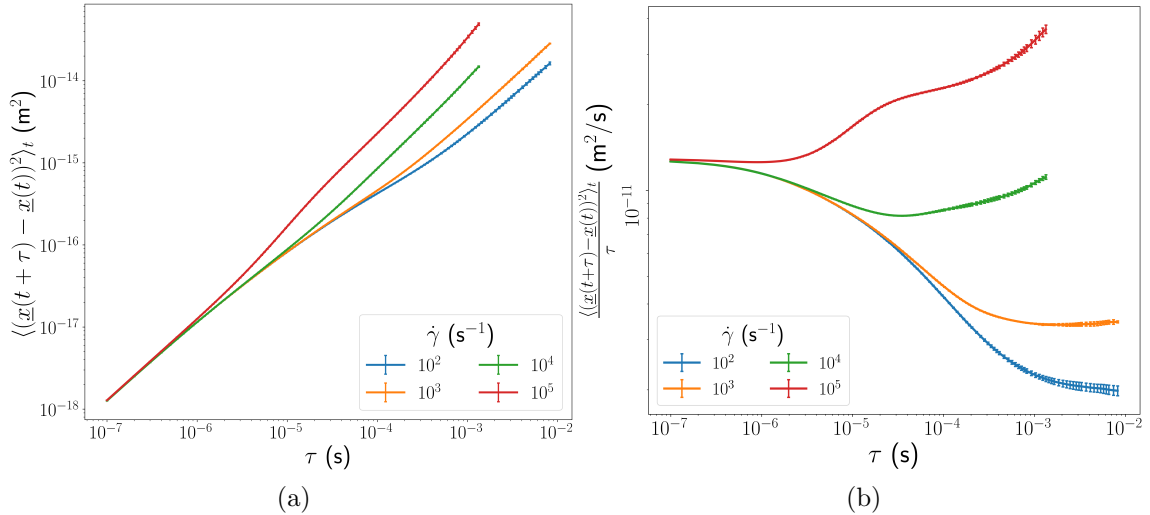


Figure 6.3: MSD of systems with  $\zeta_e = 0.7$  and varied  $\dot{\gamma}$ : (a) Simple MSD, (b) MSD divided by  $\tau$ .

In the plots that make up [Figure 6.3](#), we see similar behaviour. The results for a shear rate of  $10^2 \text{s}^{-1}$  are not significantly different to quiescent, at  $10^3 \text{s}^{-1}$  we see an elevated diffusivity, and for  $10^4 \text{s}^{-1}$  and  $10^5 \text{s}^{-1}$ , long timescale behaviour does not appear diffusive, and again the highest shear rate does not exhibit a caging decline.

Finally, we compare these results for the shear rates we have for both  $\zeta_e$  in [Figure 6.4](#). From this, we can see that at values  $10^2 \text{s}^{-1}$  and  $10^3 \text{s}^{-1}$ , the value of the MSD is significantly affected by  $\zeta_e$ . Above this value, we can see that  $\zeta_e$  becomes much less important to the dynamics, and while still relevant, the largest effect on the MSD is the new dynamics resulting from shear rates exceeding the timescale at which the system can relax, signifying that these systems transition

## 6. SHEARED SIMULATION RESULTS

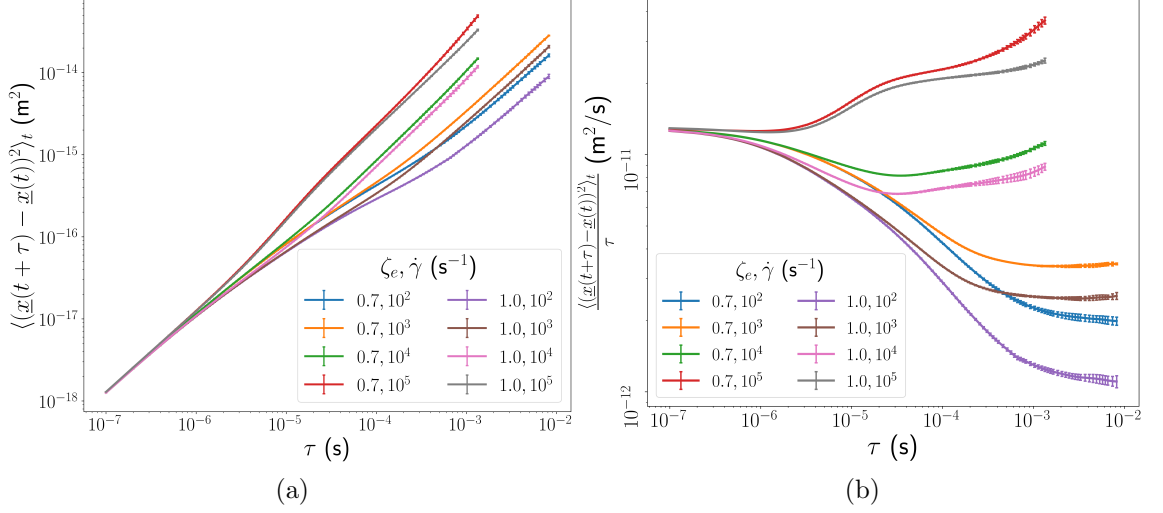


Figure 6.4: MSD of systems with  $\zeta_e = 0.7, 1.0$  and varied  $\dot{\gamma}$  for comparison: (a) Simple MSD, (b) MSD divided by  $\tau$ .

into a new regime of particle dynamics at these shear rates.

As we can see from the errors in general, system initial configuration does not have a significant effect on observed MSD.

### 6.4 Flowcurve

In this section, we discuss the flowcurve generated from the shear response of these simulated soft colloidal systems, and how it compares to examples from the experiments we described in [Chapter 5](#). We can see the flowcurves for the  $x$ - $y$  component of stress for these systems, sampled at the decades of shear rates in [Figure 6.5](#). To generate the values we take the mean of the stress for the latter half of each simulation, allowing time for shear response to reach a steady state. To ensure that this is the case, we plotted the moving average of the stress

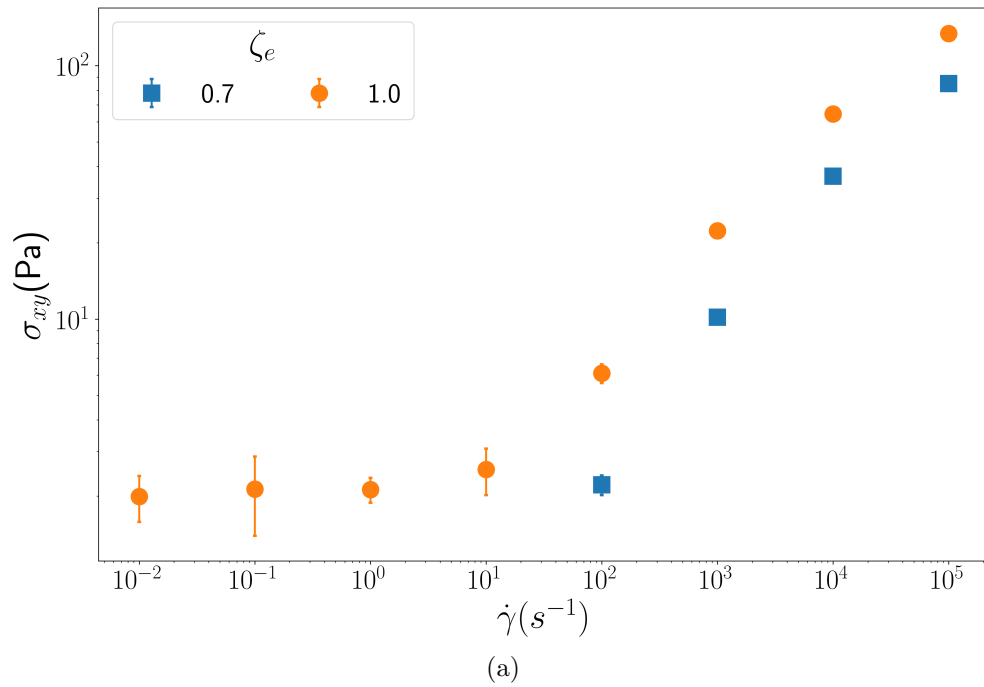


Figure 6.5: Flowcurve of systems with  $\zeta_e = 1.0$  and varied  $\dot{\gamma}$ .

## 6. SHEARED SIMULATION RESULTS

---

for these simulations and manually verified that simulations did not exhibit a transient startup stress. For the lower shear rate simulations, we can see that there is significant error, as these simulations have only experienced a fraction of a strain unit. The error in these stress measurements may therefore result from the stochastic nature of both the simulation initial configuration and the thermal activity of these systems. At higher shear rates, we can see the sampling error is smaller than the markers as plotted, and we can safely assume that a steady state stress response has been measured.

As anything under  $10^3\text{s}^{-1}$  has not undergone a significant fraction of a strain unit in the timescales we are able to simulate, we must be careful what we infer from this data. As discussed previously, these simulations take up to a month of compute time to complete, and simulating another decade in time is therefore impractical. Regardless, our systems appear to be shear thinning yield stress fluids with a low yield stress. This would explain also why the MSD only appears to be greatly affected at values where the systems have begun to yield. We can see that the stochastic element of our simulations is much more important at low shear rates, with the error being smaller than the marker for the data in our plot at higher shear rates.

As this curve appears at first glance to be consistent with standard shear-thinning behaviour, we analyse the gradient of this graph. A standard model for shear thinning fluids is the empirical Herschel-Bulkley relation ([Herschel & Bulkley, 1926](#)), which has the form:

$$\sigma = \sigma_y + k\dot{\gamma}^n, \tag{6.4}$$

where  $\sigma$  is the stress,  $k$  is a consistency index,  $\sigma_y$  the yield stress and  $n$  is the flow index. The gradient of the log-log plot therefore indicates the type of behaviour of the system. Where  $n > 1$ , the system is shear thickening, and where  $n < 1$  the system is shear thinning. If  $n = 1$  the system is simply a Newtonian fluid.

The curves for both volume fractions flatten out, with gradients going from a high for  $\zeta_e = 0.7$  of 0.66 between  $10^2\text{s}^{-1}$  and  $10^3\text{s}^{-1}$  to 0.36 between  $10^4\text{s}^{-1}$  and  $10^5\text{s}^{-1}$ , and for  $\zeta_e = 1.0$  the gradients are 0.54 and 0.32 at the same intervals. This is firmly below 1, and is decreasing, and so we conclude that we have a shear-thinning fluid. The decrease in scaling of the stress response at high shear rates is consistent with a rearrangement of the system once the timescale of shear exceeds the timescale at which it can rearrange, which we have seen previously in the decrease of volume fraction and qualitative change in MSD. We will also see evidence consistent with this in [subsection 6.4.2](#). Below this rearrangement, the stress is able to dissipate at low shear rates, then grows at  $10^3\text{s}^{-1}$  as stress builds against an amorphous structure. Above this shear rate, the system begins to layer, and while the stress response continues to grow, it grows more slowly due to the layering effect.

### 6.4.1 Normal stress differences

We look next at the normal stress differences  $N_1 = \sigma_{xx} - \sigma_{yy}$  and  $N_2 = \sigma_{yy} - \sigma_{zz}$ , which will tell us whether we have compressive stress aligning with the main axes, and how this compressive stress varies in different directions. The absolute values of these measures can be seen in [Figure 6.6](#). As we can see, these values match the behaviour of the general stress - low until  $10^3\text{s}^{-1}$  and then growing rapidly

## 6. SHEARED SIMULATION RESULTS

---

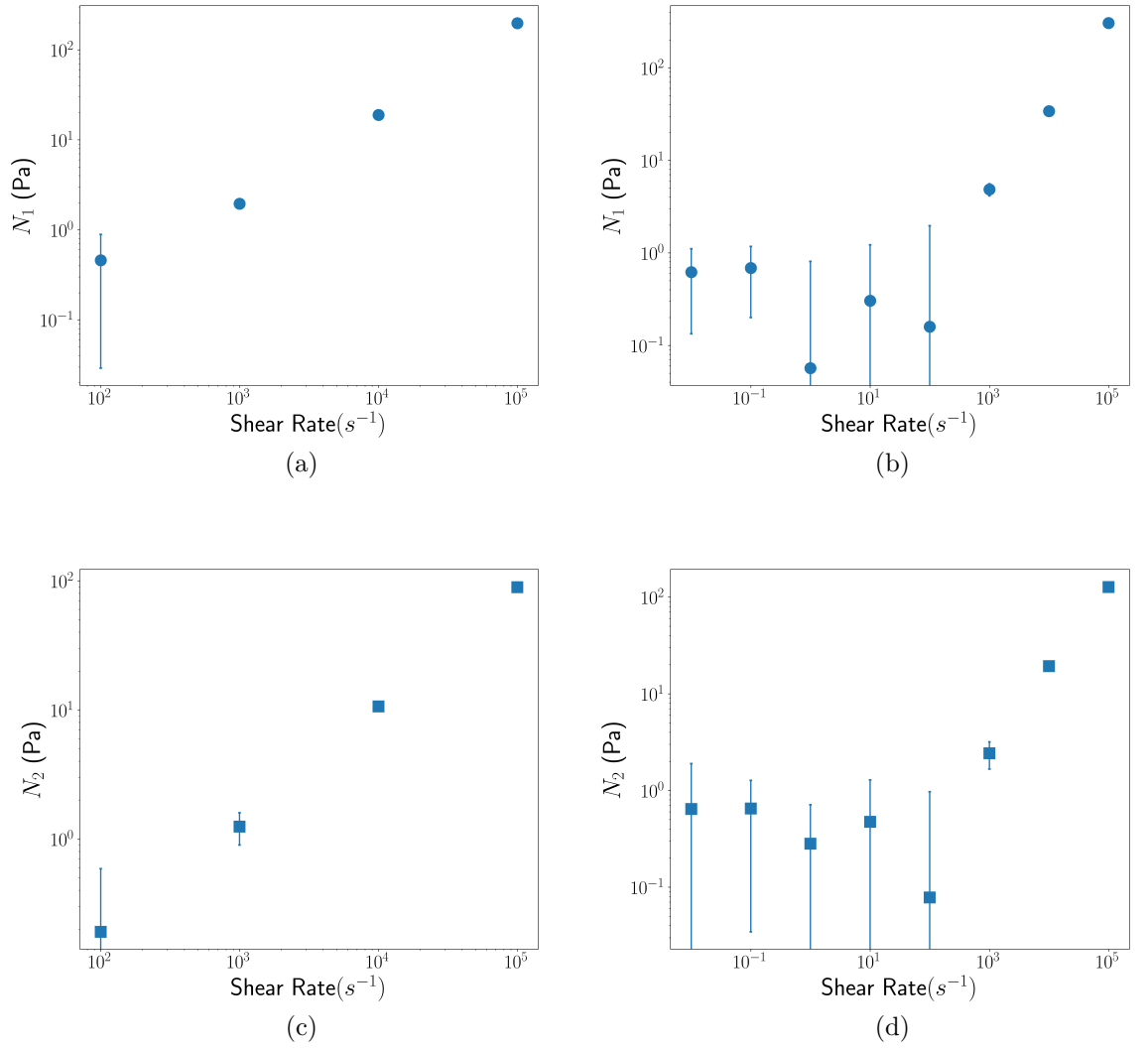


Figure 6.6: Magnitude of normal stress differences for all sheared simulations. If not visible, error bars smaller than markers. (a)  $N_1$  for  $\zeta_e = 0.7$ , (b)  $N_1$  for  $\zeta_e = 1.0$ , (c)  $N_2$  for  $\zeta_e = 0.7$ , (d)  $N_2$  for  $\zeta_e = 1.0$ .

thereafter. Due to the low size of the stress differences and the corresponding high relative error, alongside a comparatively high stress amplitude for the individual stresses, we should not read meaning into the lower values in the  $N_2$  plots. These values are all below one. The magnitude of  $N_1$  is approximately double  $N_2$  for all systems above a shear rate of  $10^3\text{s}^{-1}$ . The first normal stress difference is negative at these shear rates, and the second is positive, for both  $\zeta_e$  values. Due to the highly packed nature of the systems, the colloids are under compressive stress in all dimensions, and therefore  $\sigma_{xx}, \sigma_{yy}, \sigma_{zz}$  are all negative. This means they are experiencing more elastic stress in the  $y$ -direction than the  $x$ - or  $z$ -directions, which is consistent with layering under shear, as this would force greater compression than with a structure more similar to quiescent systems. Finally,  $\sigma_{zz} > \sigma_{xx}$ , which again is consistent with the shear acting to extend the particles in the  $x$ -direction as one would expect.

In general,  $N_2$  is negative, and of comparable size to  $N_1$ , which is consistent with previous predictions of fluids with internal deformable interfaces, such as emulsions, foams and polymer blends (Larson, 1997), although it is possible to observe this quality with the simpler Hertzian model with elastohydrodynamic lubrication that Khabaz *et al.* (2020) use, and does not require representing that deformability directly.

### 6.4.2 Scattering

In Figure 6.7 and Figure 6.8 we present the amplitude of the scattering in the  $x$ - $y$  plane, generated similarly to section 4.4 with an appropriate correction to the wavevectors  $\underline{q}$ , as the unit cell is being sheared. We use this measurement to

## 6. SHEARED SIMULATION RESULTS

---

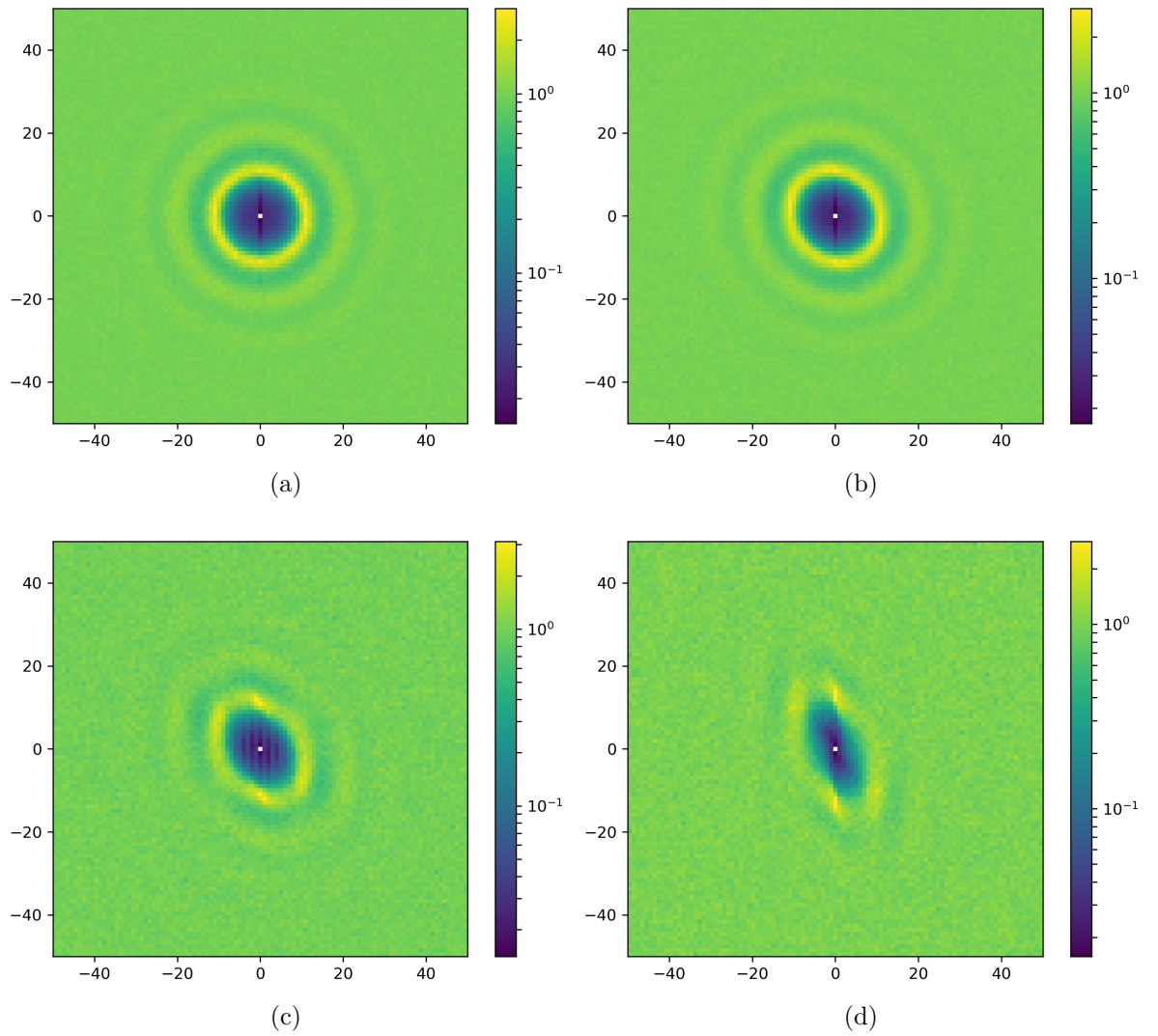


Figure 6.7: Averaged scattering amplitude for the  $x - y$  planes for all simulations at given parameter values. Results shown for  $\zeta_e = 0.7$ ,  $K = 2\text{kPa}$  at various shear rates: (a) $10^2\text{s}^{-1}$ , (b) $10^3\text{s}^{-1}$ , (c) $10^4\text{s}^{-1}$ , (d) $10^5\text{s}^{-1}$ .

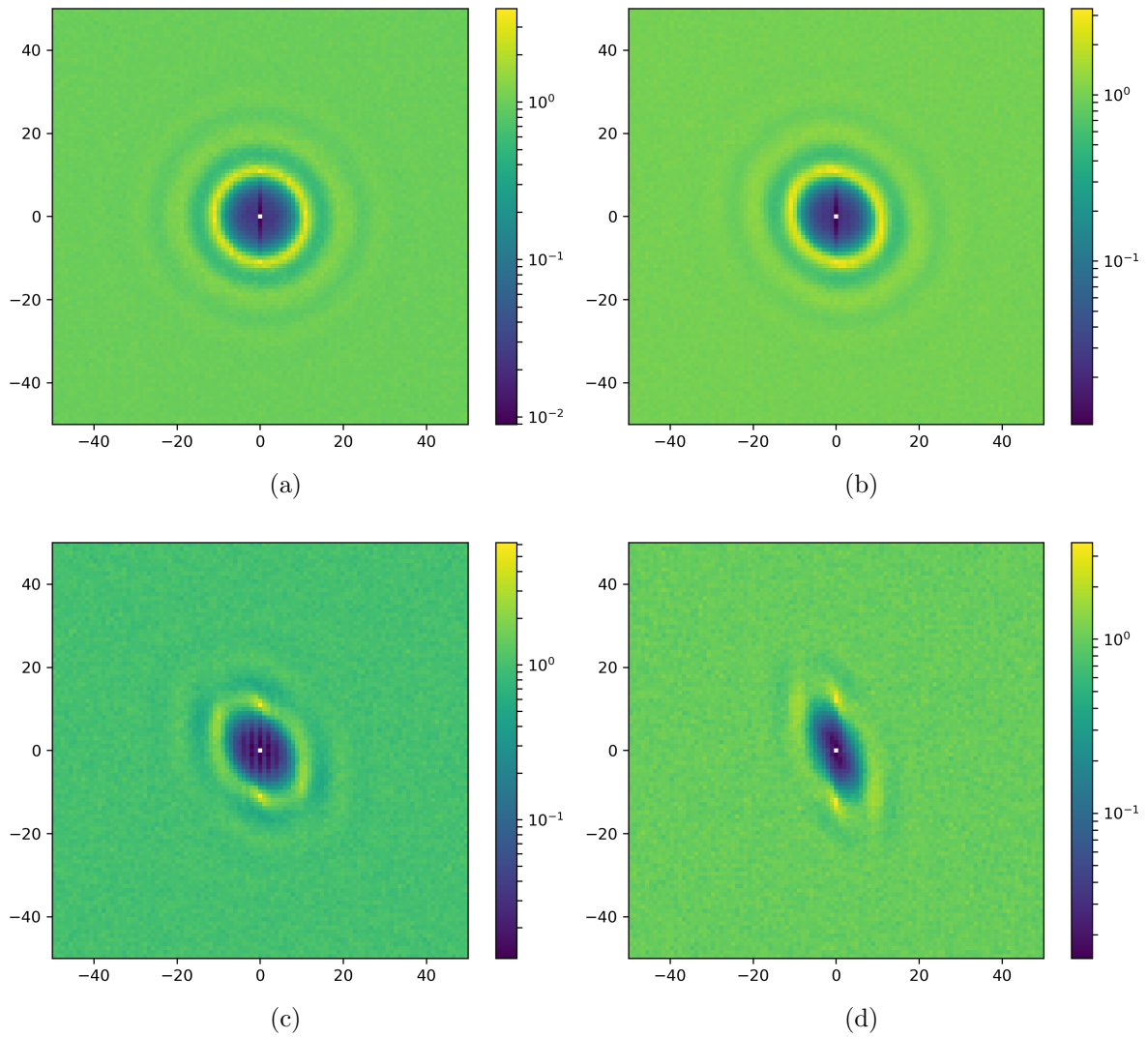


Figure 6.8: Averaged scattering amplitude for the  $x-y$  planes for all simulations at given parameter values. Results shown for  $\zeta_e = 1.0$ ,  $K = 2\text{kPa}$  at various shear rates: (a)  $10^2\text{s}^{-1}$ , (b)  $10^3\text{s}^{-1}$ , (c)  $10^4\text{s}^{-1}$ , (d)  $10^5\text{s}^{-1}$ .

## 6. SHEARED SIMULATION RESULTS

---

probe the structure of the system, to measure whether it is undergoing crystalline, amorphous or layered structures, or patterns of short range particle arrangement.

With this correction, values of  $\underline{q}$  are chosen as:

$$\underline{q} = \frac{2\pi}{L}(l, m - \alpha l, n) \quad (6.5)$$

where  $L$  is the box length, the offset of the box is  $R = \alpha L$ , and choices of  $l, m, n$  correspond to:

$$n = 0, l = (-l_{max}, l_{max}), m = (\lfloor -m_{max} + \alpha l \rfloor, \lfloor m_{max} + \alpha l \rfloor) \quad (6.6)$$

where  $l_{max}, m_{max} = 50$ . This correction is necessary for a sheared system, as the reciprocal lattice vectors will move with the strain, and  $m$  values are chosen to correspond to our fixed grid for plotting. Considering the reciprocal lattice, shear in the  $x$ -direction will manifest in the negative  $y$ -direction in these plots. As this is a shear-corrected case, we would expect to see a similar case to [section 4.4](#) for low shear: in the case where crystalline order is present, we would expect clear peaks in a lattice ordering, which would correspond to the reciprocal lattice of whichever crystalline form was present, and rings with number and sharpness dependent on the nearest neighbour distance if amorphous. For higher shear rates, we would expect to see a distortion of the central ring, and smeared peaks if crystalline. These behaviours can be seen in [Foss & Brady \(2000\)](#).

In both cases, we can see similar behaviour, with a shear rate of  $10^2\text{s}^{-1}$  barely distorting the quiescent result, and no evidence of longer range order, leading us to conclude this is an amorphous fluid. With a shear rate of  $10^3\text{s}^{-1}$ , we start

to reach timescales equivalent to the relaxation of the system, and therefore the shearing distortion is more pronounced. Finally, as we move to  $10^4\text{s}^{-1}$  and  $10^5\text{s}^{-1}$ , we see strong vertical scattering peaks present, showing layering - the systems are more strongly ordered in the  $y$ -direction. There is also a diffuse diagonal peak, which we interpret as a build up of particles forced together in their layers. While the stronger peak is a layer-layer correlation, the weaker peak is a colloid-colloid correlation, as they bunch in the direction of flow.

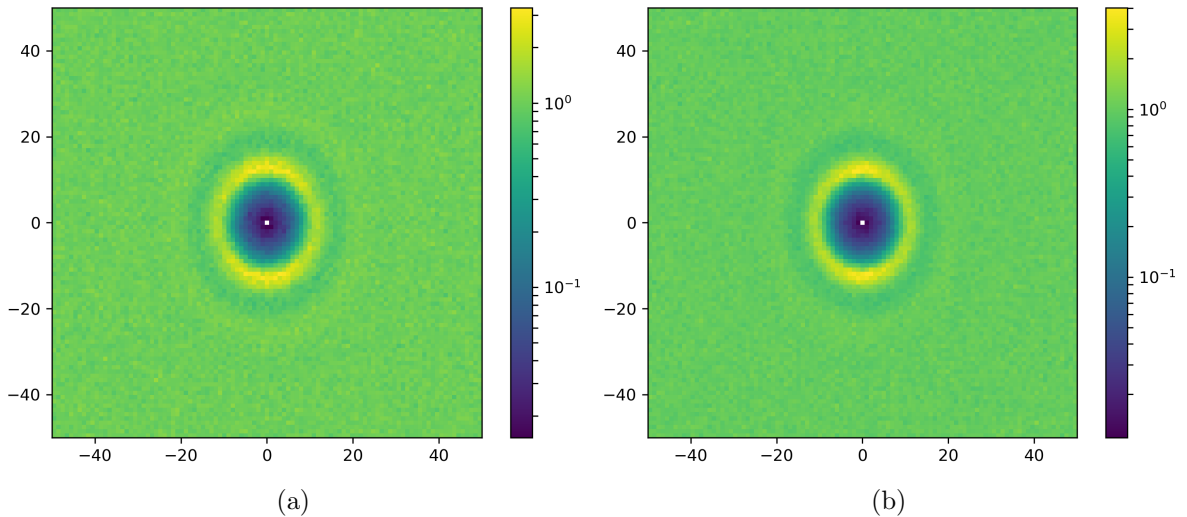


Figure 6.9:  $z$ - $y$  plane for simulations at  $10^5\text{s}^{-1}$  and at given parameter values. We vary  $\zeta_e$ : (a)  $\zeta_e = 0.7$ , (b)  $\zeta_e = 1.0$ .

Following this, we present results for the  $z$ - $y$  plane in [Figure 6.9](#). Calculation of this is unmodified from [section 4.4](#), as the reciprocal lattice is not affected in this plane by the shear. We present this only for the highest shear rate at each  $\zeta_e$ , as for lower shear rates it is not noticeably altered from the quiescent result. We can see in both cases there is a slight peak in the  $y$ -direction. The nearest neighbour scattering ring is also slightly longer in the  $y$ -direction and slightly thinner in the  $z$ -direction. We interpret this, due to the reciprocal relation to real

## 6. SHEARED SIMULATION RESULTS

---

distances, to be a compression in the  $y$ -direction, and a slight relative extension in the  $z$ -direction, which is again consistent with layering. To the resolution of the plot, the  $z$ - $y$  aspect ratio is approximately 1.2.

### 6.5 Comparison to experiments and other simulation techniques

From simulations of quiescent systems in [Chapter 4](#), we can see that all simulated systems are thermal within the timescale of 0.01s. Our simulated colloids are soft enough to rearrange solely due to thermal motion up to high volume fractions on a relatively short timescale. Due to this ability to deform, we compare them to the experimental results from ultrasoft colloids in [Chapter 5](#). The intent with this comparison is to see if having anisotropically deformable and compressible colloids is sufficient to avoid measuring a yield-stress fluid overall, or whether there are further subtleties to this phenomenon.

The curves for both volume fractions flatten out, with gradients going from a high for  $\zeta_e = 0.7$  of 0.66 between  $10^2\text{s}^{-1}$  and  $10^3\text{s}^{-1}$  to 0.36 between  $10^4\text{s}^{-1}$  and  $10^5\text{s}^{-1}$ , and for  $\zeta_e = 1.0$  the gradients are 0.54 and 0.32 at the same intervals. Compared to the ultrasoft colloids we study in [Chapter 5](#), which have gradients with the range of 0.62-0.65 for the range up to  $10^3\text{s}^{-1}$ , and 0.52-55 above (Measured in a Couette cell). Qualitatively, at high shear rates, these numbers agree - at a higher shear rate, the shear thinning is greater as the exponent falls. The precise gradients differ, but this would be expected - any realisation of a micro-gel system will have some amount of polydispersity, and it is probably that this

## 6.5 Comparison to experiments and other simulation techniques

---

would affect structure and dynamics of rearrangement, offering more resistance or a more complicated response to layering as the particles are of different size. Additionally, the gradients differ depending on  $\zeta_e$ , so further exploration of  $\zeta_e$  or  $K$  might allow more closely matched shear thinning behaviour to be recovered.

At lower shear rates, their behaviour differs more significantly. The ultrasoft colloidal systems in [Chapter 5](#) were not yield-stress fluids, whereas to the best of our knowledge we observe a yield stress, shear thinning fluid in our simulations. This indicates that merely having colloids that are thermal and can respond anisotropically to contact is not by itself enough to reproduce the behaviour of ultrasoft colloids in simulation. While more complex than many contemporary approaches, reproducing more behaviour, our model is still making many simplifying assumptions compared to real systems. Additionally, similar flowcurves have been produced in simulation techniques that do not require such a computationally expensive approach ([Khabaz \*et al.\*, 2017, 2020](#)). Simply having Hertzian behaviour in a system is not enough to produce this behaviour either - [Zakhari \*et al.\* \(2018\)](#) consider packed ( $\phi = 0.739 - 0.916$ ) colloidal systems with a Hertzian potential under Brownian dynamics, and find discontinuous diffusivity and shear responses while increasing the Peclet number, and they do observe ordering into string like dynamics.

However, we must again remark that we cannot have high confidence in our low shear rate results, especially as we simulate a microrheological system and therefore may see results that would be within experimental error in a practical bulk system. For example, our systems for the lowest shear rates are almost unstrained, and yet we have a definitively positive stress response, but in a practical system we would expect this response to be lost in noise. Additionally, if we were

## 6. SHEARED SIMULATION RESULTS

---

to cherry pick within our range of error, we could also have behaviour that does not match yield stress. As discussed above, due to time and computational constraints, we cannot be confident either that we have fully characterised sampling error or reached the steady state stress response.

While simulations of colloids based on Hertzian potentials can undergo shear-induced diffusion (Bonnecaze *et al.*, 2020), they do not tend to be thermal systems at high volume fraction, as the underlying assumptions of these models prevent sensible simulation of particles that are too soft. For regimes such as the ones we choose, thermally driven large deformations of particles are possible. As well as this, if particles under shear are distorted, this may aid in diffusion. Observing the effect of shear on the diffusion of the colloids, at the timescale of rearrangement, is a result that would be difficult to sensibly achieve in other simulation techniques. In general, while any of the quantities measured here could be measured through more simplistic simulation techniques, any effect of multi-contact deformation or shape change through homogenous shear and thermal deformation could affect those results. This makes simpler techniques unlikely to be able to recover the behaviour we see in these results other than the steady-state flowcurve.

### 6.6 Conclusion

In this chapter we have applied a linear shear to simulations with the lowest moduli. We have measured the corresponding stress response and found it to be consistent with a shear thinning yield stress fluid. We have found that applying shear to the simulations seems to yield significant dynamical differences only where the shear rate operates on timescales faster than the timescale of cage

escapes measured in [Chapter 4](#). This can be interpreted as the point at which the shear overwhelms the systems ability to dissipate stress. At this point, scattering indicates we move into another, layered structure, and our MSD results indicate that this first significantly lowers the energy barrier for cage breaking, and at the highest shear rate is not consistent with cage-breaking or diffusive behaviour at medium to long timescales. Normal stress difference measurements are consistent with measurements from the literature of systems with deformable interfaces, but we observe no qualitative difference from measures with simpler interactions that approximate deformability. This change in regime also sees a reduction in the observed volume fraction, which further supports the existence of a layered structure. Finally, we have found that simply simulating monodisperse compressible and deformable particles is not sufficient to generate qualitatively different shear responses compared to less computationally expensive methods.

## 6. SHEARED SIMULATION RESULTS

---

# Chapter 7

## Conclusion

In this chapter, we briefly reiterate the progress made in this thesis, and then discuss future development and research directions based on this progress.

### 7.1 Progress overview

The approach of using FFEA to simulate packed soft colloidal systems has allowed us to address multiparticle contacts and the resulting anisotropic deformation in three dimensions, using physically meaningful parameter choices, which has not been done before. We have modified the code to include Periodic Boundary conditions to approximate a bulk solution by simulating up to 1000 colloids in a simulation box. We have further modified this implementation to support Lees-Edwards boundary conditions, which approximate a bulk solution undergoing linear shear. We have also implemented a runtime multi- $\tau$  correlator, which allows collection of data from a range of timescales in both a memory and computationally efficient manner.

## 7. CONCLUSION

---

In [Chapter 4](#) we used FFEA to simulate quiescent systems. We have shown that rearrangements occur for all the effective volume fractions and material parameters we have simulated, with evidence of a cage-breaking regime at long times. A key advantage of our approach is that we can vary the effective volume fraction and observe the resulting volume fraction, along with varying material parameters in a physically meaningful way. We have found that, even at very high volume fractions that would have crystalline order for hard sphere systems, the thermal activity of our colloids is sufficient that we see no long-range ordering in our systems, though possibly with some short range ordering. In addition we observed a rise and fall in non-Gaussian behaviour of displacement coinciding with the approach to the cage-breaking regime, corroborating its existence. We made a preliminary investigation of correlations between particle shape and motion, but found there was insufficient data to draw conclusions.

We also investigated the stress autocorrelation function of quiescent systems, finding a superposition of intra-particle and structural deviatoric stresses. A key unexpected finding is that we observed that the structural stress scales with  $\phi$ , unlike the MSD, which does not. This result would not be possible for types of simulation which cannot represent deformation directly.

In [Chapter 5](#) we discussed our experimental investigation of ultrasoft microgels, building on the work of [Mattiello \(2018\)](#) by verifying negligible free chain content from synthesis. We confirm the observations that this class of ultrasoft microgels have qualitatively distinct behaviour to most other microgels, as they do not have distinguishable entropic and jammed glass regimes. We observe a lack of aging or history dependence, consistent with the proposed explanation that this microgels self-squeeze and thereby rearrange. We also confirm that these systems

## 7.2 Future applications and development

---

can be mapped onto a master curve solely through scaling their shear stress, and do not require scaling of strain rate as more densely crosslinked systems do, suggesting that the the associated timescales are independent of volume fraction for these systems.

Finally, in [Chapter 6](#) we applied linear shear to simulations of an ensemble of low modulus colloids, to determine the corresponding shear modulus for the system. We have found that applying shear produces substantial dynamical and structural differences only when the shear rate exceeds the inverse timescale of cage escapes found in the corresponding quiescent simulations. We found that this initially lowers the energy barrier for cage breaking, and then moves to non-diffusive behaviour at the highest shear rate. We find evidence of a switch to a layered structure at these high shear rates. However, we find that overall we generate qualitatively similar shear responses to those seen with computationally less expensive methods. Layering, the shape of the flowcurve and normal stress differences have been reproduced before by simpler methods, and it is reasonable to conclude that self-squeezing is not the only unusual attribute of ultrasoft microgels, at least with our simulation method.

## 7.2 Future applications and development

As many of the results presented in this work are qualitative or preliminary, we might make them more robust largely through running more simulations with different parameters. We also might approach measures such as correlation of asphericity and movement with a run-time correlator, making this measure more robust. We would also conduct a more detailed exploration of the parameter

## 7. CONCLUSION

---

space studied, and expand it with higher moduli and volume fractions, as this would allow us to quantitatively understand the scaling of structural modulus with volume fractions. This might also allow us to more strongly relate the structure of the system with the modulus. It would also be useful to run some simulations for longer timescales, to ensure greater convergence, and to confirm the system is ergodic as we assume, as well as more strongly confirming the existence of the second diffusive regime. Varying the size of the simulations, and constructing measures for the spatial correlation of particle motion would also allow us to calculate the lengthscales of diffusion in these systems.

The immediately obvious next step for using FFEA to model packed soft colloidal systems is to find an effective way to approach polydispersity. Most soft matter systems will have some amount of polydispersity, and so to truly approximate these systems this must be added. We attempted to add polydispersity to our simulations, but time constraints meant that we were not able to implement solutions to the issues we encountered. In this case, we simply scaled the same input files by different amounts to approximate a normal or triangle distribution in particle size. To introduce a polydispersity of even 0.05, however, can require a  $3\times$  range in volume. In turn, for scaled element size, this would require altered timesteps for the smaller elements and therefore the greater chance of inversion, and interactions cutoffs would need to be scaled with the largest elements. An alternate approach would be to keep element size roughly the same, but scale mesh complexity with size. However, this is only easily achievable with systems with discrete levels of dispersity, such as bidisperse and tridisperse systems. It is not clear that these systems would appropriately model true polydisperse systems.

Another development would be to mix particles of various moduli, or incor-

## 7.2 Future applications and development

---

porate particles that are not deformable. This would be helpful as it would allow an assessment of formulation stability, as most real industrial formulations would be multi-component systems, unlike the monodisperse, identical systems we simulate here. However, there is a challenge to mixing systems with populations of differing moduli, as the timestep will need to be decreased for higher moduli to ensure simulation stability. The neater approach would be to make some particles entirely rigid. This will not affect the necessary timestep as there is no possibility of element inversion, and the steric interactions do not need to be altered. This does mean that the code would need to be altered to add the ability to incorporate these particles. This would be of particular interest for systems of soft particles with tracer particles mixed in, such as drilling muds, as it is not clear that the movement of these tracer particles accurately represents the movement of the emulsion in general.

Another direction for development is coupling the particle meshes to a hydrodynamic mesh using a boundary element method. The already high computational expense of simulating sufficiently large systems of packed colloids currently precludes pursuing this line of research for highly packed systems, and we have already made the argument that contact forces should be more important for highly packed systems. However, it would be far more important for intermediate values of packing, below a volume fraction of 0.5, as contact becomes less relevant. It may also be useful for the interactions between objects with a significant size differential.

Another key way to improve FFEA for specifically the simulation of soft colloidal systems is code optimisation; specifically, the handling of interactions, and the approach to parallelisation. The handling of interaction currently in-

## 7. CONCLUSION

---

volves second order elements which are not necessary for stability with steric or Lennard-Jones interactions. These subdivide each surface face of a colloid into 4, meaning that checking for interactions is approximately sixteen times as costly as necessary. However, to remove this structure from FFEA would take significant development work. For parallelisation, an efficient MPI implementation is required, and this would allow more populous systems or systems with more complex internal structure to be simulated.

For future experimental investigations, it would be interesting to see high resolution confocal microscopy of ultrasoft particles such as those discussed in [Chapter 5](#). As [Mattiello \(2018\)](#) posited a key behaviour of these particles might be that they are soft enough to self-squeeze, much like our thermally diffusing systems, it would be interesting to see this experimentally confirmed. The results could then be compared to our simulations. It would also be interesting to see micro-rheology with particle tracking performed on these systems, to compare to our simulated, sheared systems, and to see if the behaviour is similar. It appears from our results that we are missing a quality of these systems and how they respond to shear, and direct observation might begin to elucidate what this is.

# References

- ACCIARO, R., GILNYI, T. & VARGA, I. (2011). Preparation of monodisperse poly(*n*-isopropylacrylamide) microgel particles with homogenous cross-link density distribution. *Langmuir*, **27**, 7917–7925, pMID: 21591700. [131](#)
- ADAM, G. & GIBBS, J.H. (1965). On the temperature dependence of cooperative relaxation properties in glassforming liquids. *The Journal of Chemical Physics*, **43**, 139–146. [16](#)
- AUFDERHORST-ROBERTS, A., BAKER, D., FOSTER, R.J., CAYRE, O., MATTSSON, J. & CONNELL, S.D. (2018). Nanoscale mechanics of microgel particles. *Nanoscale*, **10**, 16050–16061. [44](#), [74](#), [75](#), [161](#)
- BACHMAN, H., BROWN, A.C., CLARKE, K.C., DHADA, K.S., DOUGLAS, A., HANSEN, C.E., HERMAN, E., HYATT, J.S., KODLEKERE, P., MENG, Z., SAXENA, S., SPEARS JR, M.W., WELSCH, N. & LYON, L.A. (2015). Ultrasoft, highly deformable microgels. *Soft Matter*, **11**, 2018–2028. [75](#)
- BASU, A., XU, Y., STILL, T., ARRATIA, P.E., ZHANG, Z., NORDSTROM, K.N., RIESER, J.M., GOLLUB, J.P., DURIAN, D.J. & YODH, A.G. (2014). Rheology of soft colloids across the onset of rigidity: scaling behavior, thermal, and non-thermal responses. *Soft Matter*, **10**, 3027–3035. [152](#)

## REFERENCES

---

- BÉCU, L., MANNEVILLE, S. & COLIN, A. (2006). Yielding and flow in adhesive and nonadhesive concentrated emulsions. *Phys. Rev. Lett.*, **96**, 138302. [152](#)
- BERTHIER, L., MORENO, A.J. & SZAMEL, G. (2010). Increasing the density melts ultrasoft colloidal glasses. *Phys. Rev. E*, **82**, 060501. [17](#), [18](#)
- BONNECAZE, R.T., KHABAZ, F., MOHAN, L. & CLOITRE, M. (2020). Excess entropy scaling for soft particle glasses. *Journal of Rheology*, **64**, 423–431. [123](#), [180](#)
- BOUDARA, V.A.H., READ, D.J. & RAMREZ, J. (2020). reptate rheology software: Toolkit for the analysis of theories and experiments. *Journal of Rheology*, **64**, 709–722. [xix](#), [115](#), [116](#), [117](#)
- CLOITRE, M., BORREGA, R., MONTI, F. & LEIBLER, L. (2003). Glassy dynamics and flow properties of soft colloidal pastes. *Phys. Rev. Lett.*, **90**, 068303. [152](#)
- CROCKER, J.C. & GRIER, D.G. (1996). Methods of digital video microscopy for colloidal studies. *Journal of Colloid and Interface Science*, **179**, 298 – 310. [11](#)
- CUETOS, A., MORILLO, N. & PATTI, A. (2018). Fickian yet non-gaussian diffusion is not ubiquitous in soft matter. *Phys. Rev. E*, **98**, 042129. [106](#)
- DAS, P., VINUTHA, H.A. & SASTRY, S. (2020). Unified phase diagram of reversible–irreversible, jamming, and yielding transitions in cyclically sheared soft-sphere packings. *Proceedings of the National Academy of Sciences*, **117**, 10203–10209. [19](#)

## REFERENCES

---

- DE MICHELE, C., DEL GADO, E. & LEPORINI, D. (2011). Scaling between structural relaxation and particle caging in a model colloidal gel. *Soft Matter*, **7**, 4025–4031. [8](#), [17](#)
- DI COLA, E., MOUSSAD, A., SZTUCKI, M., NARAYANAN, T. & ZACCARELLI, E. (2009). Correlation between structure and rheology of a model colloidal glass. *The Journal of Chemical Physics*, **131**, 144903. [2](#)
- EDIGER, M.D. (2000). Spatially heterogeneous dynamics in supercooled liquids. *Annual Review of Physical Chemistry*, **51**, 99–128, PMID: 11031277. [16](#)
- EINSTEIN, A. (1905). ber die von der molekularkinetischen theorie der wrme geforderte bewegung von in ruhenden flssigkeiten suspendierten teilchen. *Annalen der Physik*, **322**, 549–560. [3](#)
- EISENMANN, C., KIM, C., MATTSSON, J. & WEITZ, D.A. (2010). Shear melting of a colloidal glass. *Phys. Rev. Lett.*, **104**, 035502. [106](#)
- ERWIN, B.M., CLOITRE, M., GAUTHIER, M. & VLASSOPOULOS, D. (2010). Dynamics and rheology of colloidal star polymers. *Soft Matter*, **6**, 2825–2833. [128](#), [130](#)
- FEDOSOV, D.A., SINGH, S.P., CHATTERJI, A., WINKLER, R.G. & GOMPPER, G. (2012). Semidilute solutions of ultra-soft colloids under shear flow. *Soft Matter*, **8**, 4109–4120. [21](#)
- FEI, L., SCAGLIARINI, A., MONTESSORI, A., LAURICELLA, M., SUCCI, S. & LUO, K.H. (2018). Mesoscopic model for soft flowing systems with tunable viscosity ratio. *Phys. Rev. Fluids*, **3**, 104304. [20](#)

## REFERENCES

---

- FERNANDEZ-NIEVES, A., WYSS, H., MATTSSON, J. & WEITZ, D. (2011). *Microgel suspensions : fundamentals and applications*. Wiley-VCH Verlag, Germany. [131](#)
- FOSS, D.R. & BRADY, J.F. (2000). Brownian dynamics simulation of hard-sphere colloidal dispersions. *Journal of Rheology*, **44**, 629–651. [88](#), [176](#)
- FRANKLIN, S.V. & WEEKS, E.R. (2014). Dynamic facilitation observed near the colloidal glass transition. [104](#)
- GEBREMICHAEL, Y., SCHRØDER, T.B., STARR, F.W. & GLOTZER, S.C. (2001). Spatially correlated dynamics in a simulated glass-forming polymer melt: Analysis of clustering phenomena. *Phys. Rev. E*, **64**, 051503. [99](#)
- GNAN, N. & ZACCARELLI, E. (2019). The microscopic role of deformation in the dynamics of soft colloids. *Nature Physics*, **15**, 683–688. [18](#), [22](#), [98](#), [104](#), [114](#), [130](#)
- GUAN, J., WANG, B. & GRANICK, S. (2014). Even hard-sphere colloidal suspensions display fickian yet non-gaussian diffusion. *ACS Nano*, **8**, 3331–3336, PMID: 24646449. [107](#)
- HABDAS, P. & WEEKS, E.R. (2002). Video microscopy of colloidal suspensions and colloidal crystals. *Current Opinion in Colloid & Interface Science*, **7**, 196 – 203. [11](#)
- HANSON, B. (2018). Mesoscale Modelling of Cytoplasmic Dynein using Fluctuating Finite Element Analysis. [29](#), [32](#), [45](#)

## REFERENCES

---

- HERSCHEL, W.H. & BULKLEY, R. (1926). Konsistenzmessungen von gummi-benzollösungen. *Kolloid-Zeitschrift*, **39**, 291–300. [170](#)
- HIRSCHFELDER, J.O. (1939). The structure of liquids. *Journal of Chemical Education*, **16**, 540–544. [5](#)
- HÖHLER, R. & WEAIRE, D. (2019). Can liquid foams and emulsions be modeled as packings of soft elastic particles? *Advances in Colloid and Interface Science*, **263**, 19 – 37. [8](#), [17](#)
- HOLLER, S., MORENO, A.J., ZAMPONI, M., BAOV, P., WILLNER, L., IATROU, H., FALUS, P. & RICHTER, D. (2018). The role of the functionality in the branch point motion in symmetric star polymers: A combined study by simulations and neutron spin echo spectroscopy. *Macromolecules*, **51**, 242–253. [99](#), [103](#)
- HOLMES, M.J., PARKER, N.G. & POVEY, M.J.W. (2011). Temperature dependence of bulk viscosity in water using acoustic spectroscopy. *Journal of Physics: Conference Series*, **269**, 012011. [44](#)
- HOOVER, W.G. & REE, F.H. (1967). Use of computer experiments to locate the melting transition and calculate the entropy in the solid phase. *The Journal of Chemical Physics*, **47**, 4873–4878. [5](#), [73](#)
- HUNTER, G. & WEEKS, E. (2012). The physics of the colloidal glass transition. *Rep. Prog. Phys.*, **75**, 66501. [xiii](#), [6](#), [16](#), [74](#), [75](#), [99](#), [149](#)
- JONES, R.B. & PUSEY, P.N. (1991). Dynamics of suspended colloidal spheres. *Annual Review of Physical Chemistry*, **42**, 137–169. [12](#), [13](#)

## REFERENCES

---

- KHABAZ, F., LIU, T., CLOITRE, M. & BONNECAZE, R.T. (2017). Shear-induced ordering and crystallization of jammed suspensions of soft particle glasses. *Phys. Rev. Fluids*, **2**, 093301. [27](#), [159](#), [162](#), [179](#)
- KHABAZ, F., CLOITRE, M. & BONNECAZE, R.T. (2018). Structural state diagram of concentrated suspensions of jammed soft particles in oscillatory shear flow. *Phys. Rev. Fluids*, **3**, 033301. [27](#)
- KHABAZ, F., CLOITRE, M. & BONNECAZE, R.T. (2020). Particle dynamics predicts shear rheology of soft particle glasses. *Journal of Rheology*, **64**, 459–468. [173](#), [179](#)
- LARSON, R.G. (1997). The elastic stress in film fluids. *Journal of Rheology*, **41**, 365–372. [173](#)
- LAEVI, N. & GLOTZER, S.C. (2004). Dynamical heterogeneity and jamming in glass-forming liquids. *The Journal of Physical Chemistry B*, **108**, 19623–19633. [104](#)
- LIKOS, C.N., LÖWEN, H., WATZLAWEK, M., ABBAS, B., JUCKNISCHKE, O., ALLGAIER, J. & RICHTER, D. (1998). Star polymers viewed as ultrasoft colloidal particles. *Phys. Rev. Lett.*, **80**, 4450–4453. [127](#)
- LIU, T., KHABAZ, F., BONNECAZE, R.T. & CLOITRE, M. (2018). On the universality of the flow properties of soft-particle glasses. *Soft Matter*, **14**, 7064–7074. [18](#), [152](#)

## REFERENCES

---

- LO VERSO, F., POMPOSO, J.A., COLMENERO, J. & MORENO, A.J. (2016). Tunable slow dynamics in a new class of soft colloids. *Soft Matter*, **12**, 9039–9046. [18](#), [22](#), [99](#), [130](#)
- LOCATELLI, E., CAPONE, B. & LIKOS, C.N. (2016). Multiblob coarse-graining for mixtures of long polymers and soft colloids. *The Journal of Chemical Physics*, **145**, 174901. [21](#)
- MAGATTI, D. & FERRI, F. (2001). Fast multi-tau real-time software correlator for dynamic light scattering. *Appl. Opt.*, **40**, 4011–4021. [57](#)
- MALEVANETS, A. & KAPRAL, R. (1999). Mesoscopic model for solvent dynamics. *The Journal of Chemical Physics*, **110**, 8605–8613. [20](#)
- MASON, T.G. & WEITZ, D.A. (1995). Linear viscoelasticity of colloidal hard sphere suspensions near the glass transition. *Phys. Rev. Lett.*, **75**, 2770–2773. [15](#)
- MATTIELLO, M. (2018). *Structure and dynamics of dense suspensions of soft colloids with tunable short-range attraction*. Université Paris Sciences et Lettres (ESPCI Paris). [xx](#), [xxi](#), [127](#), [129](#), [130](#), [132](#), [133](#), [134](#), [142](#), [143](#), [144](#), [145](#), [146](#), [147](#), [149](#), [152](#), [157](#), [184](#), [188](#)
- MATTSSON, J., WYSS, H.M., FERNANDEZ-NIEVES, A., MIYAZAKI, K., HU, Z., REICHMAN, D.R. & WEITZ, D.A. (2009). Soft colloids make strong glasses. *Nature*, **462**, 83–6. [4](#), [6](#), [7](#), [8](#), [17](#), [74](#)
- MOHAN, L., PELLET, C., CLOITRE, M. & BONNECAZE, R. (2013). Local mobility and microstructure in periodically sheared soft particle glasses and

## REFERENCES

---

- their connection to macroscopic rheology. *Journal of Rheology*, **57**, 1023–1046. [128](#)
- MOHAN, L., CLOITRE, M. & BONNECAZE, R.T. (2014). Active microrheology of soft particle glasses. *Journal of Rheology*, **58**, 1465–1482. [18](#)
- NAGAMANASA, K.H., GOKHALE, S., GANAPATHY, R. & SOOD, A.K. (2011). Confined glassy dynamics at grain boundaries in colloidal crystals. *Proceedings of the National Academy of Sciences*, **108**, 11323–11326. [106](#)
- NORDSTROM, K.N., VERNEUIL, E., ARRATIA, P.E., BASU, A., ZHANG, Z., YODH, A.G., GOLLUB, J.P. & DURIAN, D.J. (2010). Microfluidic rheology of soft colloids above and below jamming. *Phys. Rev. Lett.*, **105**, 175701. [152](#)
- OLIVER, R.C., READ, D.J., HARLEN, O.G. & HARRIS, S.A. (2013). A stochastic finite element model for the dynamics of globular macromolecules. *Journal of Computational Physics*, **239**, 147 – 165. [24](#), [28](#), [30](#), [31](#), [34](#)
- ÖTTINGER, H.C. (1996). *Stochastic Processes, Polymer Dynamics, and Fluid Mechanics*, 1–15. Springer Berlin Heidelberg, Berlin, Heidelberg. [34](#)
- PAREDES, J., MICHELS, M.A.J. & BONN, D. (2013). Rheology across the zero-temperature jamming transition. *Phys. Rev. Lett.*, **111**, 015701. [152](#)
- PELLET, C. & CLOITRE, M. (2016). The glass and jamming transitions of soft polyelectrolyte microgel suspensions. *Soft Matter*, **12**, 3710–3720. [128](#), [152](#)
- PERCUS, J.K. & YEVICK, G.J. (1958). Analysis of classical statistical mechanics by means of collective coordinates. *Phys. Rev.*, **110**, 1–13. [xvi](#), [xvii](#), [85](#), [86](#), [87](#), [89](#)

## REFERENCES

---

- PERRY, R.B. (1987). Principles of colloid and surface chemistry, second edition (hiemenz, p. c.). *Journal of Chemical Education*, **64**, A328. [9](#)
- PETEKIDIS, G., VLASSOPOULOS, D. & PUSEY, P.N. (2004). Yielding and flow of sheared colloidal glasses. *Journal of Physics Condensed Matter*, **16**, S3955–S3963. [121](#), [128](#)
- PHAM, K.N., PETEKIDIS, G., VLASSOPOULOS, D., EGELHAAF, S.U., PUSEY, P.N. & POON, W.C.K. (2006). Yielding of colloidal glasses. *Europhysics Letters (EPL)*, **75**, 624–630. [15](#)
- PINE, D.J., WEITZ, D.A., ZHU, J.X. & HERBOLZHEIMER, E. (1990). Diffusing-wave spectroscopy: dynamic light scattering in the multiple scattering limit. *J. Phys. France*, **51**, 2101–2127. [13](#)
- PRASAD, V., SEMWOGERERE, D. & WEEKS, E.R. (2007). Confocal microscopy of colloids. *Journal of Physics: Condensed Matter*, **19**, 113102. [10](#)
- PUSEY, P.N., ZACCARELLI, E., VALERIANI, C., SANZ, E., POON, W.C.K. & CATES, M.E. (2009). Hard spheres: crystallization and glass formation. *Philosophical Transactions of the Royal Society A: Mathematical, Physical and Engineering Sciences*, **367**, 4993–5011. [6](#)
- RAHMANI, Y., VAN DER VAART, K., VAN DAM, B., HU, Z., CHIKKADI, V. & SCHALL, P. (2012). Dynamic heterogeneity in hard and soft sphere colloidal glasses. *Soft Matter*, **8**, 4264–4270. [4](#), [8](#), [104](#)
- RAMÍREZ, J., SUKUMARAN, S.K., VORSELAARS, B. & LIKHTMAN, A.E. (2010). Efficient on the fly calculation of time correlation functions in com-

## REFERENCES

---

- puter simulations. *The Journal of Chemical Physics*, **133**, 154103. [xv](#), [57](#), [58](#), [59](#), [60](#), [62](#), [63](#)
- REDDY, J.N. (2006). *Introduction to the Finite Element Method, Third Edition*. McGraw-Hill Education, New York. [30](#), [31](#)
- RICHARDSON, R.A. (2014). A Mesoscale Model for Coarse-grained Protein Dynamics. [28](#)
- RICHERT, R. (2002). Heterogeneous dynamics in liquids: fluctuations in space and time. *Journal of Physics: Condensed Matter*, **14**, R703–R738. [16](#)
- RIVAS, N., FRIJTERS, S., PAGONABARRAGA, I. & HARTING, J. (2018). Mesoscopic electrohydrodynamic simulations of binary colloidal suspensions. *The Journal of Chemical Physics*, **148**, 144101. [20](#)
- ROMEO, G. & CIAMARRA, M.P. (2013). Elasticity of compressed microgel suspensions. *Soft Matter*, **9**, 5401–5406. [131](#)
- ROMEO, G., IMPERIALI, L., KIM, J.W., FERNÁNDEZ-NIEVES, A. & WEITZ, D.A. (2012). Origin of de-swelling and dynamics of dense ionic microgel suspensions. *Journal of Chemical Physics*, **136**, 1–9. [8](#)
- ROYALL, C.P., POON, W.C.K. & WEEKS, E.R. (2013). In search of colloidal hard spheres. *Soft Matter*, **9**, 17–27. [7](#)
- SCHEFFOLD, F., DÍAZ-LEYVA, P., REUFER, M., BEN BRAHAM, N., LYNCH, I. & HARDEN, J.L. (2010). Brushlike interactions between thermoresponsive microgel particles. *Phys. Rev. Lett.*, **104**, 128304. [131](#)

## REFERENCES

---

- SCHÖBERL, J. (1997). Netgen an advancing front 2d/3d-mesh generator based on abstract rules. *Computing and Visualization in Science*, **1**, 41–52. [44](#)
- SCHTZEL, K., DREWEL, M. & STIMAC, S. (1988). Photon correlation measurements at large lag times: Improving statistical accuracy. *Journal of Modern Optics*, **35**, 711–718. [57](#)
- SETH, J.R., MOHAN, L., LOCATELLI-CHAMPAGNE, C., CLOITRE, M. & BONNECAZE, R.T. (2011). A micromechanical model to predict the flow of soft particle glasses. *Nature Materials*, **10**, 838–843. [17](#), [79](#), [128](#), [152](#)
- SHENOY, S.L., PAINTER, P.C. & COLEMAN, M.M. (1999). The swelling and collapse of hydrogen bonded polymer gels. *Polymer*, **40**, 4853–4863. [9](#)
- SIERRA-MARTIN, B., LIETOR-SANTOS, J.J., FERNANDEZ-BARBERO, A., NGUYEN, T.T. & FERNANDEZ-NIEVES, A. (2011). *Swelling Thermodynamics of Microgel Particles*, 71–116. Wiley-VCH Verlag GmbH and Co. KGaA. [8](#), [75](#)
- SILLESU, H. (1999). Heterogeneity at the glass transition: a review. *Journal of Non-Crystalline Solids*, **243**, 81 – 108. [16](#)
- SINGH, S.P., WINKLER, R.G. & GOMPPER, G. (2011). Nonequilibrium forces between dragged ultrasoft colloids. *Phys. Rev. Lett.*, **107**, 158301. [127](#)
- SINGH, S.P., CHATTERJI, A., GOMPPER, G. & WINKLER, R.G. (2013). Dynamical and rheological properties of ultrasoft colloids under shear flow. *Macromolecules*, **46**, 8026–8036. [127](#)

## REFERENCES

---

- SOLERNOU, A., HANSON, B.S., RICHARDSON, R.A., WELCH, R., READ, D.J., HARLEN, O.G. & HARRIS, S.A. (2018). Fluctuating finite element analysis (ffea): A continuum mechanics software tool for mesoscale simulation of biomolecules. *PLOS Computational Biology*, **14**, 1–29. [xiv](#), [36](#), [37](#)
- STIEGER, M., RICHTERING, W., PEDERSEN, J.S. & LINDNER, P. (2004). Small-angle neutron scattering study of structural changes in temperature sensitive microgel colloids. *The Journal of Chemical Physics*, **120**, 6197–6206. [9](#), [131](#)
- STILL, T., CHEN, K., ALSAYED, A.M., APTOWICZ, K.B. & YODH, A. (2013). Synthesis of micrometer-size poly(n-isopropylacrylamide) microgel particles with homogeneous crosslinker density and diameter control. *Journal of Colloid and Interface Science*, **405**, 96 – 102. [131](#)
- STOPPER, D., ROTH, R. & HANSEN-GOOS, H. (2016). Structural relaxation and diffusion in a model colloid-polymer mixture: dynamical density functional theory and simulation. *Journal of Physics: Condensed Matter*, **28**, 455101. [21](#)
- TASSIERI, M., RAMREZ, J., KARAYIANNIS, N.C., SUKUMARAN, S.K. & MASUBUCHI, Y. (2018). i-rheo gt: Transforming from time to frequency domain without artifacts. *Macromolecules*, **51**, 5055–5068. [xix](#), [115](#), [116](#), [117](#)
- TAYLOR, G.I. (1954). Conditions under which dispersion of a solute in a stream of solvent can be used to measure molecular diffusion. *Proceedings of the Royal Society of London. Series A. Mathematical and Physical Sciences*, **225**, 473–477. [64](#), [164](#)

## REFERENCES

---

- THEERS, M., WESTPHAL, E., GOMPPER, G. & WINKLER, R.G. (2016). From local to hydrodynamic friction in brownian motion: A multiparticle collision dynamics simulation study. *Phys. Rev. E*, **93**, 032604. [20](#)
- TRAN, C.T., CRESPI, B., CERBELAUD, M. & VIDECOQ, A. (2018). Colloidal suspension by srdmd simulation on gpu. *Computer Physics Communications*, **232**, 35 – 45. [20](#)
- VAN DER SCHEER, P., VAN DE LAAR, T., VAN DER GUCHT, J., VLASSOPOULOS, D. & SPRAKEL, J. (2017). Fragility and strength in nanoparticle glasses. *ACS Nano*, **11**, 6755–6763, pMID: 28658568. [84](#), [123](#)
- VORSELAARS, B., LYULIN, A.V., KARATASOS, K. & MICHELS, M.A.J. (2007). Non-gaussian nature of glassy dynamics by cage to cage motion. *Phys. Rev. E*, **75**, 011504. [106](#)
- VOUDOURIS, P., FLOREA, D., VAN DER SCHOOT, P. & WYSS, H.M. (2013). Micromechanics of temperature sensitive microgels: dip in the poisson ratio near the lcst. *Soft Matter*, **9**, 7158–7166. [44](#), [74](#), [75](#), [76](#), [161](#)
- WEEKS, E.R. & WEITZ, D. (2002). Subdiffusion and the cage effect studied near the colloidal glass transition. *Chemical Physics*, **284**, 361 – 367, strange Kinetics. [99](#)
- WEEKS, E.R., CROCKER, J.C., LEVITT, A.C., SCHOFIELD, A. & WEITZ, D.A. (2000). Three-dimensional direct imaging of structural relaxation near the colloidal glass transition. *Science*, **287**, 627–631. [106](#)

## REFERENCES

---

- WEEKS, E.R., CROCKER, J.C. & WEITZ, D.A. (2007). Short- and long-range correlated motion observed in colloidal glasses and liquids. *Journal of Physics: Condensed Matter*, **19**, 205131. [106](#)
- WINKLER, R.G., FEDOSOV, D.A. & GOMPPER, G. (2014). Dynamical and rheological properties of soft colloid suspensions. *Current Opinion in Colloid & Interface Science*, **19**, 594 – 610. [17](#)
- WITTE, J., KYREY, T., LUTZKI, J., DAHL, A.M., HOUSTON, J., RADULESCU, A., PIPICH, V., STINGACIU, L., KHNHAMMER, M., WITT, M.U., VON KLITZING, R., HOLDERER, O. & WELLERT, S. (2019). A comparison of the network structure and inner dynamics of homogeneously and heterogeneously crosslinked pnipam microgels with high crosslinker content. *Soft Matter*, **15**, 1053–1064. [9](#)
- YOON, J., CARDINAUX, F., LAPOINTE, C., ZHANG, C., MASON, T.G., AHN, K.H. & SCHEFFOLD, F. (2018). Brownian dynamics of colloidal microspheres with tunable elastic properties from soft to hard. *Colloids and Surfaces A: Physicochemical and Engineering Aspects*, **546**, 360 – 365. [99](#)
- ZAKHARI, M.E.A., HETTER, M. & ANDERSON, P.D. (2018). Effect of particle-size dynamics on flow properties of dense spongy-particle systems. *Journal of Rheology*, **62**, 543–557. [130](#), [179](#)
- ZAUSCH, J. & HORBACH, J. (2009). The build-up and relaxation of stresses in a glass-forming soft-sphere mixture under shear: A computer simulation study. *EPL (Europhysics Letters)*, **88**, 60001. [19](#)

## REFERENCES

---

ZIA, R.N., LANDRUM, B.J. & RUSSEL, W.B. (2014). A micro-mechanical study of coarsening and rheology of colloidal gels: Cage building, cage hopping, and smoluchowski's ratchet. *Journal of Rheology*, **58**, 1121–1157. [124](#)